Experimental investigation on time-dependant bond behaviour of alkali-activated concrete

Master Thesis

Structural Engineering – Concrete Structures

Student

Victor M Bettencourt de Freitas

4579046

Graduation Committee

Dr. Mladena Luković	TU Delft Concrete Structures
Ir. Zhenxu Qian	TU Delft Concrete Structures
Dr. Guang Ye	TU Delft Materials and Environment

Date of defence: 12 December 2024

Faculty of Civil Engineering and Geosciences

Stevinweg 1, Delft

Foreword

This thesis represents the culmination of a long and challenging journey, one that has tested my resolve and determination. Despite these hurdles, I remained focused on the objective I established at the outset of my Civil Engineering journey: to complete my education and obtain my degree.

I would like to express my deep gratitude to my thesis committee for their guidance and support throughout this process. A special thank you goes to Ir. Zhenxu Qian, my daily supervisor, whose dedication and involvement were invaluable. Her assistance in the lab, from concrete casting to the early stages of testing, along with her thorough and insightful feedback, were crucial to the completion of this thesis. I am also sincerely grateful to Dr. Mladena Luković, my supervisor, for her constructive feedback and valuable guidance during our meetings, which helped steer this project toward its final form. Additionally, I would like to thank Dr. Guang Ye, the third member of my graduation committee, for his participation in this endeavour.

This experimental thesis would not have been possible without the expertise and help of the personnel at the TU Delft Macrolab. I am particularly grateful to Ton Blom for his assistance during the casting sessions, to Albert Bosman for his help in designing and setting up the pull-out test apparatus, and to Ake Blom for guiding me through the testing process.

Finally, I would like to extend my heartfelt thanks to my family and friends, whose constant encouragement and support helped me persevere through the challenges and complete this thesis.

Summary

Efforts are being made worldwide to reduce CO_2 emissions across various industries, with the construction sector being a significant contributor. Cement production alone accounts for about 6% of global anthropogenic CO_2 emissions. To address this, alternative materials to OPC (Ordinary Portland Cement) have gained substantial academic and industrial interest. One such alternative is alkali-activated concrete (AAC), which replaces OPC with industrial by-products such as granulated blast furnace slag (BFS) and fly ash (FA) from steel and coal industries respectively. These materials, known as precursors, are activated primarily using sodium hydroxide and sodium silicate alkaline solutions to produce AAC.

AAC has demonstrated mechanical properties comparable to or even superior to conventional concrete, along with additional benefits such as enhanced chemical, acid, and fire resistance. However, despite its potential, AAC has yet to be widely adopted for structural applications. This is mostly due to the fact that the majority of research conducted thus far has concentrated on its microstructure and material properties, resulting in a knowledge deficit about its performance in larger structural components and its long-term behaviour.

The focus of this study is on alkali-activated slag-based concrete (AAS), which has been shown to experience changes in material properties when exposed to drying. Previous studies have reported decreases in E-modulus, flexural strength, and tensile splitting strength over time in AAS under these conditions. However, how these long-term material developments impact the structural integrity of AAS remains unclear, particularly in relation to bond behaviour. Bond behaviour is critical to the performance of structural elements, as it governs the transfer of forces between reinforcement and the surrounding concrete, thereby influencing the overall structural capacity.

The main objective of this study is to determine the influence of curing conditions, curing age, and reinforcement type on the bond behaviour of slag-based alkali-activated concrete. More specifically, it aims to assess to what extent the observed decrease in material properties affect bond behaviour. This is investigated through pull-out tests, where the protruding reinforcement is pulled out of the concrete cube while recording the applied tensile force and rebar displacement to evaluate the bond strength between the concrete and the embedded reinforcement.

The experimental methodology consists of testing concrete specimens at different curing ages (28 days and 84 days) to assess the effects of curing age and conditions on bond strength. All specimens are initially cured in standard moisture conditions for 28 days, after which a portion is tested to serve as a reference against older specimens. The remaining specimens are either left to continue curing under optimal moisture conditions or exposed to drying conditions until they reach 84 days of age. Afterward, pull-out tests are conducted on both sets of specimens to determine the influence of curing condition (moisture vs. drying) and age on the development of bond strength over time. This method is applied to two types of reinforcement, steel and prestressing strand, and is conducted for both AAS and conventional concrete (CC), with CC serving as a reference for AAS.

Prior to the main research objective, a preliminary study was conducted to address the first research question: "What is the optimal method for conducting a pull-out test?" This question, although not tied to the main objective, aimed to determine the optimal specimen configuration, test procedure, and setup for an accurate assessment of the bond behaviour based on the available facilities in Macrolab TU Delft. This entails a preference for pull-out failure over splitting failure. Splitting failure represents a brittle failure mode, where the concrete suddenly cracks once its tensile strength is exceeded. In contrast, pull-out failure exhibits more ductile behaviour, allowing the rebar to gradually

yield. This gradual yielding leads to noticeable deformations, which serve as warning signs, enabling users and engineers to assess the situation and intervene before collapse. Regarding the study on the bond strength, pull-out failure is preferred because this failure mode provides a more accurate measure of the maximum concrete-rebar bond capacity. This upper bound failure mode signifies the structures maximum bond potential without premature failure. Whereas splitting failure is a lower bound premature failure and is more dependent on complex factors relating to material properties such as concrete tensile strength and internal crack propagation.

Three distinct configurations were examined for the steel reinforced specimens. The main distinction between them was the presence of an unbonded top layer in the concrete preceding the bonded region. Result suggests that specimens containing an unbonded concrete layer above the bonded region are more likely to fail on pull-out, due to the additional concrete mass providing necessary resistance against tensile stresses. The choice of specimen configuration aligns with the modified test setup, designed to measure rebar displacement at both the free and loaded ends of the specimens. Displacement measurement at the free end is preferred, as it excludes rebar deformation, offering a more accurate reading. Therefore, configuration 3 was selected to enable precise measurement of rebar slip at the free end (bottom) of the specimens.

Regarding the testing procedure, a key factor was the amount of confinement that was applied. As the rebar is pulled, a wedging action occurs when the crushed concrete in front of the rebar ribs is pushed outward, generating radial tensile stresses that can lead to undesirable splitting failure. This failure mode is characterized by a rapid loss of bond resistance, making it less safe and underscoring the necessity for confinement to prevent such occurrences. Tests were conducted with varying levels of confinement—ranging from none to excessive. It was observed that without any confinement, the pull-out setup experienced movement, which negatively affected the results. Conversely, excessive confinement often led to premature failure. This was primarily due to securing the rebar before applying confinement, which caused the rebar to effectively be pulled out prematurely as a result of compression on the top plate. Additionally, the deformation of the top plate from the applied confinement generated localised stresses that resulted in the specimen's splitting. The optimal confinement level was determined to be 60-80 Nm, inhibiting movement of the setup. Ultimately, this preliminary investigation provided valuable insights into specimen’s configurations and test procedures, setting the stage for the main experiment.

Subsequently, the main experiment was conducted to investigate the influence of curing conditions and curing age on the bond behaviour of AAS reinforced with both steel and prestressing strands. Two groups of AAS specimens were prepared: one group was subjected to standard moisture curing (22°C and 99% RH) for 28 days, followed by drying (20°C and 55% RH) for up to 84 days, while the other group remained in moist conditions for the entire duration. For comparison, conventional concrete (CC) samples, set as a reference, were also subjected to standard moisture curing for 28 days and then placed in drying conditions for up to 168 days. Pull-out tests were performed on all groups at intervals of 28, 84, and 168 days (only for CC), complemented by compressive and tensile splitting tests.

Results indicate that bond strength in conventional concrete (CC) remains unaffected under dry conditions, aligning with its stable material properties. In contrast, AAS specimens displayed a noticeable decrease in bond strength, though large variations in results suggest that the effect of drying may not be definitive. Closer inspection of DIC, DFOS, and execution revealed no clear differences, leaving the results inconclusive. Nonetheless, it is clear that drying did influence the bond behaviour of AAS. Although the material properties of AAS did not show a direct correlation with bond strength reduction, the substantial shrinkage observed in AAS due to drying likely

contributed to microcracking, which adversely affects tensile splitting strength and bond integrity . Ultimately compromising bond integrity.

Additionally, the study reveals that prestressed strands reinforced CC demonstrates superior bond strength compared to AAS. This disparity is attributed to varying proportions in the contributions of bond transfer mechanisms and concrete tensile strengths. The smoother surface of the prestressed strands relies heavily on friction for bond transfer, which is more effective in CC due to its higher tensile splitting strength. In contrast, the reduced tensile strength of AAS, influenced by factors such as drying shrinkage and microcracking, limits its bond capacity, leading to weaker bond performance.

When comparing the results between steel reinforcement and prestressing strands, the difference in failure modes is notable. In the case of steel-reinforced specimens, only two failed due to splitting, while the majority exhibited pull-out failure. This suggests that the concrete's confinement was sufficient to resist the radial tensile stresses generated during the pull-out test. In contrast, all prestressed strand-reinforced specimens experienced splitting failure, which can be attributed to the differences in rebar geometry and bond transfer mechanisms. The smoother surface and larger diameter of the prestressing strands make them more reliant on concrete tensile strength for bond transfer, leading to earlier splitting failure, especially in slag-based alkali-activated concrete (AAS) with lower tensile strength compared to conventional concrete. The difference in dominant bond strength mechanisms between the two types of reinforcement is reflected in the observed bond strength. Steel-reinforced concrete exhibited significantly higher bond strength compared to prestressed strand-reinforced concrete. This is due to the stronger mechanical interlock provided by the ribbed surface of steel rebar, which plays a larger role in load transfer, whereas the prestressed strands rely more on friction and are therefore more susceptible to splitting failure.

Internal strain measurement using Distributed Fiber Optic Sensing (DFOS) sensors was employed to provide further insights into the internal bond behaviour. In some cases, the internal strain measurements were consistent with the theoretical strain derived from the external strength gained from pull-out tests. Particularly in the top unbonded layer preceding the bonded segment. This indicates that DFOS can accurately measure the internal distribution of bond stress. However, notable inconsistencies were observed, particularly high peak strain values at the boundaries of the bonded segment, which significantly affected the strain measurements in the bond region. The inconsistencies likely arose from disruptions associated with the technique employed to install pipe covers to the rebar at the unbonded sections. While DFOS demonstrates promise in evaluating bond behaviour, these boundary effects underscore the necessity for additional refining of the setup to enhance measurement accuracy and consistency.

Estimating bond strength is vital for the safety and structural design of concrete structures. The pull-out test results were compared to various semi-empirical models and code standards. The semi-empirical models were generally conservative, even for the lower bond strengths observed in dry-exposed AASC specimens. This lower bond strength arises from the models' derivation from lap-spliced beams, where the surrounding concrete matrix is under tension, leading to typically lower bond strengths compared to pull-out tests. Comparisons with other studies show a similar trend, with pull-out test results being more conservative relative to these models, while beam-end test results align more closely with them. Code standards, particularly Eurocode 2, were also conservative, with all bond strength results compliant. However, the reduced bond strength in drying-exposed AAS specimens fell below minimum requirements according to standards like AS 01 and ACI 318. The pull-out test results aligned with the Harajli bond behaviour model for CC and moisture-cured AAS specimens, with the exception of the AAS specimens that underwent drying. The noted reduction in bond strength resulting from drying effects in AAS may result in unsafe designs.

In conclusion, this study aimed to determine the impact of drying conditions on the bond behaviour of AAS over time. The results for steel-reinforced AAS were inconclusive. However, some reductions in bond strength may be linked to drying shrinkage and subsequent microcracking. Regarding prestressed strand-reinforced concrete specimens, the results reflect the main bond transfer mechanism that prevails in this type of reinforcement. The exclusive splitting failure highlights the impact of rebar geometry, where the bond transfer mechanism relies primarily on friction. The lack of mechanical interlock means that bond strength is highly dependent on the concrete's tensile strength, explaining the exclusive splitting failure. The observed reduction in bond strength is a considerable concern for the further implementation of AAS in structural applications, particularly prestressed structures.

Moreover, the study also found that existing analytical models for conventional concrete may not be directly applicable to AAS, particularly under drying conditions. It was shown that the decreased bond strength observed in AAS specimens exposed to drying may result in unsafe designs when relying on existing analytical models for conventional concrete. This underscores the need for further research to refine or develop new models that can more accurately capture the time-dependent behaviour and specific characteristics of AAS.

Further research is required to determine the full extent of these issues and ensure the safe and effective use of AAS in future structural applications.

Symbols and Abbreviations

Abbreviations

AAC	Alkali-Activated Concrete
AAS	Alkali-Activated Slag-based Concrete
AASC	Alkali-Activated Self-Compacting Concrete
AAF	Alkali-Activated-Fly-Ash-based Concrete
AASF	Alkali-Activated Slag and Fly Ash-based Concrete
FA	Fly Ash
FRP	Fibre Reinforced Polymer
DFOS	Distributed Fiber Optic Sensing
DIC	Digital Image Correlation
GPC	Geopolymer Concrete
GGBFS/BFS	Granulated Ground Blast Furnace Slag
OPC	Ordinary Portland Cement
SCMs	Supplementary Cementitious Materials
C-(A)-S-H	Calcium-(Alumino)-Silicate-Hydrate
N-A-S-H	Sodium-Alumino-Silicate-Hydrate
ITZ	Interfacial Transition Zone

Chemical notations

Al_2O_3	Alumina
CO_2	Carbon di-oxide
CaO	Calcium oxide (lime)
$CaCO_3$	Calcium Carbonate (Limestone)
$\mathrm{Ca}(OH)_2$	Calcium hydroxide (slaked lime)
NaOH	Sodium hydroxide (caustic soda)
$NaCL$	Sodium chloride
Na_2SO_4	Sodium sulphate
Na_2CO_3	Sodium carbonate
$Na_2\mathrm{Si}O_3$	Sodium silicates
SiO_2	Silicon dioxide

Contents

Foreword 2
Summary 3
Symbols and Abbreviations 7
1. Introduction 10
1.1 Background 10
1.2 Problem statement 12
1.3 Research questions 13
1.4 Outline 14
2. Alkali Activated concrete and its material properties 15
2.1 Alkali Activated concrete 15
2.1.1 History 15
2.1.2 Constituents 16
2.1.3 Terminology 17
2.1.4 Classification 17
2.2 Material properties 20
2.2.1 Mechanical properties 21
2.2.2 Volume stability 22
2.2.3 Durability 23
3. Bond Behaviour in Concrete 24
3.1 Introduction 24
3.1.1 History 24
3.1.2 Bond stress 24
3.1.3 Bond mechanisms 26
3.1.4 Bond Failure modes and behaviour 28
3.1.5 Test type 29
3.2 Summary of State-of-the-Art report 30
3.2.1 Influence parameters for bond behaviour 32
3.2.2 Tension stiffening effect 34
3.3 Conclusion 35
4. Experimental Program 36
4.1 Overview 36
4.1.1 Variable Implementation and sub-objectives 36
4.1.2 Approach 37
4.2 Material, casting and curing procedures 40
4.2.1 Material and Mixture design 40

4.2.2 Casting and Curing procedure 41
4.3 Specimen preparation 44
4.3.1 Moulds 44
4.3.2 Monitoring device installation 47
4.3.3 Configuration 49
4.3.4 Size and Configuration Results 52
4.4 Test Method 58
4.4.1 Test Setup 58
4.4.2 Preliminary Test Procedure and Results 60
4.4.3 Optimal Testing Procedure 62
4.4.4 Monitoring Devices and Mechanical Tests 63
5. Experimental Results 64
5.1 Mechanical Properties 64
5.2 Pull-out results 67
5.2.1 Steel reinforced specimens 68
5.2.2 Steel reinforced specimens: DIC results 71
5.2.3 Steel reinforced specimens: DFOS measurements 75
5.2.4 Prestress reinforced specimens 81
5.2.5 Prestress reinforced specimens: DIC results 85
5.3 Drying shrinkage 87
6. Comparison of Analytical and Experimental results 89
6.1 Bond strength prediction models 89
6.2 Bond behaviour prediction model 92
6.3 Bond prediction Codes 94
6.4 Comparison model to test results 96
7. Conclusion 100
References 104

1. Introduction

1.1 Background

A growing trend to lower carbon dioxide (CO_2) emissions across many industries worldwide is gaining momentum. The construction industry is not an exemption. A core material in the construction industry is concrete. The ease of use and plastic consistency make concrete an extremely versatile material. In addition to being reasonably priced and easily accessible, it provides good structural performance. In part because of these favourable characteristics, concrete is the second most consumed material in the world next to water (Gagg, 2014).

Of all the components in conventional concrete the constituent contributing the most to CO_2 emissions is Ordinary Portland Cement (OPC). It was estimated the production of OPC has a significant contribution to the global anthropogenic CO_2 emissions estimated around 6% (Allwood et al., 2010). With rising population and the need for urbanisation and infrastructure development. Global cement production is expected to grow 12-23% from 2014 levels by 2050 (IEA, 2018), see Figure 1-1. This poses a challenging goal for the cement industry as it faces growing demand while aiming to reduce CO_2 emissions.

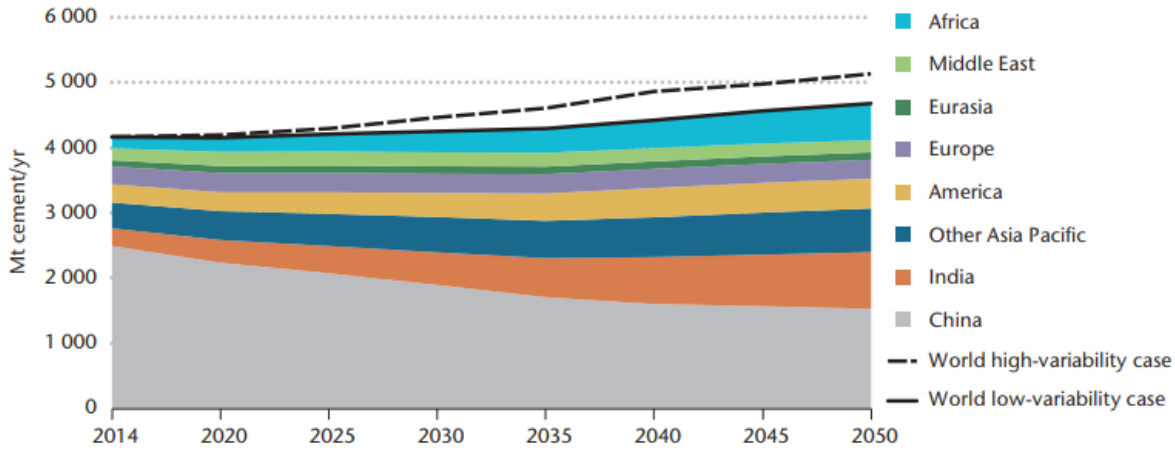

Figure 1-1: Cement consumption projections (IEA, 2018)

The bulk of CO_2 emission during cement production occurs during the clinker production in the kiln. With 60-70% of CO_2 emissions resulting from the calcination process, Eq. 1-1. Limestone ($CaCO_3$) is converted into lime (CaO) and carbon dioxide (CO_2). Whereas, the remaining 30-40% of CO_2 emissions comes from fuel combustion (IEA, 2018).

$$CaCO_3 \rightarrow CaO + CO_2 \qquad \text{Eq. 1-1}$$

Therefore, optimizing the cement production process by improving energy efficiency, reducing clinker to cement ratio, switching to alternative fuels and implementing emerging and innovative technologies such as carbon capture are all viable methods in reducing CO_2 emissions. Still, the biggest reduction in emissions follow from reducing clinker ratio (IEA, 2018; Kajaste & Hurme, 2016). To IEA indicates that a reduction in clinker to cement ratio from 0.64% in 2014 to 0.60% is necessary to reach the 2-degree scenario (2DS) by 2050 as stipulated by the IPCC. The incorporation of supplementary cementitious materials (SCMs) in cement blends is common practise in the

construction industry, serving as alternative binders to clinker. Common industrial byproducts utilised include fly ash, blast furnace slag, silica fume, rice husk ash and metakaolin, as indicated in Table 1-1.

Increasing attention has been paid to the environmental impact of the construction industry in the Netherlands. A LCA (Life Cycle Assessment) study conducted by CE Delft revealed that concrete usage contributes 40-60% of the total environmental impact, of which cement accounted for 95% of the impact (Bijleveld et al., 2013). In order to reduce this impact, the use of CEM III concrete, which contains 36% to 95% blast furnace slag (BFS), is encouraged over CEM I, which comprises at least 95% clinker. In the Netherlands, CEM III is already widely adopted, making up 50-60% of total cement usage (Bijleveld & Beeftink, 2020). The Netherlands serves as an example that significant reduction in clinker to cement ratio can be achieved in the construction industry, in line with global climate goals such as those outlined by the IEA and IPCC.

Table 1-1: Cement types EN 197-1

Type	Name	Clinker	Other components
CEM I	Portland cement	95-100%	5%
CEM II	Portland composite	65-94%	BFS, Silica, Pozzolan, FA
CEM III/A	Blast furnace slag cement	35-65%	36-65% BFS
CEM III/B		66-80%	66-80% BFS
CEM III/C		81-95%	81-95% BFS
CEM IV	Pozzolan cement	45-89%	Pozzolan, FA
CEM V	Composite cement	20-64%	BFS + Pozzolan, FA

In addition to clinker reduction strategies, Alkaline-Activated Concrete (AAC) presents a promising alternative to cement is. AAC replaces OPC entirely by using industrial waste such as fly ash (FA) or granulated ground blast furnace slag (GGBFS) as precursor combined with an alkaline activator, (see Figure 1-2). By eliminating OPC a more sustainable concrete without clinker can be produced. Leading to a 44-64% reduction in greenhouse gas emissions when using AAC (McLellan et al., 2011). However, this is reduction depends on whether or not the precursors are categorized as waste as opposed to by-products (Habert et al., 2011).

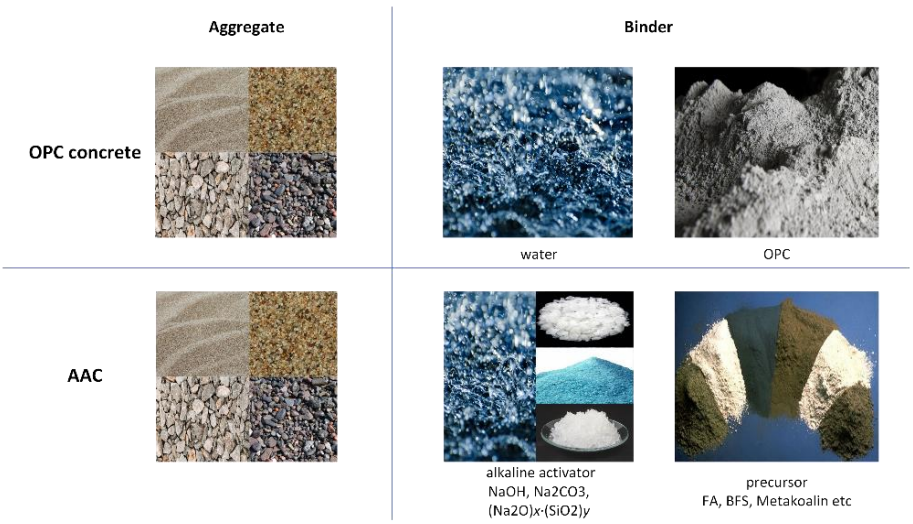

Figure 1-2: CC vs AAC composition

1.2 Problem statement

Alkali-activated concrete (AAC) is emerging as a promising alternative to CC for future construction. Investigations on AAC have been carried out for a couple of decades. AAC might provide comparable or better mechanical properties compared to CC (Nath & Sarker, 2017). Besides AAC has shown encouraging qualities. Several studies indicate that fly ash-based alkali activated concrete (AAF) exhibits superior resistance to chemical assaults, such as acids and sulphates (Fernandez-Jimenez et al., 2007; Hardjito et al., 2004; Rangan, 2009) and demonstrates enhanced fire resistance (Zhang et al., 2018). However, despite these promising results, AAC's structural behaviour, particularly at a large scale, remains insufficiently understood (Ma et al., 2018).

While extensive research has been conducted on the material microstructure and mechanical properties of AAC, the behaviour of structural elements, specifically bond behaviour, is still not comprehensively understood. Bond behaviour is crucial in the performance of structural elements. Bond enables the reinforcement and concrete matrix to transfer forces locally within the structure elements. This occurs by a number of mechanisms including adhesion, friction and bearing. Furthermore, bond enables the tension stiffening effect. Tension stiffening is referred to the ability of concrete to carry tensile stresses between the formation of cracks. This tensile contribution of the concrete stiffens the member and reduces deflections. For serviceability limit state bond influences the crack spacing and crack width. The latter is a crucial factor for durability since structural elements are less prone to corrosion if crack width is limited.

Bond behaviour has been proven to correlate well with material properties such as compressive strength and tensile strength (Sarker, 2011; Sofi et al., 2007). Research has shown that these material properties are time-dependant for AAC and can decrease over time. Slag-based AAC has shown to be sensitive to curing condition. Prinsse et al. (2020) reported reduction in flexural strength, tensile strength and significant elastic modulus decrease over time for samples exposed to dry laboratory conditions (20°C/50%RH). Furthermore, AAS showed higher and unstable shrinkage over time (Zhang et al., 2022). These results has been attributed to drying, emphasising the impact of curing condition. Nevertheless, the literature on the effect of curing conditions on the bond behaviour of AAS is limited. Therefore, the effect of curing condition, especially drying as well as the influence of the time dependent material properties on the bond of steel in AAC needs to be well understood.

The inherent differences in composition, including differing chemical reactions and matrix formation, between AAC and CC can lead to difference in bond behaviour. This raises concerns about the safety of extrapolating models and equations designed for ordinary Portland cement (OPC) concrete to AAC. Furthermore, the deterioration of AAS's material properties over time, especially under different curing conditions, poses a significant safety issue. While building codes for conventional concrete assume that most of its long-term strength is achieved by 28 days, with strength increasing over time due to continued hydration, this assumption does not hold for slag-based alkali-activated concrete (AAS), whose properties tend to degrade over time.

Understanding the bond behaviour of AAC, especially in relation to time-dependent material properties and different curing conditions, is crucial for its safe and effective use in structural applications. Slag-based AAC, in particular, has shown sensitivity to curing conditions, with its mechanical properties potentially decreasing over time. Such degradation can affect the bond behaviour of AAC, impacting its structural performance and raising concerns about long-term durability, which may hinder its widespread adoption in the construction industry.

This research aims to investigate the time-dependent bond behaviour of slag-based AAC under varying curing conditions. The study will focus on the bond performance of a specific self-compacting

slag-based alkali-activated concrete (AASC) mixture developed by (Zhang et al., 2022). By evaluating the bond behaviour over time, the research will assess the impact of curing conditions on structural integrity and explore the applicability of existing models designed for conventional concrete in the context of AAC.

1.3 Research questions

The following research question are sought to be answered:

Q: What is the influence of *curing condition*, *curing age and reinforcement* type on the <u>bond behaviour</u> of slag-based alkali activated concrete (AAS)?

Q1: What is the optimal method for conducting a pull-out test?

Q2: How does the bond behaviour for conventional and prestressing strand reinforced concrete develop over time under different curing conditions?

Q3: What is the applicability of existing analytical models for conventional concrete on AAS considering the time dependency?

1.4 Outline

The structure of this thesis is designed to guide the reader through a comprehensive exploration of bond behaviour in slag-activated concrete, leading to a deeper understanding of its potential for future structural applications.

The first chapter introduces the central topic of bond behaviour in AAS and explains why this research is significant. It highlights the motivation behind the development of AAC, particularly in relation to reducing CO2 emissions, and establishes the main research objective: to determine whether the observed decrease in material properties in AAS affects its bond behaviour.

Chapter 2 delves into the background of AAC, offering a brief history and detailed descriptions of its composition, key constituents, and the various classifications of alkali-activated materials (AAMs). It further explores into the material properties of AAS. This foundational knowledge sets the stage for understanding AAC's broader context.

In Chapter 3, the fundamental concepts of the bond between rebar and concrete are explored. The bond transfer mechanisms are explained, providing insight into how these processes influence bond behaviour. A State-of-the-art review on bond behaviour of AAC is presented, by examining the bond behaviour of AAC. It provides a thorough analysis of the factors influencing bond performance in AAC, including concrete strength, curing conditions, reinforcement types and concrete cover.

Chapter 4 outlines the experimental program, detailing the test setup and execution of the research. It provides a clear description of the methodology employed to assess the bond behaviour of AAS under various conditions.

In Chapter 5, the experimental results are presented. These include both material property results and the pull-out test results for steel and prestressed strand-reinforced concrete, offering a detailed analysis of how AAS performs comparison to conventional concrete under different curing conditions.

Chapter 6 focuses on the practical applications of the research, comparing the steel-reinforced pull-out test results with semi-empirical models and code standards. This comparison helps assess the applicability of existing standards to AAS in real-world design scenarios.

Finally, Chapter 7 presents the conclusions drawn from the research, answering the three sub-research questions and providing a final, concise conclusion to the main research objective. Recommendations for future research are provided, highlighting areas for additional exploration that could enhance the understanding of AAS in relation to its bond behaviour and its ultimate objective for structural applications.

2. Alkali Activated concrete and its material properties

2.1 Alkali Activated concrete

2.1.1 History

Earliest occurrence of alkali activated concrete dates back to 1895. J Whiting patented a cement derived from molten slag brought in contact with water. The resulting product is dried and mixed with slaked lime ($\mathrm{Ca}(OH)_2$) and alkaline materials such as caustic soda (NaOH), potash (KOH) and sodium chloride ($NaCL$). The mixture is ground to produce slag-based cement (Whiting, 1895). German chemist Hans Kuhl patented a similar blast furnace slag-based (BFS) concrete with the addition of alkali salt material as "accelerating material" such as sodium sulphate (Na_2SO_4) or sodium carbonate (Na_2CO_3). In combination with or without so called "developing material" containing earth oxides or hydroxides such as potassium (KOH), sodium hydrate ($NaOH$) or calcium hydrate ($\mathrm{Ca}(OH)_2$). The BFS together with the non-hygroscopic additions when hydrated with water would produce free caustic alkali connection with the slag material (Kuhl, 1908).

Later on in 1935, Belgian engineer Purdon intent on solving the current issues at that time with alkali activated slag-based concrete such as; slow hardening and low initial strength. Proposed an AAC mixture, the slag is activated by an alkali solution consisting of caustic soda ($NaOH$) or caustic potash (KOH). Purdon's mixture achieved faster activation and exhibited greater tensile strength over time compared to OPC concrete, for comparable levels of compressive strength (Purdon, 1935).

By mid-1950, fuelled by cement shortages in the Soviet Union. The need for alternative cement prompted development into AAC led by Ukrainian researcher Glukhovsky. Resulting in many infrastructure projects developed in the region since. Glukhovsky produced AAC derived from natural soils and industrial wastes precursors which were activated by either sodium hydroxide ($NaOH$) and sodium silicates ($Na_2\mathrm{Si}O_3$) solutions, with the latter being very common in modern applications of AAC. The use of metal salts and oxides with the intend to influence the chemical and physical properties as additives was also investigated. Glukhovsky also found that the amount of these additive can influence the setting time, compressive strength and water resistance (Ponomar et al., 2023).

Interest in AAC was reignited by French scientist Davidovits in the late 1970s. Urged to find a fire-resistant material after catastrophic fires in France. Davidovits, was inspired by the hydrothermal condition for zeolite synthesis. Zeolite a term which referrers to a wide group of minerals that are build-up of tetrahedral linked structures of alumina (AlO_4) and silica (SiO_4) also referred to as poly(sialate) structure. Zeolites can thermoset at room temperature conditions provided with high pH environment and alkaline source. These conditions are viable and practical for the production in the construction industry. Davidovits adopted metakaolin precursor with either ($NaOH$) or (KOH) as alkaline activator. The resulting poly(sialate) structure was coined "Geopolymer" (Davidovits, 1991)

Contrary to current motives, initial interest in AAC was driven by the commercial aspect due to AAC comparative low price and Portland cement shortages. Whereas, renewed interest is intended to curb CO_2 emissions and the application in specific fields such as; fire resistance and chemical attack resistance. In contrast with current application of AAC, initial application of AAC aimed to produce a ready-mix replacement of OPC, by mixing the precursor with the alkali source in solid form. Although more practical, a study conducted by Wang et al. (1994), demonstrated that adding the alkali in solution form as opposed to solid form results in greater strength and less strength fluctuation.

2.1.2 Constituents

Alkali activated concrete (AAC) is a term used to describe a broad range of concretes derived from mainly an alumina (Al_2O_3), silica (Si_2) and lime (CaO) containing source, also referred as precursor, see Table 2-1. Common precursors used to produce AAC are derived from; either industrial by products, incinerated materials or natural materials. The most common used industrial byproducts are FA and BFS. FA is derived from coal plants, whereas BFS from steel production. Incinerated materials such as metakaolin are derived from the calcination of kaolinite clay source. Most common precursors are depicted in the CaO-SiO_2-Al_2O_3 diagram, illustrating their composition; see Figure 2-1.

Table 2-1: Chemical composition common precursors

	CaO	SiO_2	Al_2O_3	Fe_2O_3	MgO	SO_3	K_2O	Na_2O
OPC (Bye et al., 2011)	63-67%	19-23%	3-7%	1.5-4.5%	0.5-2.5%	2.5-3.5%	0.1-1.2%	0.07-0.4%
BFS (Matthes et al., 2018)	35-48%	32-42%	6->19%	-	3-14%	1-4%	-	0.3-1.2%
FA Class C (Garcia-Lodeiro et al., 2015a)	38%	34.1%	14.2%	7.2%	1.5%	4.2%	1.4%	0.44%
Fa Class F (Garcia-Lodeiro et al., 2015a)	2.8-7%	43-60%	22-35%	6.3-18%	1.2-2.6%	0.2-1.9%	0.38-6%	0.15-1%

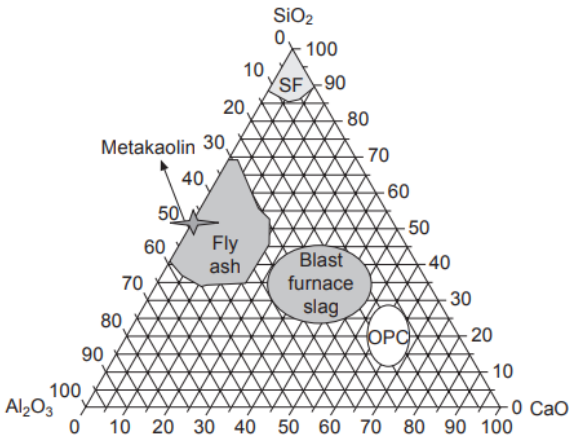

Figure 2-1: Chemical composition diagram(Garcia-Lodeiro et al., 2015a)

The precursors are activated by an alkali source and react to form the binder. Glukhovsky (1994), classified activators into six groups according to their chemical composition. An overview of the constituents of alkali-activated concrete is depicted in Figure 2-2. Sodium (Na) and potassium (K) are denoted by M.

1. Caustic solutions: MOH
2. Slightly acid, non-siliceous salts: M_2CO_3, M_2SO_3, M_3PO_4, MF
3. Silicates: $M_2O.nSiO_2$
4. Aluminates: $M_2O.nAl_2O_3$
5. Aluminosilicates: $M_2O.nAl_2O_3.SiO_2$
6. Non-siliceous, highly acid salts: M_2SO_4

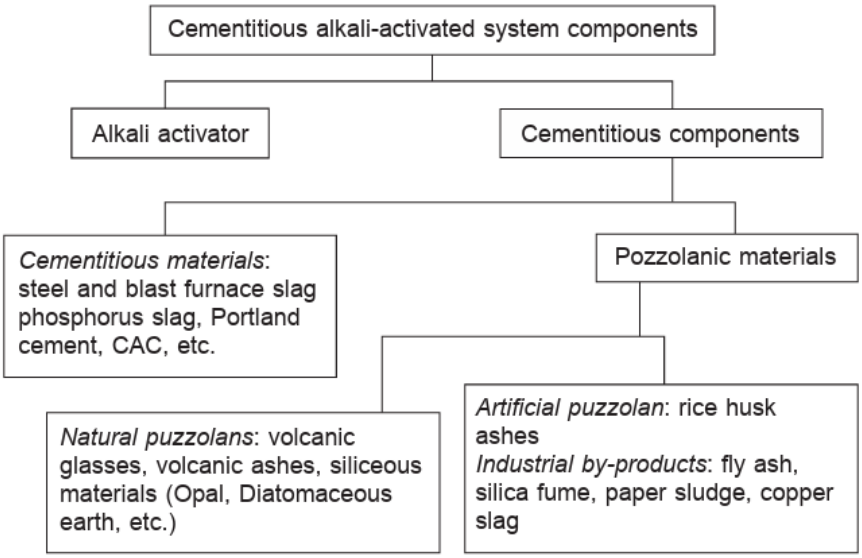

Figure 2-2: Alkali activated cements constituents (Garcia-Lodeiro et al., 2015a)

2.1.3 Terminology

A broad range of terminology is used to describe alkaline activation. These include terms such as 'soil silicate concrete' as originally referred to by Glukhovsky. To other names like 'inorganic polymers' and more popular terminology such as, Alkali Activated materials (AAM) and Geopolymer concrete as coined by Davidovits. Provis and Van Deventer (2013) categorised the whole as Alkali activated material (AAM). Encompassing any binder derived from an alkali metal source with a solid silicate precursor. Whereas, geopolymer is considered as a subset of AAMs. Only binders derived from low calcium source (fly ash) will produce a polymeric alumina and silica zeolite like chain, hence the name "geopolymer". Davidovits (2018), strongly disagrees with this notion that geopolymers are a subset of alkali-activated materials. He argues that AAM are not polymers, and can't be considered as calcium hydrate alternative. Instead, geopolymer and AAM are from a completely separate different chemistry system. AAM are hydrates, whist geopolymer are polymers. These are not the same thing.

2.1.4 Classification

A wide variety of precursors and alkali source combination are possible, each with different reaction products and microstructure development resulting in different material properties. However, the reaction products they form widely fall in two distinct camps. This classification of AAC is determined based on the calcium content of the precursor. In short, low calcium containing precursors (FA and MK) will produce N-A-S-H gels, that are zeolitic in structure. Whilst high calcium containing precursors (BFS) will produce C-A-S-H gels as reaction product, which are similar to OPC.

High Calcium Alkali Activated Concrete

High calcium precursors like BFS subjected to alkali activation, have similar hydration process to OPC concrete leading to the formation of C-S-H gel in the early stages, Figure 2-3. However, in the latter stages the reaction process differs from conventional OPC concrete, where Al is taken up in the C-S-H gel structures to form aluminium tetrahedra C-A-S-H gels (Garcia-Lodeiro et al., 2015b). Aside from the primary C-A-S-H gel, secondary hydration products are formed like calcium sulfoaluminate hydrates (AFm), hydrotalcite and zeolites. The main alkali activators used are sodium hydroxide (NaOH) and waterglass ($Na_2\mathrm{O} \cdot \mathrm{Si}O_2$) due to their relative higher pH compared to other options such as sodium carbonate (Na_2CO_3) and sodium sulphate (Na_2SO_4). The higher alkalinity results in greater dissolution of the precursor with consequent better hydration. Waterglass and (NaOH) activated slag concrete have greater early strength and slower hardening and subsequently better material properties (Bernal et al., 2014).

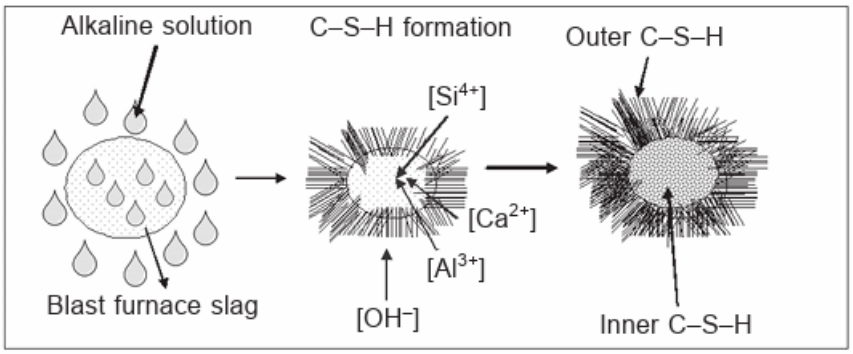

Figure 2-3: High Calcium Hydration process (Garcia-Lodeiro et al., 2015b)

Low Calcium Alkali Activated Concrete

Commonly used low calcium precursor in alkali activated concrete are fly ash and metakaolin. Inversely, these precursors are aluminosilicate rich which when brought in contact with alkali solution source will produce N-A-S-H gel. Fernández-Jiménez et al. (2005) proposed a model that describes alkali activation of aluminosilicates. Figure 2-4. When an aluminosilicate source is brought in contact with alkaline solution, the alumina and silica monomers dissolve in the solution. In the early stages, attributed to the Al^{3+} ion content from the alkaline solution and the more reactive Al dissolving quicker. The hydration process enters an Al rich phase where an Al rich gel called Gel 1 is produced also referred to as gelation process. Progressively more silicon ions will dissolve leading the Gel 2 formation through Si crosslinking within the gel. Finally, at complete saturation polymerisation of the N-A-S-H gel precipitates (Garcia-Lodeiro et al., 2015b; Shi et al., 2011). Besides N-A-S-H gel formation secondary reaction products formed are various zeolite types. Most common activators used are NaOH and $Na_2\mathrm{Si}O_3$. Carbonate based activators are less preferred due to lower alkalinity resulting in lower strength. Furthermore, low calcium precursors are often thermal and steam cured as strength development is low at room temperature (Bernal et al., 2014).

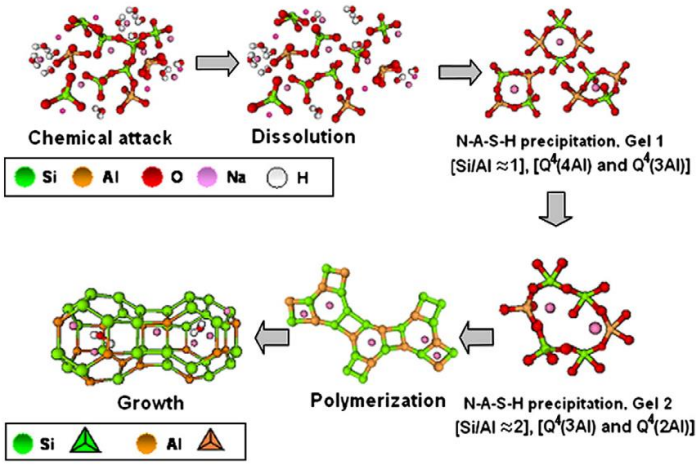

Figure 2-4 Theoretical Model (Shi et al., 2011)

Hybrid

Most hybrid alkaline cements contain blend of Portland cement with addition of supplementary cementitious material (SCM) such as; BFS and FA. These blends are characterized by having important chemical composition of CaO, SiO_2 and Al_2O_3 above 20% (García-Lodeiro et al., 2012). The reaction products are heavily dependent on the chemical composition of the blend and the reaction environment. The production of either N-A-S-H or C-A-S-H is heavily reliant on the Ca and pH values. Higher pH environment, due to alkaline type and or concentration used will result in predominantly degradation of N-A-S-H into C-A-S-H production (Garcia-Lodeiro et al., 2011), Figure 2-5. Conversely, the production of C-S-H gel is prevailing under lower alkalinity (Yip et al., 2005). Although, when consider longer time frames the formation of C-A-S-H is favoured. With C-S-H developing into C-A-S-H under Al presence and N-A-S-H developing into C-A-S-H under the presence of Ca (García-Lodeiro et al., 2013).

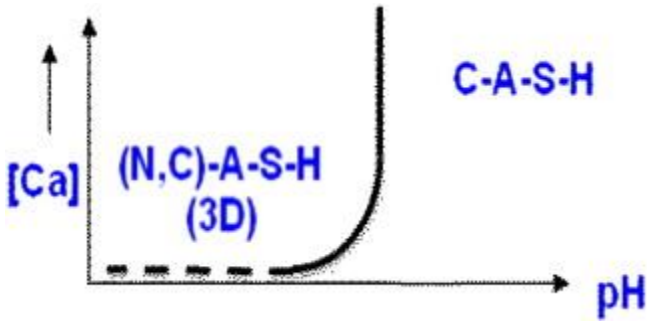

Figure 2-5: Hybrid systems hydration product model (Garcia-Lodeiro et al., 2011)

2.2 Material properties

Understanding how material properties vary based on the composition of AAC, particularly the choice of precursors and activators, is pivotal to understanding its bond behaviour. Additionally, material properties such as volume stability and durability, which are influenced by both composition and curing conditions, play a crucial role in overall performance. The literature review in this chapter will aim to provide a better understanding of these characteristics, with particular emphasis on AAS, as this is the focus of the current study. Understanding the material properties is key in order to comprehend the bond behaviour, as this directly depends on the mechanical characteristics of the concrete.

The following table provides a summary of the key literature discussed in the upcoming sections, highlighting their important aspects.

Material properties					
Mechanical properties					
Reference	**Precursor**	**Activator**	**Curing**	**Variable**	**Test**
(Collins & Sanjayan, 2001)	BFS	Na2SiO3	Bath: saturated lime 23°C Sealed: 23°C Exposed: 23°C, RH = 50%	Curing condition	Sorptivity Porosity Microscope: crack f_{cd} up to 1 yr
(Nath & Sarker, 2014)	FA/BFS	NaOH Na2SiO3	Ambient: 20°C, RH = 70%	Activator content: 35/40% BFS content: 0/10/20%	f_{cd} f_{ct}
(Topark-Ngarm et al., 2015)	FA Class C	NaOH $NaSiO_3$	1d steam cured 60°C Controlled room 23°C	Activator molarity: NaOH 10/15/20 M Activator ratio S:H: 1 and 2 Concrete strength class f_{cd} Curing type: heat or ambient	Pull out
(Wardhono & et al., 2017)	BFS FA Class F	NaOH 10/15 M Na2SiO3	Room temp. 23°C 1d AAF: water-cured 23°C 6d -room temp till test AAS: heat cured 80°C - room temp till test	AAC: AAF / AAS	Ultrasonic, water permeability and absorption, SEM X-Ray, f_{cd} f_{ct} f_{fl} E
(Boopalan & Rajamane, 2017)	FA/GGBS 75/25 – 50/50 Helix rebar	NaOH $NaSiO_3$	3d wet covered Ambient cured till 28d	Rebar Ø12-16mm (ribbed) Binder FA/GBFS ratio AA/B + Concrete strength class f_{cd}	Pull out
(Prinsse et al., 2020)	FA/BFS	NaOH 4M Na2SiO3	Moisture: 20°C, RH = 95% 28d Drying: 20°C, RH= 55% till test	BFS amount: 50 / 100% Curing condition: standard (no drying) vs drying	Microscope f_{cd} f_{ct} E 4PB
Zhang et al. (2022)	BFS	NaOH Na2SiO3	Mould: 1d 25°C Moisture: 20°C, RH= 95% till 7, 14 or 28d Drying: 20°C, RH= 55%	Curing age: 7/14/28d Curing condition: standard (no drying) vs drying	Workability f_{cd} f_{ct} E ν ε_{cr} ε_{sh} mass loss, carbonation, freeze thaw, chloride
(Abdulrahman et al., 2022)	FA Class C	NaOH 14M $NaSiO_3$	Ambient curing	AA/B ratio - f_{cd} Concrete cover to bar ratio c_v/d_b	Pull out
Volume stability					
(Collins & Sanjayan, 2000)	GGBFS Gypsum 2% vs OPC slag	Na2SiO3 Hydrate lime: Ca (OH)2	Temp: 23 °C and RH: 50%	AASC vs OPC slag	Shrinkage Micro: pore size
(Kovalchuk et al., 2007)	FA Class F	NaOH Na2SiO3	Covered: 95 °C Dry: 150 °C Steam: 95 °C RH 100%	Curing conditions	XRD, FTIR and Si MAS-NMR f_{cd}

(Melo Neto et al., 2008)	GBFS	Na2SiO3	Dry room: 24°C, RH = 50%	Silica modulus SiO2/Na2O =1.7 with Na2O: 2.5,3.5 and 4.5% by slag weight	Shrinkage: dry/auto Pore size
(Sagoe-Crentsil et al., 2013)	FA Class F	NaOH Na2SiO3	Steam cured: 65 °C 6hr Ambient: 23 °C, RH = 100%	Curing age Loading	Dry shrink. Creep 52wk f_{cd}
(Un et al., 2015)	GGBFS / FA 380-20 kg/m3	Na2SiO3	Lime bath 6d 23°C Chamber 23°C, RH = 50%	Curing cond.: bath/ bath + dry Curing time: 7/14/28 days Sus. loading app. Time 14/28 days	Sus. Load 40% Load at 14d/28d f_{cd} f_{cf} 4PB
(Castel et al., 2016)	FA/HPA/GBFS Class F 85.2-14.8%	NaOH 12M Na2SiO3	Shrinkage Creep 1D40 O 3D40 O 1D80 O 7D80 W 3D40 O O = oven 7D80 W W = water	Curing age: 1/3/7 days Curing Temp.: 40/80 °C	Dry shrink. /Creep Both 90d f_{cd} E at 28d
(Ye & Radlińska, 2016)	GBFS	NaOH 4M	Drying: varying RH, T = 23°C	Relative humidity RH: 11/30/50/70% 70-140 days	XRD SEM N-sorpotion Moisture, shirnk.
(Z. Li et al., 2020)	FA/GBFS 50/50% BFS 100%	NaOH Na2SiO3	Sealed: 20°C	Chemical shrinkage Relative humidity RH Elastic modulus evolution E FA/GBFS ratio	XRD FITR Thermometric Shrinkage E
(Humad et al., 2021)	BFS High-MgO	Na2SiO3 Na2CO3	Heat: 24h 65°C Ambient: 20°C, RH = 40%	Curing cond.: Heat / Ambient Activator: SS, SC, SS/SC Carbonation:	Shrinkage 52wk Creep 52wk Setting/Slump f_{cd} 52wk XRD/SEM
Durability					
(Albitar et al., 2017)	FA Class F	NaOH 14M $NaSiO_3$ S:H=1.5	Ambient cured 84d (No heat curing used for FA, hence longer curing time needed)	Concrete cover to bar ratio c_v/d_b: 2 - 7.8 Mass loss corrosion level 0 - 85% Compressive strength f_{cd} (c_v/d_b: $r$ebar Ø 12–16 mm ribbed)	Pull out
(Farhan et al., 2018)	FA/GGBFS	NaOH $NaSiO_3$	Ambient curing 28d	Type of steel fibre V_f: MIS/DES/HYS (Ribbed Ø12 mm)	Pull out

2.2.1 Mechanical properties

The material development in AAC is heavily dependent on the precursor. Wardhono and et al. (2017) compared the time dependent material properties of AAS to AAF concrete. Interestingly, for AAS a reduction in elastic modulus and flexural strength was observed, while the compressive strength remained relatively constant. Similar findings were later reported by (Prinsse et al., 2020; Zhang et al., 2022), as previously mentioned. In contrast to this, the fly ash-based samples displayed increased material properties over time.

Fly ash-based alkali-activated concrete (AAF) has low strength development under ambient curing conditions as the hydration reaction is weakened due to the decreasing amount of cementitious minerals. Slow pozzolanic reactions and lack of calcium content also hamper the strength development (Li et al., 2017). Therefore, most researchers gave insight into material properties and bond behaviour of heat cured AAF. Blended mixtures of fly ash and granulated ground blast furnace slag (GGBFS) or high calcium fly ash (HCFA) were also considered to enhance the strength

development without the need for heat curing. Nath and Sarker (2014) reported that the addition of GGBFS enhanced the compressive strength, while simultaneously diminishing setting time and workability as slag content increased. Topark-Ngarm et al. (2015) found similar results with HCFA having shorter setting time and continued strength gain due to the presence of calcium and hence the formation of CSH hydrates.

The use of sodium hydroxide ($NaOH$) and sodium silicate ($Na_2\mathrm{Si}O_3$) are almost exclusively used as activators in studies conducted on the bond behaviour. The preference for sodium-based activators is due to their inexpensiveness compared to other options as potassium hydroxide (KOH) and potassium silicate (K_2SiO_3). Furthermore, studies indicate that the combination of $Na_2\mathrm{Si}O_3$ and $NaOH$ result in better material properties (Ryu et al., 2013; Xin et al., 2014).

The manner in which activator concentration, ratio and activator to binder ratio effects the material properties, and in turn influence the bond behaviour was investigated. Humad et al. (2021) studied the influence of activator type on the material properties of AAS. Reduction in compressive strength was observed for sodium carbonate (Na_2CO_3) activated specimens. While sodium silicate ($Na_2\mathrm{Si}O_3$) activated specimens had slight progression in strength over time. Higher molarity of $NaOH$ was found to increase strength, but at high $NaOH$ concentration of 20M the strength decreased (Topark-Ngarm et al., 2015). Abdulrahman et al. (2022) found that reduction of alkaline-activator to binder ratio (AA/B) for HCFA increased the material properties which in turn had a positive effect on the bond strength. Boopalan et al. (2018) noted that the larger activator molar ratio SS/SH contributes towards denser interfacial transition zone (ITZ), a stronger ITZ correlates to higher compressive and tensile strength and thus also better bond strength.

2.2.2 Volume stability

Curing condition has great impact on the microstructure development of AAC, consequently its material properties are also affected. Kovalchuk et al. (2007) compared the influence of different curing conditions on the microstructural and material properties of AAF. Three different curing regimes were adopted, including covered (95°C), moisture (95°C/100 % RH) and dry (150°C) curing. Dry cured samples had the largest porosity and lowest compressive strength compared to its counterparts. Castel et al. (2016) studied the drying shrinkage and creep behaviour of AAF exposed to curing ages up to 7 days under curing temperatures of 40℃ and 80℃. Specimens exposed to prolonged 80℃ heat curing for 7 days showed slightly better shrinkage performance compared to CC and significantly smaller creep. Heat treatment appears to reduce the shrinkage in spite of increased capillary tension due to smaller pore size in AAF concrete. Likewise, a long-term study spanning 52 weeks found reduced drying shrinkage and creep for AAF compared to OPC concrete (Sagoe-Crentsil et al., 2013). Specimens were heat cured (6 hr at 65°C) and subsequently stored in a controlled environment (23°C/100 % RH) up to test age.

Regardless of activator or curing condition AAS has higher shrinkage than conventional concrete. Melo Neto et al. (2008) found that AAS tends to have a higher autogenous shrinkage compared to CC. Most drying and autogenous shrinkage occurs at early ages, with autogenous shrinkage increasing with higher SiO_2 content due to more intense hydration. This is because sodium silicate affects material properties, porosity, and the degree of hydration, all of which influence autogenous shrinkage. The intensified hydration from increased sodium silicate leads to more chemical shrinkage, which, along with high capillary pressure from self-desiccation, contributes to the significant autogenous shrinkage in AAS. However, heat-cured specimens experience less shrinkage than ambient-cured ones. This is due to the fact that the majority of moisture loss occurs during heat

curing. Hence, mitigating shrinkage over time (Humad et al., 2021). Un et al. (2015), demonstrated the impacted of curing condition on the creep behaviour of AAS. Specimens that remained under bath curing condition had less creep compared to samples that were bath cured and subsequently exposed to drying. The former samples had denser pore structures therefore less creep.

Collins and Sanjayan (2000) suggested that the high drying shrinkage of AAS is not necessarily attributed to moisture loss, as OPC had more weight loss than AAS while shrinkage was much smaller. Rather an explanation is found in the fact that AAS has larger proportion of pore sizes within mesopores limits compared to OPC, thus finer. Similar pore size proportion was reported by Melo Neto et al. (2008) as well. The smaller radius of the menisci will result in larger negative pressure within the pores causing greater contraction of the matrix. Ye and Radlińska (2016) compared the shrinkage of AAS at differing relative humidity concentrations. The high shrinkage of AAS was attributed due to the incorporation of alkali cations in the C-A-S-H gel, making the structure more irregular. Hence, easier to collapse and redistribute upon drying compared to C-S-H gel. Z. Li et al. (2020) suggested that self-desiccation is not the only process driving autogenous shrinkage. But rather due to the reduction of the concentration of ions leading to a reduction in steric-hydration force. As a result, the gel particles approach closer to each other forming a denser microstructure.

2.2.3 Durability

The durability of AAC is crucial when evaluating the long-term lifespan of constructions. The corrosion of reinforcement in concrete lead to crack formation and a decrease in bond strength, ultimately compromising the structural integrity of concrete structures. The corrosion resistance of AAF concrete bond strength was evaluated by Albitar et al. (2017). The accelerated corrosion procedure involved immersing the samples completely in a 5% sodium chloride aqueous solution. A slower decline in bond strength was seen in AAF concrete with corrosion levels between 5% and 30% compared to OPC concrete. The elevated tensile strength of AAF concrete was believed to facilitate increased corrosion volume expansion before cracking. Consequently, this might be responsible for the higher bond capacity. The incorporation of fibres in a study by Farhan et al. (2018) shown that fibre inclusion mitigated the decline in bond strength when subjected to an accelerated corrosion procedure in a seawater bath. The use of fibres enhanced the tensile strength of the concrete, hence diminishing early-age cracking, which improved resistance to chloride intrusion and augmented corrosion resistance. Zhang et al. (2018) assessed resistance to increased temperatures. At temperatures of 300°C and above, AAC concrete has substantial bond breakdown, accompanied by a significant decrease in splitting strength.

Creep effects are an important consideration when evaluating the long-term durability of structural elements. Creep refers to the progressive deformation of concrete over time, which can lead to increased deflection and, in the long term, may adversely affect the structural integrity of the elements. The AAS used in this study has been shown to exhibit creep levels twice as high as those of CC with similar strength (Zhang et al., 2022). This elevated creep is attributed to the characteristics of the C-A-S-H gel formed during the hydration process (Ye & Radlińska, 2016). However, the higher creep and relaxation effects in AAS help counterbalance its high autogenous shrinkage, thereby mitigating internal stress development and reducing the risk of cracking (Li et al., 2021; Zhenming Li et al., 2020).

3. Bond Behaviour in Concrete

The main objective of this chapter is to present a comprehensive review of bond behaviour in concrete, with a specific focus on understanding the factors that influence bond strength. This chapter begins by defining key concepts such as bond stress and bond transfer mechanisms. A clear understanding of these concepts is crucial for interpreting experimental results and advancing the understanding of how bond strength behaves in different conditions. Following this, a state-of-the-art on bond behaviour of AAC is presented.

3.1 Introduction

3.1.1 History

Earliest implementation of embedded steel on concrete dates back to 1877. At that time, it was believed that cast and wrought iron beams were 'fireproof'. However, Hyatt (1877) vitiated this fallacy. Hereupon, Hyatt proposed covering the iron girder with concrete in order to provide better fire resistance qualities. It was Hyatt himself who proved that by omitting the web and upper flange from the beams, and in place substituting the bottom flange for a flat bars or ties could result in equal resistance. The iron would act as tension resistance whereas the concrete would serve as the compressive member. This novel system at that time, is still the basis of modern reinforced concrete member design today.

Research on the bond resistance between concrete and steel gained traction already starting from the early 1900's. The interaction between concrete and the embedded steel or bond quality, was measured by pullout tests. Where the displacement or slippage of the steel was measured as means to determine the bond quality. This ability of reinforced specimens to resist slippage was first referred to as bond resistance by Menzel (1939). This initial understanding of the bond interaction between concrete and steel led to further research to comprehend all different variables subject in influencing the bond resistance.

3.1.2 Bond stress

Bond stress refers to the shear stress acting parallel to the rebar surface and the surrounding concrete matrix interface. The bond stress is responsible for the transfer of forces between the concrete matrix and the steel rebar. The change in bond force and steel stress go hand in hand, e.g. increasing bond stress results in increased steel and concrete stresses (Ferguson, 1966).

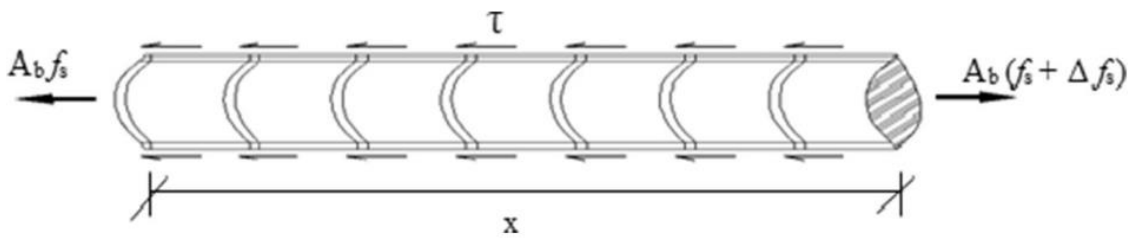

Figure 3-1: Bond equilibrium reinforcement model (MacGregor et al., 1997)

The analytical model for bond stress is derived in accordance with Newton's 3rd law. The internal forces in a loaded reinforced concrete element are in equilibrium. This opposite but equal forces are the steel force F_s and the surrounding concrete bond force F_b, $F_s = A_s f_s$ Eq. 3-1Eq. 3-1 and Eq. 3-2. Therefore, by equating these two forces (Eq.3-3) and rearranging to the formula the bond stress u_b is derived, Eq. 3-4. Where A_s is the steel area, f_s is the steel tensile stress of the rebar, d_b is the rebar diameter and L is the embedment length of the rebar.

$$F_s = A_s f_s$$ *Eq. 3-1: Steel stress*

$$F_b = \tau_b \, \pi d_b L$$ *Eq. 3-2: Bond stress*

$$\tau \, (\pi d_b x) = A_s(f_s + \Delta f_s) - A_s f_s$$ *Eq. 3-3: Bond equilibrium*

$$\tau = \frac{A_s \Delta f_s}{\pi d_b x} = \frac{d_b \Delta f_s}{4L} \left[{}^{N}/_{mm^2} \right]$$ *Eq. 3-4: Bond stress*

The bond behaviour is not constant over the rebar profile. Particularly in the case of a reinforced concrete beams, where the length of the rebar is significantly greater, compared to smaller pull-out tests. In these reinforced beams, at the onset of flexural cracks the bond stress will vary significantly. At the crack, there is no steel-concrete interaction anymore. Therefore, no bond stress. Here the steel will carry all the tension force. Because there is no bond interaction the stresses can no longer be carried jointly. Therefore, the concrete compressive stress also increases at the same time. Adjacent to the crack the steel stress reduces as bond stresses are activated again, Figure 3-2.

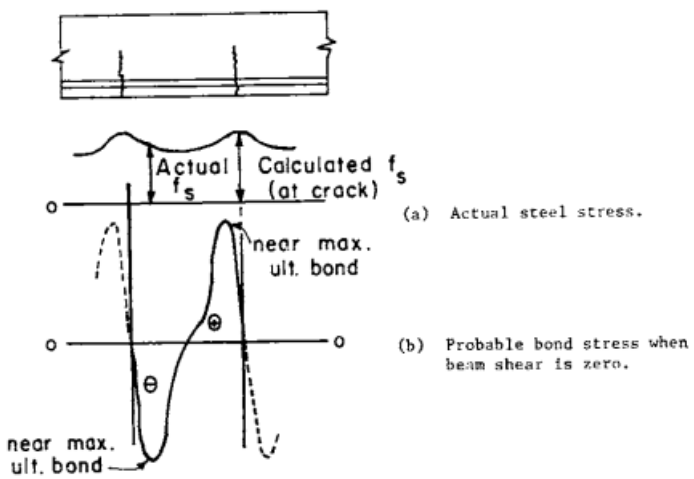

Figure 3-2: Lutz and Gergely 1967 (check its source Mains)

The theoretical model defined below Eq. 3-5 represents an average bond stress along the profile. When examining short length specimens (current study), this average bond stress will resemble the real scenario more closely. Conversely, the longer the specimen, the lower the average bond stress will be. For the purpose of this study the theoretical average bond stress will be used.

$$u_b = \frac{A_s f_s}{\pi d_b L} = \frac{d_b f_s}{4L}$$ *Eq. 3-5: Average bond stress*

3.1.3 Bond mechanisms

As mentioned before bond is considered a surface shear stress around the bar surface and the concrete. These bond stresses are responsible for the transfer of forces from the bar to the concrete and vice versa. Bond force transferring mechanism consist of the following components:

- Chemical adhesions
- Friction
- Mechanical interaction steel bar and concrete matrix (bearing)

(Lutz & Gergely, 1967)

How and in what extend these components are present depends primarily on the rebar geometry and surface conditions. Plain rebars transfer bond forces primarily though chemical adhesions and friction between the rebar and the concrete surface. Initially the rebar segment closest to the loaded end will begin resisting the loading. This resistance as explained before, is primarily due to chemical adhesion, which is very localized. After exceeding this resistance, the bar will start slipping near the loaded end. This initial segment will only be resisted by friction resistance of the rebar against the surrounding concrete. The remaining bar segment, beyond the slip zone, remains mostly unstressed. With continued loading the chemical adhesion will fail along the rebar profile till reaching the rebar end. At this point pull out of the rebar may occur (Ferguson, 1966). In plain rebars mechanical interlocking contributes to resistance through the roughness of the bar against the concrete surface. Although, this contribution is limited to a much lesser extent.

Deformed bars are characterised by the lugs/ribs along the rebar surface. Deformed rebars were introduce to improve the bond resistance compared to plain rebar. Plain rebars, have the disadvantage that, after the chemical adhesion is surpassed, the remaining resistance over the failed segment is friction drag, which is smaller in comparison to chemical adhesion. This results in brittle failure. Were the rebar can be pulled out completely in most cases, leaving a hole in the concrete matrix.

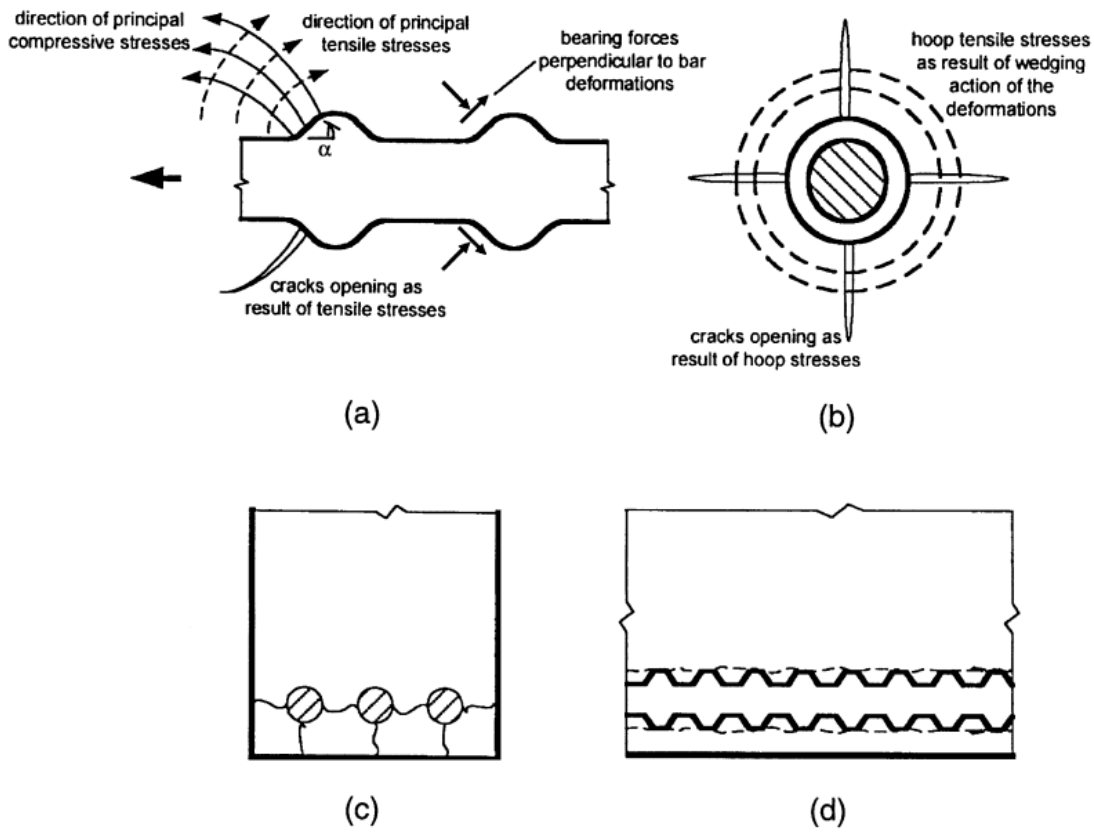

Figure 3-3: Bond bearing mechanism (Allen et al., 2003)

Due to the ribs present along the rebar profile in deformed rebars, the bond transfer mechanism is different, Figure 3-3. During initial loading the stresses are small, the bond between the bar and the concrete can still completely be transferred by chemical adhesion and mechanical interlock. Concrete and rebar undergo identical strain deformation; therefore, no slip will occur. The first instance of rebar slip happens when the chemical adhesion is exceeded. From then on mechanical interlock (bearing) will become the main bond transferring mechanism.

Unlike plain rebars, deformed rebars do not transmit bond stresses predominantly by friction at the onset of slip. In the case of plain rebars when the rebar starts displacing it will move relative to the surrounding concrete. Hence resulting in friction forces. Contrary, in the case of deformed rebars the surrounding concrete is being pushed as opposed to the rebar moving relative to the concrete. The manner in which either wedging action or concrete crushing occurs is heavily dependent of the deformed rib angle. Wedging is when, crushed concrete in front of the rebar rib is pushed. When rib face angles are larger than 90°, concrete crushing is nearly the only cause of slippage. Whereas there is some concrete crushing, rib angles less than 30° cause slippage because there is insufficient friction resistance. The optimal rib angles are found at 40-45°, where concrete crushing is followed by wedging action (Lutz & Gergely, 1967).

3.1.4 Bond Failure modes and behaviour

Bond failure is categorized into two distinct modes: pull-out failure and splitting failure. The occurrence of a specific failure mode is contingent upon numerous factors, including rebar type, concrete cover, bar spacing, bar diameter, embedment length, and the presence of transverse reinforcement. Plain rebars are more likely to fail by pull-out. Whilst, splitting failure is significantly more prevalent in deformed rebars (Anwar Hossain, 2008; Cui et al., 2020; Ferguson, 1966). The occurrence of splitting failure is unsurprising, as it directly results from the wedging of the concrete caused by the rebar ribs, as will be elucidated shortly. Although pull-out failure remains a possibility, it is more likely in instances with substantial concrete cover and smaller rebar diameter (Orangun et al., 1977).

With a thorough understanding of the bond mechanisms, the observed bond stress-slip behaviour can be understood. The bond behaviour will differ significantly based on whether the failure mode is pullout or spitting failure. The bond behaviour detailed in the following paragraph is illustrated in Figure 3-5.

In the early stages of bond stress-slip curves, the bond behaviour is similar regardless of the failure mode. Due to chemical adhesion the curves are steep as there isn't almost any slip yet. This behaviour corresponds to segment A. When the chemical adhesion is exceeded, the rebar will start slipping. In this stage mechanical interlocking is activated due to the rebar ribs pushing against the concrete. The bearing stresses from the rebar ribs exerted on the concrete will induce microcracks in the concrete (Vandewalle, 1992). The formation of microcracks enables the rebar to slip through the concrete matrix. Hence, the bond/slip curve is having a softer concave shape, segment B. An ongoing increase in external force will lead to significant concrete crushing. Slip will ensue as a result of the crushing of the porous concrete matrix. Thereafter, wedging of crushed concrete will follow. Ultimately causing significant slip of the rebar. In case of pullout failure this wedging action will not result in splitting cracks. With proper confinement the specimen will reach a higher bond resistance, Point E. Thereafter, a gradual decrease in the bond resistance is observed where the rebar is mainly resisted by friction, segment F. Continued slip reduces the embedded rebar length, with as consequence declining friction resistance.

Conversely, the wedging of the concrete is the principal cause of splitting cracks in instances lacking confinement. As the crushed concrete is being pushed outward radially in front of the rebar lugs. Consequentially radial tensile stresses will arise in the concrete matrix. When these stresses exceed the concrete tensile strength, longitudinal splitting cracks will occur (Tepfers, 1979), see Figure 3-4. At this moment as sudden decrease in bond resistance is observed, Point C. Depending on the concrete confinement either curve b or c will occur. With proper confinement cover these splitting cracks will be better resisted. Therefore, resulting in a less sudden bond stress decrease, curve c.

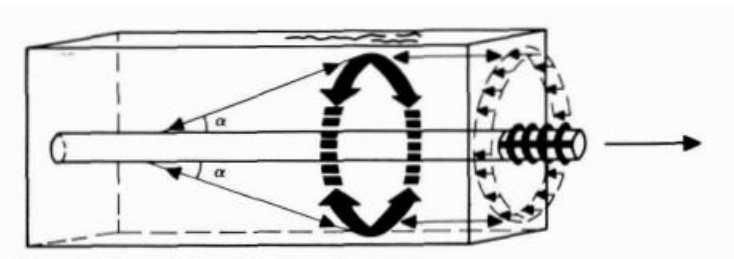

Figure 3-4: Radial hoop stresses due to wedging action (Tepfers, 1979)

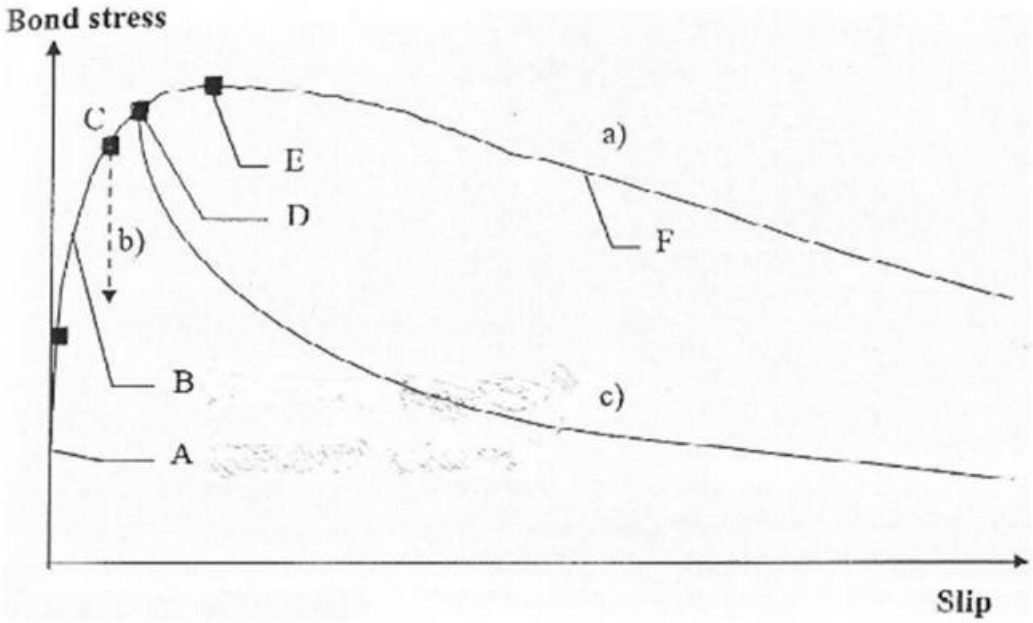

Figure 3-5: Bond-stress slip curve; (a) well confined concrete pull-out failure (b) unconfined concrete splitting failure and (c) confined concrete splitting failure (Sulaiman et al., 2017)

In the absence of splitting failure, pull-out failure produces the highest bond resistance. Moreover, the gradual decrease in bond strength is far safer. Consequently, pull-out failure is favoured over splitting failure.

3.1.5 Test type

There are various test methods used to gauge the bond strength of concrete. Either beam-end (Figure 3-6b), anchorage (Figure 3-6c) or splice (Figure 3-6d) testing are conducted on beam specimens. Whereas pull-out (Figure 3-6a) test is performed on cube or cylindrical specimens. The latter method is not the most accurate representation of the bond behaviour in structural elements. In this test while the rebar is being pulled the concrete is being compressed. This differs with bond behaviour in structural elements where the matrix surrounding the rebar is in tension. This compression of the concrete results in enhanced friction resistance of the rebar and greater splitting resistance of specimens. In contrast to the pull-out test, the beam test methods are more in line with the actual bond behaviour in structural elements. In study conducted by Sofi et al. (2007) where beam-end and pull-out methods were compared for AAF concrete. The beam-end test had a lower strength compared to the pull-out test specimens. Reflecting the effect of the pull-out specimens being in compression. Nevertheless, pull out test is still the most favoured method because of its simplicity and inexpensiveness.

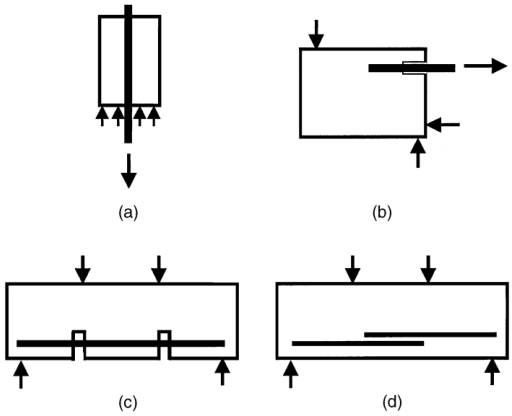

Figure 3-6: Pullout (a), Beam-end (b), Beam Anchorage (c) and Splice (d) test specimens (Allen et al., 2003)

3.2 Summary of State-of-the-Art report

Following chapter reviews, the literature on bond behaviour of AAC. All sources most relevant characteristics including precursor, activator, curing condition and research variables are summarized and ordered according to their most relevant parameter in Table 3-1. Insights gained from the literature review are presented for each parameter. The manner in which different variables like; concrete strength class, curing condition, concrete cover, reinforcement and fibre addition influence the bond behaviour is presented.

The following table provides a summary of the key literature discussed in the upcoming sections, highlighting their important aspects.

Table 3-1: Summary of state-of-the-art studies on bond behaviour of AAC

Bond Literature					
Reference	**Precursor**	**Activator**	**Curing**	**Variable**	**Test**
Curing condition					
(Castel & Foster, 2015)	FA/GGBFS FA Class F 85/15%	NaOH 12M $NaSiO_3$	2d: heat 80°C/ bath 80°C 7d: heat 40°C 1d/ bath 80°C Ambient cured until 28d	Curing age: 2d / 7d Rebar type: Smooth / Ribbed Ø 12 mm	Pull out
Concrete cover					
(Sarker, 2011)	FA	NaOH 14M $NaSiO_3$	Steam cured at 60 °C 24h Ambient curing till 28d	Concrete cover to bar ratio c_v/d_b Embedded length l_b 95-125 mm Water content/f_{cd} (Rib. rebar Ø 20-24 mm)	Beam-end
(Abdulrahman et al., 2022)	FA Class C	NaOH 14M $NaSiO_3$	Ambient curing	AA/B ratio - f_{cd} Concrete cover to bar ratio c_v/d_b	Pull out
Reinforcement					
(Sofi et al., 2007)	FA Class F 3 sources GGBFS	Na_2CO_3/SiO_2 Na_2O/SiO_2	Beam end: 12h steam – ambient 28d Pull out: 24h steam – ambient 28d	Fly ash type (source) Fly ash / slag ratio Concrete strength class f_{cd} Rebar Ø 12-16-20 mm (Coarse aggregate, w/b)	Beam-end Pull out
(Kim & Park, 2014)	FA/GGBFS	NaOH $NaSiO_3$	24h heat cured 70°C	f_{cd} : 20/30/40 MPa Rebar Ø 10-16-25 mm ($l_b = 5d_b$)	Pull out

(Maranan et al., 2015)	FA/GGBFS	NaOH $NaSiO_3$	Cured 28d	Rebar Ø 12.7 - 15.9 - 19 mm $f_y = 540MPa$ Embedded length l_b 5/10/15d_b + 300 mm (Sand coated ribbed GFRP rebars)	Pull out
(Albitar et al., 2017)	FA Class F	NaOH 14M $NaSiO_3$ S:H=1.5	Ambient cured 84d (No heat curing used for FA, hence longer curing time needed)	Concrete cover to bar ratio c_v/d_b: 2 - 7.8 Mass loss corrosion level 0 - 85% Compressive strength f_{cd} (c_v/d_b: $r$ebar Ø 12–16 mm ribbed)	Pull out
(Paswan et al., 2020)	FA/GGBFS Cass F 80/20% Helix rebar	NaOH $NaSiO_3$	Ambient curing 28d	Rebar Ø: 8,12,16 and 20 mm Surface condition: ribbed/plain /coatings Concrete cover c_v Embedded length l_b: 50/80/100/150mm T: 200,400,600,800°C (durability) Corrosion (durability)	Pull out
(Boopalan et al., 2018)	FA Class F GGBFS 80/20%	NaOH $NaSiO_3$	Ambient curing 35°C RH:65-85% 1d covered	Molar SiO2/Na2O ratio: 0.9-1.2 Rebar Ø 12-16-20 mm ($f_y = 700MPa$)	Pull out
(Cui et al., 2020)	FA Class F	NaOH 12M $NaSiO_3$ S:H=1.95-2.5	Heat cured 80°C Ambient cured till 28d	Rebar type: Ribbed/Smooth Ø 16 mm	Beam-end Pull out
(Subramanian & Solaiyan, 2021)	FA/GGBFS Class F FA Helix rebar	NaOH 8M $NaSiO_3$S:H=2.5	Ambient curing 28d	Rebar type: GFRP/BFRP/Steel	Pull out
(Romanazzi et al., 2022)	GGBFS/Silica fume/gypsum	Ingessil	28d	Rebar type: Steel (rib)/GFRP (sand coated) Rebar Ø: 12,16 mm Embedded length l_b: 2.5/5d_b	Pull out
(Kim & Park, 2014)	FA/GGBFS	NaOH $NaSiO_3$	24h heat cured 70°C	f_{cd} : 20/30/40 MPa Rebar Ø 10-16-25 mm ($l_b = 5d_b$)	Pull out
(Cui et al., 2022)	FA Class F	NaOH 12M $NaSiO_3$ S:H=1.95-2.5	Heat cured 80°C Ambient cured till 28d	Rebar type: Ribbed/Smooth Ø 16 mm	Beam-end
(Ma et al., 2023)	GGBFS/MK	NaOH 8M $NaSiO_3$	Ambient curing 28d	Compressive strength f_{cd} (AA/B: 0.40/0.50) Rebar Ø: 14,16 and 20 mm Rebar type: Epoxy coated/Steel Embedded length l_b: 5/7d_b	Beam-end
Fibre addition					
(Ganesan et al., 2015)	FA Class F Helix rebar	NaOH $NaSiO_3$	Steam cured 1d at 60°C	Fibre volume V_f: 0/0.25/0.50/0.75/1.0% Rebar Ø 10-12-16 mm	Pull out
(Zhang et al., 2018)	MK/FA	SiO_2/K_2O	7d 22°C RH95% OPC 28d	Rebar Ø: 10,12,14,18 and 25 mm Plain or Ribbed T: 100,300,500,700°C exposed 120min	Pull out
(Farhan et al., 2018)	FA/GGBFS	NaOH $NaSiO_3$	Ambient curing 28d	Type of steel fibre V_f: MIS/DES/HYS (Ribbed Ø12 mm)	Pull out
(Albidah et al., 2020)	MK	NaOH 20M $NaSiO_3$		Rebar type: Steel/GFRP (ribbed Ø: 12mm) AA/B: 0.4/0.5 and S:H=1.0/0.6 Fibre addition V_f = 2.5%	Pull out
(Peng et al., 2022)	FA/GGBFS 9:1/4:6/1:9 Class F FA	Na2CO3 $NaSiO_3$	Water bath 28d	Compressive strength f_{cd} (FA/GGBFS ratio) Embedded length l_b: 5/10/15d_b Fibre volume V_f: 0/1.0/2.0% Fibre type: Steel/PVA fibres Rebar Ø: 3,6,10 mm (CFRP)	Pull out

3.2.1 Influence parameters for bond behaviour

Material properties influence on bond

Concrete strength, particularly compressive and tensile strength, play a significant role in influencing bond behaviour. Numerous research has demonstrated a robust association between bond strength and the concrete compressive strength and concrete tensile strength (Albitar et al., 2017; Boopalan et al., 2018; Sofi et al., 2007). These higher mechanical properties can be attributed to the improved interfacial transition zone (ITZ) between the aggregates and binder paste in AAC, which enhances the adhesion necessary for effective force transfer between concrete and reinforcement (Sarker, 2011). However, this correlation between concrete strength and bond strength is not universal. For example, tests conducted by Kathirvel et al. (2017) showed that alkali-activated slag (AAS) exhibited greater bond strength compared to ordinary Portland cement (OPC), regardless of concrete strength grade or rebar diameter, due to stronger adhesion between the aggregates and the activator solution. Saranya et al. (2021) reported similar findings for blended dolomite (DM)-slag AAC. In some cases, despite similar compressive strengths, AAC has shown reduced bond strength, which can be attributed to differences in microstructure. For instance, (Mo et al., 2018) observed that POFA-based AAC, despite having similar compressive strength to OPC, exhibited reduced bond strength. This reduction was attributed to the higher porosity and less dense matrix of POFA-based AAC, underscoring that bond strength is influenced not only by the compressive strength but also by the microstructural characteristics of the concrete.

The influence of Concrete cover on bond

Several researchers investigated the influence of concrete cover to rebar ratio c_v/d_b on the bond strength of AAC. Sarker (2011) researched the bond strength of AAF for c_v/d_b 1.71- 3.40 and found that the normalized bond strength to compressive strength increased with increasing c_v/d_b for both AAC and OPC concrete. Similar findings were found in studies conducted by Abdulrahman et al. (2022) and Ma et al. (2023). These researchers attributed bond strength loss to a reduced concrete confinement i.e., lower concrete cover to bar ratio c_v/d_b resulted from increasing rebar diameter for same size specimens. Furthermore, it should be noted that splitting failure was more common in cases with low c_v/d_b.

Reinforcement influence on bond

Various studies have researched the impact of reinforcement on the bond strength, focusing on key aspects such as rebar diameter, embedded length, the distinction between ribbed and plain rebars and reinforcement type. Most research indicated stronger bond strength with decreasing rebar diameter (Kathirvel et al., 2017; Sofi et al., 2007). Maranan et al. (2015) suggested that larger rebars have greater Poisson effect, resulting in worsened interface that led to reduced bond strength. Under direct pull-out test bond strength increased for embedded length (l_b) up to $5d_b$ (Paswan et al., 2020). Further increase in embedment length to $7d_b$ resulted in decrease in bond strength (Ma et al., 2023). Similar decrease in bond strength with increasing embedded length was confirmed by (Maranan et al., 2015; Peng et al., 2022).

Specimens with shorter l_b tend to fail by pull out, while those with longer l_b fail by splitting. Specimens with longer l_b have enough embedment length for the development of radial stresses and can induce longitudinal cracks. These cracks weaken the concrete's compressive confinement, which explains why the bond strength is lower (Maranan et al., 2015). Similar bond behaviour was found for FRP bars (Peng et al., 2022) and in case of epoxy coated rebar (Ma et al., 2023).

The reinforcement type has great influence on the bond behaviour. Ribbed rebars have substantial larger bond strength as the bond transfer mechanism occurs mainly through bearing resistance of the ribs against the surrounding matrix. Whereas plain rebars bond transfer mechanism occurs through chemical adhesion and friction which are much weaker compared to bearing resistance. This difference in bond mechanism is reflected in a study conducted by Paswan et al. (2020) where ribbed rebars had a 234% greater bond strength compared to plain rebars. Overall AAC has superior bond strength than conventional concrete in case of ribbed steel rebars (Albitar et al., 2017; Castel & Foster, 2015; Kathirvel et al., 2017).

Plain rebars was found to perform slightly better in OPC concrete compared to blended slag and fly ash based and AAC (AASF), according to Castel (2017). This indicated that chemical adhesion in this AAC mixture is not better than OPC. Yet later studies demonstrated otherwise. Boopalan et al. (2018) showed that the adhesive bond strength of comparable AASF was 30% -80% greater compared to OPC concrete. Similarly, plain bars in AAF had an average of 21% stronger adhesion than OPC for solely fly ash based AAC according to (Cui et al., 2020).

Moreover, ribbed rebars experienced splitting failure, whereas pull-out failure was more common with plain rebars (Cui et al., 2020). Subramanian and Solaiyan (2021) compared ribbed glass fibre-reinforced polymer (GFRP), basalt fibre-reinforced polymer (BFRP) and steel reinforcement for blended AAC (AASF). Ultimate bond strength was higher for FRP reinforcement compared to steel. Furthermore, FRP had less slip, but more ductility compared to steel. Still, the bond/slip behaviour for FRP in AAC was similar to conventional concrete.

Influence of fibre on bond

Incorporation of steel fibres has been found to increase the mechanical properties of AAC, leading to better bond strength performance. Ganesan et al. (2015) studied the bond behaviour of AAF under increasing fibre content for differing rebar diameter (d_b). The bond strength and slip increased for both d_b 10 and 12 mm, whereas for d_b of 16 mm, the bond strength decreased. Farhan et al. (2018) investigated the bond behaviour for three distinct types of fibres in AASF concrete. The addition of fibres improved the bond strength in accordance with improved compressive and tensile strength. For metakaolin based AAC, the addition of fibres significantly increased the bond strength of GFRP reinforced AAC, such that the bond strength was comparable to steel reinforced concrete. Whereas in plain GFRP reinforced AAC the bond strength was much lower compared to steel (Albidah et al., 2020). However, the addition of fibres was found to have marginal effect on the bond strength according to Peng et al. (2022).

Curing conditions

Curing conditions are significant in determining the material properties of concrete and in addition the bond behaviour. Castel and Foster (2015), assessed the effect of curing age on the bond strength for AASF. Bond performance for AASF concrete was found to be similar to OPC based concrete subjected to 48 h of heat curing. Extending heat curing till 7d enhanced bond strength with 25%. A relation between bond strength and material properties could be seen. With extended heat curing significant gain in compressive strength was achieved. Although the elastic modulus and tensile splitting strength did not increase much.

Prinsse et al. (2020) compared the material properties of AAC based on their slag content using AASF (50%-50% GBFS/FA) and AAS (100%GBFS) exposed to drying conditions. The compressive strength for both AAC types improved slightly over the span of 1 year. On the other hand, both AAC types had decreasing E-modulus. Noteworthy, the AAS had greater decrease over time indicating higher sensitivity to drying for slag based AAC. Zhang et al. (2022) studied the material properties for self-compacting AAS exposed to drying up to 3 months. All specimens exposed to drying resulted in

decreased E modulus. Later on, Pineda (2022) confirmed same material properties findings when using same AAC developed in the Microlab-TU Delf. Furthermore, long term structural behaviour of prestress beam was tested. Interestingly, a beam subjected to its self-weight for 9 months failed due to anchorage failure. It was suggested that the high creep and shrinkage present in AAS causes reduced Hoyer affect resulting in decrease of bond strength. Still the research on curing age and condition effect on bond is limited.

Applicability of code

Given the absence of design standards for AAC, it is useful to compare its behaviour with the established design standards of its analogous counterpart, conventional concrete. Although AAC differs from traditional concrete in terms of chemical reactions and matrix creation. The current codes, AS 3600, EC2, and ACI-02, have been shown to be conservative in their predictions of the bond behaviour of steel or FRP reinforced AAC in most cases. Specifically regarding the embedded length (l_b), reinforcement diameter (d_b), and concrete cover (c_v) utilised in the respective studies (Albidah et al., 2020; Saranya et al., 2021; Sofi et al., 2007; Topark-Ngarm et al., 2015). However, there are exceptions, (Luan et al., 2021) proved that the characteristic bond strength value for low calcium FA is lower in some cases. Others adjusted existing models to provide a more precise depiction of bond strength. Peng et al. (2022) presented a revised model to the somewhat conservative ACI 440 model to more appropriately represent the bond strength of CFRP. To forecast the binding strength of steel and GFRP bars in fibre-reinforced AAC, Albidah et al. (2020) introduced a modified Orangun model. AAC has demonstrated similar bond behaviour to conventional concrete (CC), following comparable trends in bond-slip relationships. The bond behaviour curve of AAC can also be characterized by five distinct stages: (1) an initial linear increase, (2) a non-linear phase, (3) splitting or pull-out bond failure, (4) a non-linear decrease in bond resistance, and (5) a constant residual frictional resistance. While existing bond behaviour models, such as the CEB-fib model, are applicable to AAC, minor adjustments are recommended to account for AAC's unique properties (Abdulrahman et al., 2022; Albitar et al., 2017; Castel & Foster, 2015).

3.2.2 Tension stiffening effect

Tension stiffening refers to the ability of concrete to carry tensile stresses between cracks, contributing to the overall stiffness of a reinforced concrete member and reducing deflections. This mechanism is essential for controlling crack formation, development, and overall deformation. All of which are vital for the serviceability limit state (SLS) of concrete structures. The degree of tension stiffening is influenced by the bond strength between concrete and steel and the concrete's tensile capacity (Bischoff, 2001). Understanding these aspects is critical for future applications of AAC in structural elements.

The tension stiffening effect can be studied directly through tension stiffening tests, which involve applying a tensile load to both ends of a reinforced concrete prism specimen. Albitar et al. (2018) conducted such tests on low-calcium FA and FA/BFS composite AAC specimens, demonstrating that both of these AAC's exhibited similar behaviour to CC. It was found that increasing the c_v/d_b improves the tensile capacity of the concrete, delaying crack formation and leading to a stronger tension stiffening response (Abdulrahman et al., 2023; Albitar et al., 2018; Khalfallah & Guerdouh, 2014). This is consistent with findings for conventional concrete (Dawood & Marzouk, 2011; Lee & Kim, 2009).

Tension stiffening is more commonly studied indirectly using four-point bending tests. Studies have shown that AAF exhibits similar flexural performance to CC (Nguyen et al., 2016). Furthermore, AAC

has been shown to have higher load capacity compared to CC (Kumar et al., 2017; Shah & Shah, 2017). However, some contradictory findings have been reported. For instance, Shah and Shah (2017) observed larger deflections in AAF and AASF compared to their CC counterparts, along with differences in failure modes. FA-based AAC exhibited brittle failure, while CC displayed more ductile behaviour (Yost et al., 2013).

Tension stiffening is significantly affected by shrinkage, where drying shrinkage has been shown to reduce the stiffness of the concrete members (Bischoff, 2001). Ambient-cured AAS has shown to be detrimental to the tension stiffening, due to the effects of drying shrinkage (Tran et al., 2019). The addition of steel fibres, however, has proven effective in counteracting the effects of drying shrinkage. Reducing crack width and improve tension stiffening, ultimately leading to enhanced load-carrying capacity (Ganesan et al., 2014; Tran et al., 2019). Nonetheless, the influence of drying shrinkage on the overall structural performance of AAC requires further investigation.

3.3 Conclusion

Having explored the various factors impacting bond strength in alkali-activated concrete (AAC), it is essential to emphasize how these factors relate to the present study, particularly the key parameters of interest: curing conditions, curing age, and reinforcement type. These elements play a significant role in shaping the bond behaviour of AAS.

While compressive and tensile strengths are crucial in determining bond strength, the specific chemical reactions and matrix structure of the AAC mixture significantly influence bond characteristics. In particular, the impact of drying on AAS is noteworthy. The bond strength of AAS has been observed to decrease over time, indicating a higher sensitivity to drying for slag-based AAC.

Furthermore, the difference in rebar diameter between steel and prestressed concrete results in a reduced concrete cover-to-rebar diameter ratio c_v/d_b. This reduced confinement, combined with increased rebar diameter, may negatively affect the bond strength for prestressed reinforcement. Similarly, with a bond length of $5d_b$ for both reinforcements, the larger bond length for prestressing strands may be more prone to splitting failures, as suggested by the literature.

4. Experimental Program

This chapter aims to address a key sub-question: What is the optimal method for conducting a pull-out test? The experimental setup is designed to investigate the effects of curing age, curing conditions, and reinforcement type on bond behaviour of AAC, as outlined in this chapter. Firstly, the implementation of variables and the experimental approach are presented. Subsequently, various iterations undertaken to establish the optimal setup and testing procedures are described in Section 4.3. Finally, the optimal test setup and procedure are determined and presented in Section 4.4. Besides, procedural decisions made based on preliminary tests are clarified in Section 4.4.3.

4.1 Overview

4.1.1 Variable Implementation and sub-objectives

As aforementioned, the research on the time-dependant bond behaviour of AAS is limited. Besides, various studies reported the degradation of mechanical properties of AAS over time exposed to drying conditions (Prinsse et al., 2020; Wardhono & et al., 2017), which might impact the bond behaviour and hamper the adoption of AAC for structural applications in practice. Furthermore, most of the studies focused on the bond behaviour between AAC and conventional rebar. While there is limited research on the bond behaviour of prestressing strands.

Thus, the main parameters investigated in this study include curing condition, curing age and reinforcement type. The implementation of variables in the experimental plan is outlined as follows.

Curing condition

The impact of curing condition on material properties of AAS has been reported by several researchers (Pineda, 2022; Prinsse et al., 2020). AAS exposed to drying has increased moisture loss paired with greater porosity. This lead to a reduction in compressive strength (Kovalchuk et al., 2007). Besides, some AAS mixtures illustrates high creep and shrinkage (both dry and autogenous) when exposed to drying, in comparison to CC (S. Zhang, 2021; Un et al., 2015). However, research on the effects of curing condition on bond behaviour is still limited. Therefore, two different curing conditions are considered: **moisture cured** (22°C and 99% RH) **and dry curing** (20°C and 55% RH). The effects of drying on the bond behaviour of AAS are studied by comparing the results obtained from the samples exposed to drying against that gained from the moist-cured specimens.

Curing age

Under drying curing conditions, AAS material properties will decrease over time. However, research in the bond behaviour of AAS is limited to short time frame studies (mainly on 28 days). Therefore, gaining better understanding on the development of bond behaviour of AAS over time requires further research. The samples are tested at two different curing ages: **28 days and 84 days.** Additionally, only CC specimens undergo testing at the age of **168 days**.

Reinforcement type

In order to gain insight on the bond behaviour between AAC and different types of reinforcement, not only ribbed rebar but also prestressing strands are included in this study. Extensive studies have been conducted on the impact of steel reinforcement on the bond behaviour of AAC. Hence, only a fixed **steel ribbed rebar diameter of Ø 8 mm** is used. On the other hand, research in bond behaviour

using prestressing strands is limited. Therefore, this research will consider the bond behaviour of plain 7-wire **FeP1860 prestressing strand** with Ø 12.9 mm. Note that no prestress is introduced in the tests.

4.1.2 Approach

The experimental program consists of two main phases: a preliminary test series and the main experimental series. First, the preliminary test is performed. The purpose of this preliminary series is to develop an optimal testing method for pull-out tests. Pull-out test is preferred over other bond test methods, detailed in Section 3.1.5, for their simplicity and effectiveness to measure the bond strength. The optimal testing method is developed by evaluating the effects of different sample designs, test setups, and procedures on the results. Following this, the main experimental program begins. The objective of the program is to evaluate the bond strength and slip behaviour of AAS over time through pull-out tests. The study specifically looks into the impact of curing conditions, curing age, and reinforcement type on the bond behaviour by comparing AAS samples to reference CC samples.

An overview of the experimental program is depicted in Figure 4-1, while Figure 4-2 illustrates the configuration and specifications of each series. Note that, due to certain issues encountered during the casting of the main experiment (detailed in Section 4.3.3), a segment of the series failed (AAS100-S). Consequently, a separate series titled 'Size & Configuration' was conducted to determine the cause of the failure.

In Figure 4-3, the main experimental program is visualized, illustrating the implementation of the research variables: curing condition, curing age, and reinforcement type. Besides the pull-out test, mechanical tests are performed to determine the compressive strength and tensile splitting strength properties of the samples.

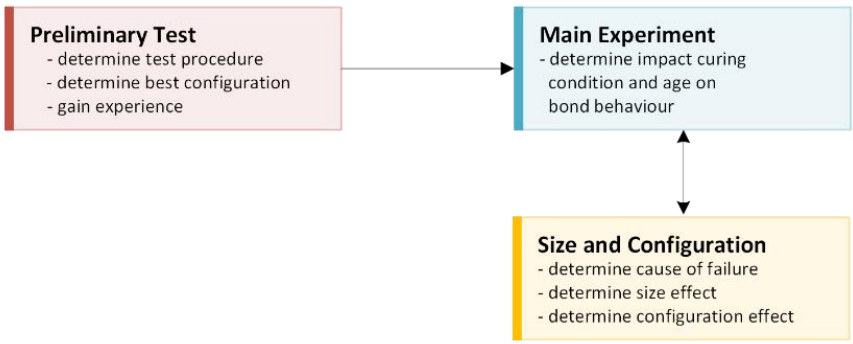

Figure 4-1: Experimental program sequence flowchart

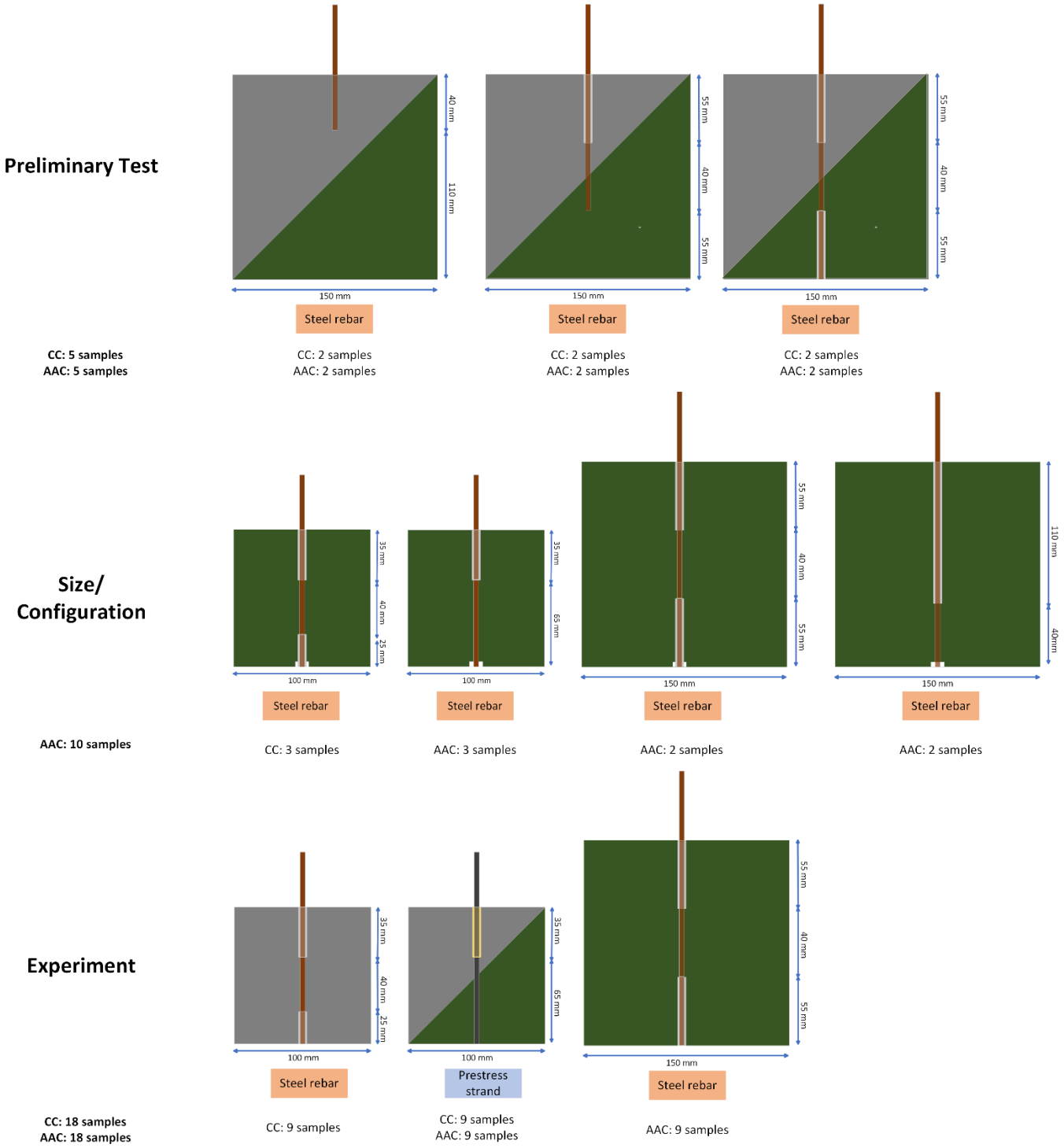

Figure 4-2: Outline experimental program details

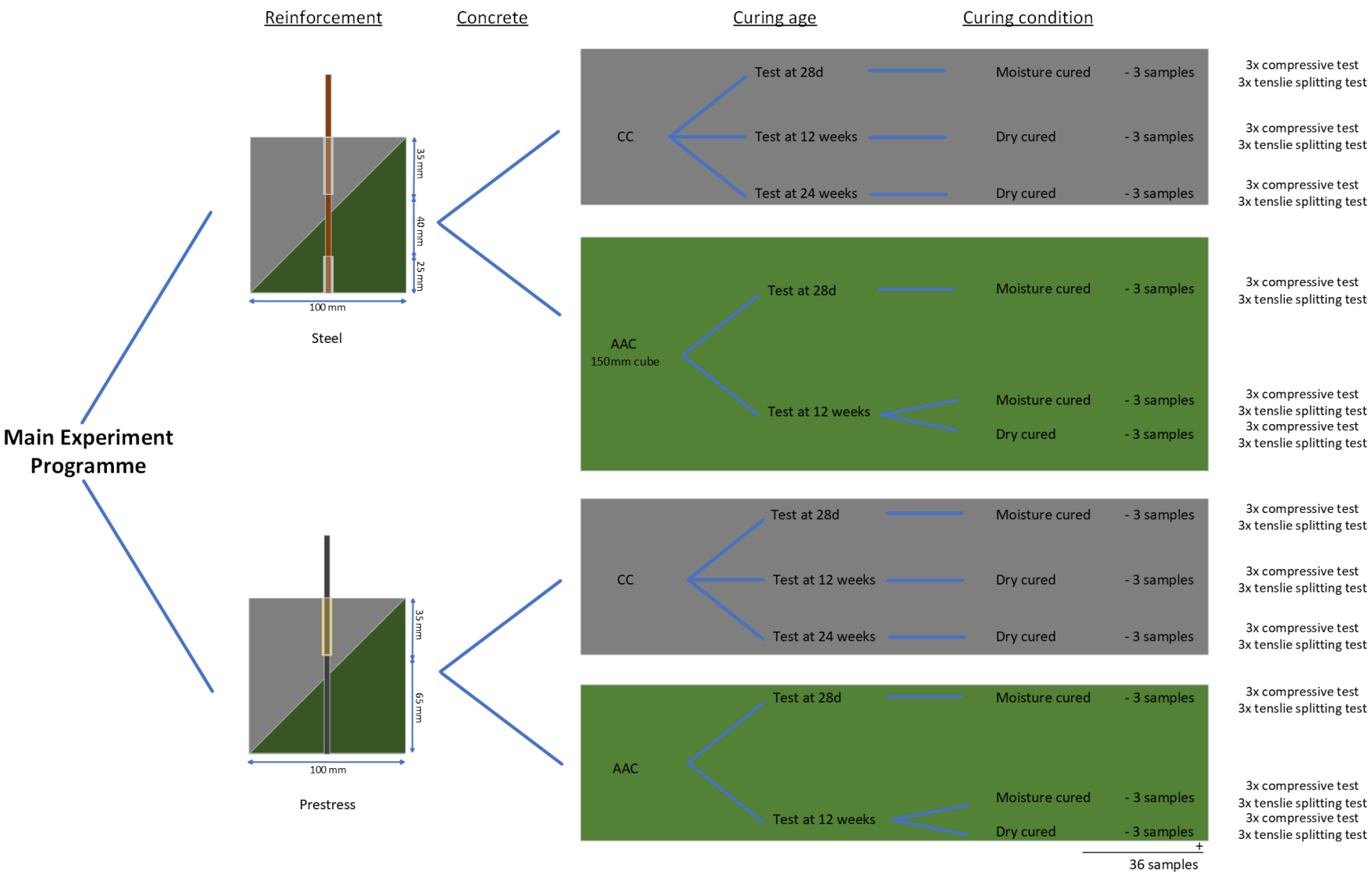

Figure 4-3: Main Experimental Programme outline

4.2 Material, casting and curing procedures

4.2.1 Material and Mixture design

A self-compacting alkaline activated concrete (AASC) mixture designed at TU Delft (Zhang et al., 2022) is used in this study, with a concrete strength class C45/55.. The reference series is cast with CC designed to have similar concrete strength class with AAC.

The Ground Granulated Blast Furnace Slag (GGBFS) used in this study is supplied by Ecocem Benelux. The chemical composition is presented in Table 4-1.

Table 4-1: Blast furnace slag composition (Superfine Technisch datasheet - CO2-arme, hoogwaardige GGBS voor veeleisende betontoepassingen)

SiO_2	Al_2O_3	CaO	MgO	TiO_2	SO_3	Cl-	S_2	$Na_2O_{eqv.}$
35.7	11.6	41	8.7	0.6	0.3	0.01	0.85	0.5

The alkaline activator consists of a mixture of waterglass and sodium hydroxide. The waterglass used in batches 1-8 was supplied by PQ. For the remaining batches 8-12 Brenntag waterglass was used. The difference in chemical concentration was adjusted accordingly. Table 4-2 reports the chemical composition of these materials.

Table 4-2: Alkaline activator composition

	Waterglass		**NaOH**
	PQ (48 wt%)	Brenntag (35 wt%)	Brenntag (50.0 wt%)
SiO_2	14.9 -15.6 %	26.3 - 27.5 %	0 %
Na_2O	7.6 – 8 %	7.8 – 8.2 %	39.36 %
Mol ratio	1.95 -2.05	3.3 – 3.5	

4.2.2 Casting and Curing procedure

Prior to casting, the rebar holders and the rebars are prepared in advance, typically a week before casting. These preparations are detailed in Section 4.3 Specimen preparation. This process concludes with the rebars configured to the proper embedment length, and for some AAC samples, Distributed Fibre Optic Sensors (DFOS) are installed.

A casting week follows a similar structure each time. Preparation of the specimens is performed one day prior to the casting session. The moulds' inside are lubricated. If CC is being cast, oil is used; if AAC is being cast, Vaseline is used. The alkali-activator is prepared 20 hours in advance and stored in laboratory-controlled room conditions (20°C and 55% RH). The ingredients are weighed and stored in plastic buckets, see Figure 4-5 and Figure 4-5a.

The CC and AASC casting both follow similar procedures. All the aggregates (sand and gravel) are first mixed for about 3 minutes. Next, the cement (in case of CC) or GGBFS (in case of AASC) are added to the mixer and mixed for 1 minute. At this point, the liquids are added in a gradual manner. For CC, water is added, and the mixing continues for an additional 4 minutes. In the case of AASC, the alkaline activator solution is added. After 1-2 min of mixing the retarder is added. The mixing is continued until a homogenous concrete mix is obtained, see Figure 4-5c.

When the mixing is completed, the concrete is poured in a wheelbarrow. From there the concrete is scooped into the moulds. The moulds for CC samples are first filled halfway and vibrated for about 20 seconds. Then the remaining half is filled and vibrated again. For AASC specimens no vibration is needed as this concrete is self-compacting. Finally, after casting all specimens are covered with plastic sheets to prevent moisture loss, and are left to harden, see Figure 4-5e.

After one to two days, the specimens were demoulded (see Figure 4-5f). The CC specimens were left for hardening for 1 day. The AASC specimens were initially demoulded after 1 day as well (PT_AAC batch #2 and ME_AAC batch #5). However, when demoulding batch #5 after 1 day of hardening the concrete was still soft. This was not the case for PT_AAC specimens. This is explained by the temperature difference between these batches. Batch #2 was cast in August where the temperature was much higher (max 23°C) than in March (max 9°C) when batch #5 was cast. Therefore, the proceeding AASC batches were cured for 2 days in constant laboratory conditions with the temperature of 20°C. When demoulding has been completed and all specimens have been labelled, Figure 4-5g, the specimens are weighed. This allows tracking the moisture loss of the specimens during curing.

Finally, all samples are transferred to the fog room (relative humidity (RH) 99% and temperature 22°C) of Stevin Lab - TU Delft for moisture curing till 28 days (Figure 4-5j). Depending on the testing plan, some specimens were exposed to drying under a constant laboratory condition (20°C and 55% RH), whereas others remained in the fog room until the day of testing. An overview of the curing procedure can be seen in Figure 4-4: Curing procedure.

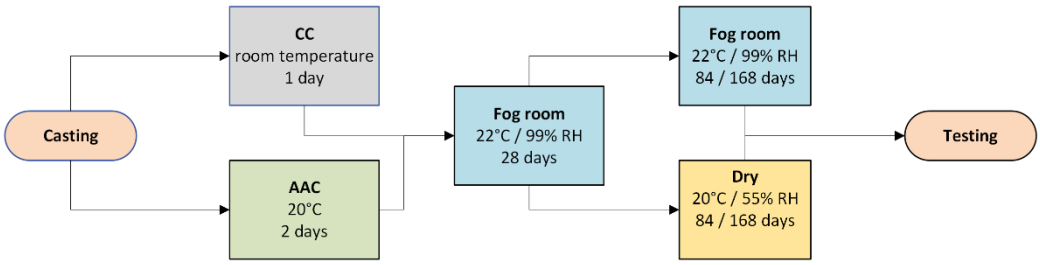

Figure 4-4: Curing procedure

Figure 4-5: Casting procedure

Figure 4-5 a: CC casting weighed materials; sand, aggregate and GGBFS

Figure 4-5 b: Mixer 40L

Figure 4-5 c: AASC mixing

Figure 4-5 d: Prepared specimens just before casting

Figure 4-5 e: Plastic covered specimens after casting

Figure 4-5 f: Demoulding AASC concrete 100mm sized cubes

Figure 4-5 g: Labelling concrete specimens after demoulding (ME #3 CC)

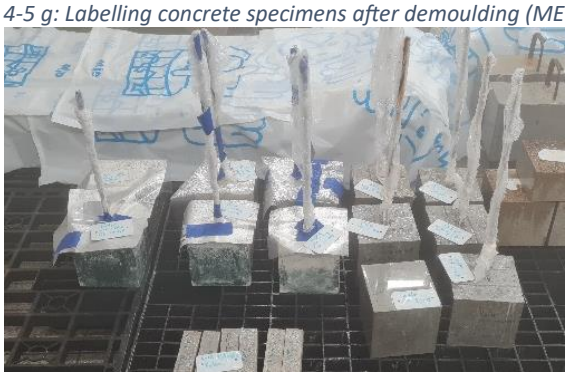

Figure 4-5 h: Moisture cured specimens (fog room). AASC specimens are covered, CC fully exposed

Table 4-3: Casting schedule: Preliminary Test, Size and Configuration test and Main Experiment

Series	Casting Date	Specimen ID	Curing condition	Exposure Date	Curing age	Testing Date	Notes
Preliminary Test #1 CC	26/Jul/23	PT-CC150-S-40 PT-CC150-S-5540 PT-CC150-S-554055	Moisture			Dec-Jan/23	
Preliminary Test #2 AAC	15/Aug/23	PT-AAC150-S-40 PT-AAC150-S-5540 PT-AAC150-S-554055	Moisture			Dec/Jan-23	
Main Experiment #3 CC	27/Feb/24	ME-CC100-S/P-6m-D	Dry	26/Mar/24	168 days	05/Nov/24	
Main Experiment #4 CC	05/Mar/24	ME-CC100-S/P-28d-M ME-CC100-S/P-3m-D	Moisture + Dry	02/Apr/24	28 days + 84 days	02/Apr/24 + 28/May/24	
Main Experiment #5 AAC	12/Mar/24	ME-AAC100-S/P-6m-M ME-AAC100-S/P-6m-D	Moisture + Dry		168 days		Bottom wood piece restrained shrinkage, causing splitting failure. 1 day hardening not enough
Main Experiment #6 AAC	19/Mar/24	ME-AAC100-S/P-28d-M	Moisture		28 days	16/Apr/24	Most steel specimens failed during curing
Main Experiment #7 AAC	26/Mar/24	ME-AAC100-S/P-3m-M ME-AAC100-S/P-3m-D	Moisture + Dry	23/Apr/24	84 days	18/Jun/24	Most steel specimens failed during curing
Main Experiment #8 AAC	10/Apr/24	ME-AAC100-S/P-6m-M ME-AAC100-S/P-6m-D	Moisture + Dry	08/May/24	168 days		Most steel specimens failed during curing This batch failed, due to corrosion of the pipe, more over in Section 4.3.3
Size/Configuration #9 AAC	30/Apr/24	SC-AAC100-S-354025 SC-AAC100-S-3565 SC-AAC150-S-554055 SC-AAC100-S-11040	Moisture			18/Jun/24	
Main Experiment #10-12 AAC	14/May/24	ME-AAC150-S-28d-M ME-AAC150-S-3m-M/D ME-AAC150-S-6m-M/D	Moisture	18/Jun/24	28d 3m 6m	11/Jun/24 06/Aug/24	Batch #12 is not part of this study

Table 4-3 reports the casting schedule of all the batches cast for each test series. Each specimen is given a unique identification code. Based on the following aspects.

- Test series: Preliminary Test: **PT**, Size and Configuration: **SC** and Main Experiment: **ME**
- Concrete type and size: Alkali activated concrete: **AAC**, and Conventional Concrete: **CC**. Followed by the concrete size either 100 mm are 150 mm cube.
- Reinforcement type: Steel: **S** and Prestressing strands: **P**.
- Curing Age: time dependant effect at: 28 days: **28d**, 84 days: **3m** and 168 days: **6m**.
- Curing condition: Two curing conditions are considered. Moisture: **M**, Dry: **D**
- Sample number: Each test is performed three time. Hence sample numbers: **1**, **2** and **3**.
- Configuration: In case of size and configuration series the configuration is denoted by the final numbers, which refer to the different embedded segments length (bonded and unbonded).

4.3 Specimen preparation

The setup and preparation of the specimens have been through various iterations. The setup of the specimens consists of two parts: the mould and the rebars. The same moulds are used for casting the pull-out and material test specimens.

4.3.1 Moulds

An addition is made to the moulds of the pull-out specimens to ensure that the rebars remain straight and centred during casting. Through the different series, as denoted in Figure 4-2, two different sizes of moulds have been used: 100 mm and 150 mm. The wooden additions to the mould intended to restrain the rebars have been adjusted accordingly. This addition is referred to as the 'rebar holder'.

Fist iteration: *Batch #1: Preliminary Test-CC*
The first iteration was used to cast the Preliminary test CC specimens. This iteration consisted of a square wooden frame, with a wooden piece across the middle of the frame. The centre piece has a hole where the rebar protrudes from at centre of the mould. The rebar is held in place with a clamp on the top side. This whole frame was placed on top of the mould (150 mm size). On either side of the centre wood piece, the concrete could be poured into the mould, see Figure 4-6a.

This first iteration was not optimal in various ways. First and most importantly, the setup could not ensure that the rebar remained straight. The centre wood piece was too thin. Therefore, in some samples a double frame was used, see Figure 4-6b. Furthermore, the frame itself was not rigid enough, as some fell apart during casting when the moulds were placed on the vibrating table.

Figure 4-6: Rebar holder v1

Figure 4-6a: top view

Figure 4-6b: double frame

Figure 4-6c: side view

<u>Second iteration</u>: *Batch #2: Preliminary Test-AAC*
The top addition was adjusted for the subsequent casting session for the preliminary test AASC specimens. In this iteration, the wooden frame was discarded. Instead, the rebar was held in place with a thicker centre piece. This centre piece features a fixed steel L-hook on one side (right) and a sliding L-hook on the opposing end (left side), see Figure 4-7a and Figure 4-7b. This design allows the centre wood piece to be secured tightly to the mould. As a result, the protruding rebar of the pull-out specimen remained much straighter, as can be seen in Figure 4-7c. In this iteration, the rebar is still prone to displacement as it is not securely fixed at the bottom.

Figure 4-7: Rebar holder v2

Figure 4-7a: side view

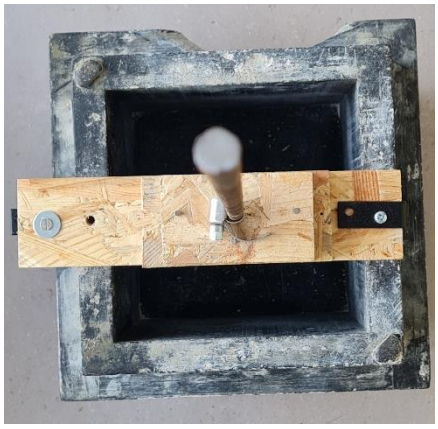
Figure 4-7b: top view

Figure 4-7c: side view after casting

<u>Third iteration</u>: *Batch #3 - 12: Main Experiment and Size/Configuration*
The main experimental program as well as the size/configuration test were cast with both 100 mm and 150 mm size moulds, as shown in Figure 4-8a. The 100 mm moulds are made from steel and differ slightly from the plastic moulds. The steel moulds do not have plain edges, so the L-hooks are secured diagonally to the mould edge, see Figure 4-8b. For the recast of AASC 150 mm moulds, a similar diagonal L-hook was adopted. When the screw is tightened, it creates a compressive horizontal force, which keeps the rebar holder tightly in place.

Figure 4-8: Rebar holder v3

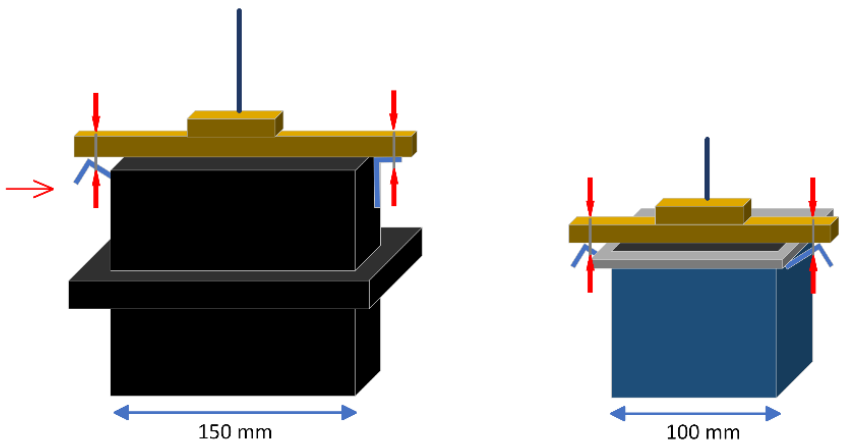

Figure 4-8a: Diagram 150 mm vs 100 mm moulds

Figure 4-8b: 100mm mould

In addition to the rebar holder, a bottom wood piece was added to restrain the rebar end, keeping it straight, see Figure 4-9. This setup did not affect the CC specimens. However, by the following day, the AAC specimens developed longitudinal cracks, see Figure 4-10. Because the samples were properly covered before demoulding, only autogenous shrinkage was at play. AASC exhibits relatively high autogenous shrinkage compared to CC. Unlike CC, which autogenous shrinkage stabilizes after 7 days, AASC experiences prolonged, elevated rates of autogenous shrinkage that continue for several weeks (Z. Li et al., 2020; Zhang et al., 2022). The high autogenous shrinkage in AASC, combined with the restraint provided by the wooden base, likely caused the observed cracking.

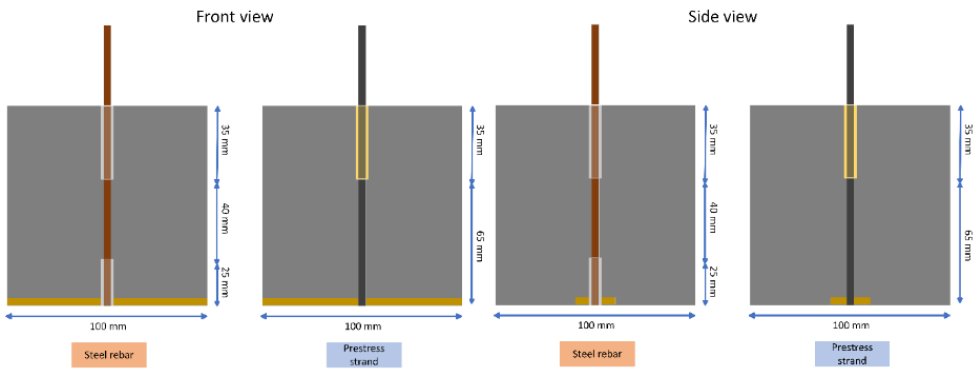

Figure 4-9: Conventional concrete mould setup and rebar configuration, left: side view - right: front view

Figure 4-10: Batch #5: AASC specimens 1 day after casting

For this reason, the bottom wood piece was left out for the AASC specimens. Instead, a silicone layer was used, Figure 4-11. This silicone layer helps keep the rebar in centre and keeps the screw hole for the LVDT platform free, further explanation regarding the LVDT platform in the following segment 4.3.2 Monitoring device installation.

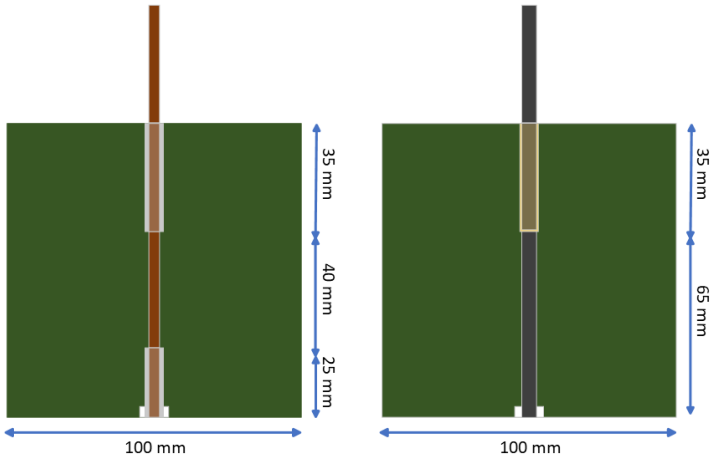

Figure 4-12: Inside of mould

Figure 4-11: Batch #6-12: New AASC setup using silicone instead

4.3.2 Monitoring device installation

Preparation of DFOS

Distributed Fibre Optic Sensors (DFOS) are applied to some of the steel rebar specimens in the series: Main Experimental program and Size/Configuration. The execution of this process is detailed in this segment, with all the steps illustrated in Figure 4-13 on the following page.

1. Preparation of the Rebar

The entire rebar segment to be embedded in the concrete is sanded on the flat side, which is where the DFOS will be glued, Figure 4-13b. The rebar is then cleaned with isopropanol alcohol to remove all rust and dirt, ensuring proper adhesion of the DFOS to the steel later on. Next, the segments (embedded length and pipe segments) are marked on the clean rebar. Finally, a sleeve is glued onto the rebar segment that will remain exposed. This sleeve serves to protect the DFOS that remains unbonded and exposed, as shown in Figure 4-13c.

2. DFOS Setup

DFOS sensors work by reflecting light traveling through the fibre. With the fibre embedded inside the concrete, a final segment, a 'coreless' fibre segment, is added to the end for this purpose. To prepare for this addition, the DFOS protection layer is stripped, Figure 4-13g. The DFOS is then cut with the ShinewayTech OFC-10 cleaver, as illustrated in Figure 4-13h and Figure 4-13i. The cleaver makes a perfect straight cut, necessary for splicing the 'coreless' fibre segment to the DFOS using the ShinewayTech OFS 95S splicer. The same procedure is followed to splice the 'pigtail' to the DFOS. The pigtail connects the DFOS to the signal source. As this part is exposed, it is more fragile. Therefore, a heat shrink-sleeve is added at the spliced connection. For additional sturdiness some tape is wrapped around, Figure 4-13m.

3. Adhering DFOS to rebar

The embedded segment, $5d_b$, is glued with a cyanoacrylate adhesive, see Figure 4-13f. After 24 hours of drying, a protective PU-coating layer is applied to the glued segment. The unbonded regions (pipe covered segments) are glued with Griffon glue.

4. DFOS profile

After the DFOS was adhered to the rebar. A rebar profile is made before embedding the rebar in concrete. With the rebar profile the important locations are denoted in the system beforehand. These locations are: surface of the concrete, start and end embedded segment. This step is crucial for later processing of the data.

These steps ensure the DFOS is properly installed and protected within the concrete specimens, allowing for accurate measurement of the bond strength and slip behaviour over time. More detail about the DFOS measurement specifications and measurement device in Section 4.4 Test Method.

Figure 4-13: Installation DFOS

Figure 4-13 a: Rebar cut to size

Figure 4-13 b: Sanded and cleaned rebar

Figure 4-13 c: Attaching DFOS sleeve

Figure 4-13 d: Isopropyl

Figure 4-13 e: Glue used unbonded regions

Figure 4-13 f: cyanoacrylate adhesive

Figure 4-13 g

Figure 4-13 h: Optical Fibre Clever

Figure 4-13 i: Placing fibre in clever

Figure 4-13 j: Shineway splicer

Figure 4-13 k: Splicer inside

Figure 4-13 l: Shineway splicer

Figure 4-13 m: Spliced fibre (red) to pigtail (yellow)

Figure 4-13 n: Wrapping DFOS unbonded region

Figure 4-13 o: Fully completed DFOS rebar

LVDT platform

A LVDT platform is designed and utilised to measure the slip from the free end of the rebar during the pull-out test series. In the case of steel reinforcement, this platform is screwed into the steel, see Figure 4-14a and b. However, drilling a hole in prestressing steel is not feasible due to its hardened nature. For these specimens, the LVDT platform is soldered on after casting, see Figure 4-14c and d.

Figure 4-14: LVDT platform

Figure 6-14 a

Figure 6-14 b

Figure 6-14 c

Figure 6-14 d

4.3.3 Configuration

This research investigates the bond behaviour of Ø 8 mm ribbed steel rebar and Ø 12.9 mm plain 7-wire FeP1860 prestressing strand. The embedment length is a multiple of the rebar diameter, $5d_b$. This follows from the literature Section 4.1 were $5d_b$ was proved to be optimal (Ma et al., 2023; Paswan et al., 2020; Peng et al., 2022). Moreover, an embedded length of $5d_b$ is the specified bond length for direct pull-out test in EN10080:2005. Therefore, the embedment lengths are: $5d_b = 40\ mm$ for steel rebars and $5d_b = 64.5\ mm$ for the prestressing strands. The embedment length is maintained inside the concrete by covering the remaining segments with pipes. The execution of the rebar setup has also undergone different iterations.

Preliminary test

The purpose of this series was to check the setup and test the applicability of different embedment methods in the pull-out tests. As can be seen from Figure 4-15, the preliminary tests consist of three different rebar embedment configurations. For this test series only Ø 8 mm ribbed bars were used. To keep the desired embedment length an aluminium pipe with an inner Ø 10 mm and Ø 12 mm outer diameter was used. As the pipe is larger than the rebar, the rebar was wrapped in tape to fit inside the pipe. In this way the pipe is held in place by friction, see Figure 4-23a and b. Figure 4-15 presents the test setup alongside the three different configurations.

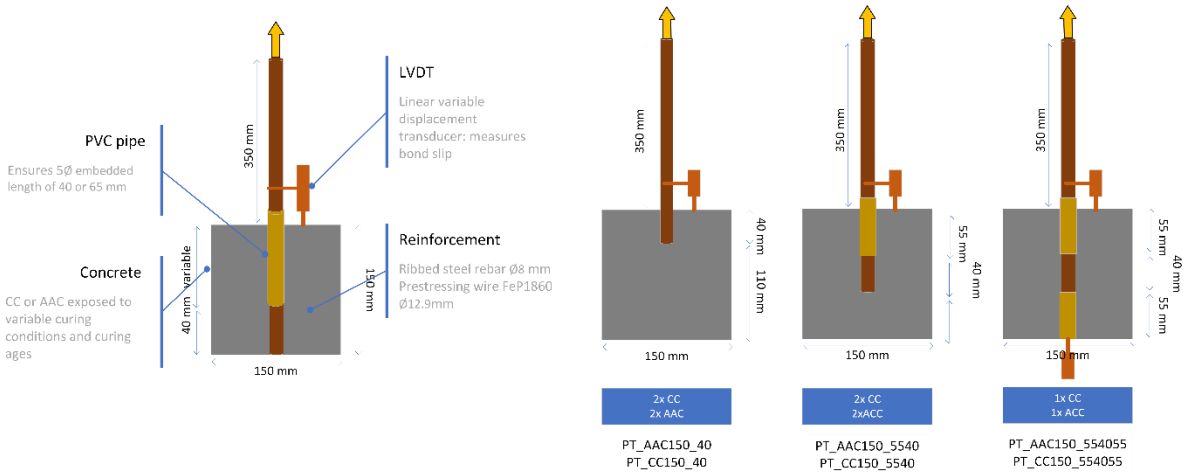

Figure 4-15: Preliminary test setup: 3 Configurations

Main Experiment

Initially, the same procedure to set up the rebars was followed for the main experiment. The only difference this time was that smaller 100 mm cubes were used instead of the 150 mm cubes used in the preliminary test series. This decision was based on the understanding that smaller cubes may experience a larger drying effect due to their higher surface area-to-volume ratio. With a greater exposed area, the rate of moisture loss is increased, consequently leading to more significant drying shrinkage (Nmai et al., 2018). Therefore, the effect drying effect on the bond behaviour might be more noticeable in a shorter time frame.

In addition to steel rebar specimens, prestressed specimens were also cast for this series. To ensure proper embedment length, part of the reinforcement is covered with a pipe. A preference for pipes that closely match the rebar size was prioritized over material type. Thus, taking into account the availability. A PVC pipe with an inner diameter of 13 mm and an outer diameter of 15 mm was utilised for the larger prestressing strands (Ø12.9 mm). The steel reinforced specimens were covered using a smaller aluminium pipe with an inner diameter of 10 mm and an outer diameter of 12 mm, which was also employed in the Preliminary Tests. Refer to Figure 4-16, where the grey pipe represents aluminium and the yellow pipe represents PVC.

The steel and prestressed strands also differed in their respective configuration. Due to their respective differences in size, the embedment length $5d_b$ is larger for the prestressing strands compared to the steel specimens. Therefore, the configuration is different, as shown in Figure 4-16.

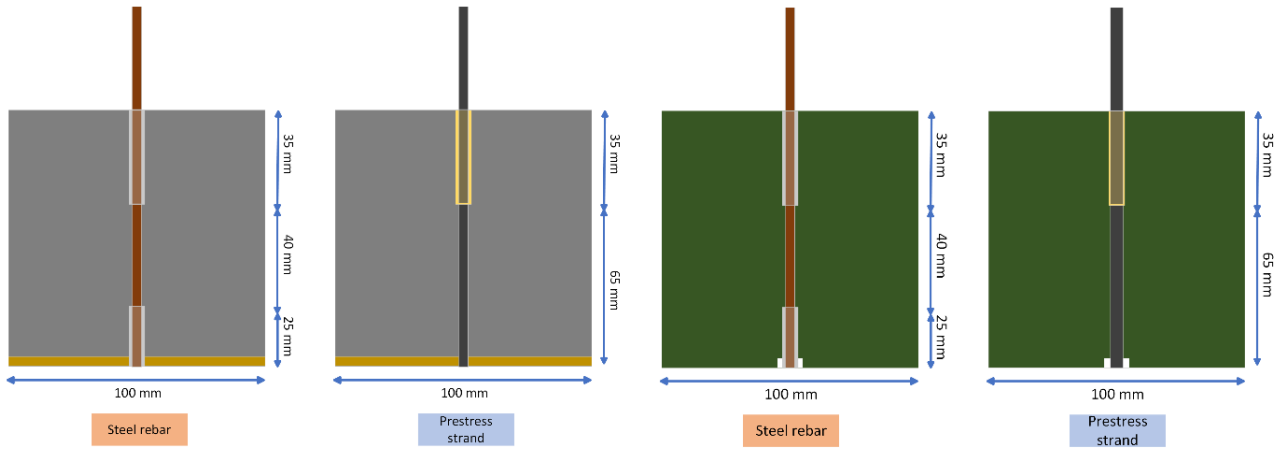

Figure 4-16: Main Experiment configuration: CC (grey) and AAC (green), steel and prestressing strand reinforced concrete

Size and Configuration

After casting the specimens of the 'Main experiment' series, batch #6-8. As can be seen from Figure 4-17, It turned out that most of the steel specimens split during curing. On the contrary all of the prestressing specimens were fine. Therefore, the cause for one segment of the specimens (steel) to fail instead of the other, lies in their differences. As described in the previous segment, the differences between the steel and prestressed specimens are the configuration. Another difference is the pipe material used for the covered segments: aluminium pipe was used for the steel specimens, whereas PVC pipe was used for the prestressed specimens.

To identify the cause of splitting crack development of the steel specimens, a new series "Size and Configuration" was cast. Since the prestressed specimens did not fail, the same size PVC pipe was used for all specimens in this new series. The configuration differences were now tested while keeping the pipe material as a constant. This approach allowed for the determination of whether the steel specimens failed due to the differences in configuration or the pipe material.

Interestingly, same aluminium pipe was used for the Preliminary Test. Contrary, to the Main experiment. The Preliminary Test specimens did not fail. Presumably due to size effect, the shrinkage effect is less pronounced for the larger 150 mm cube sizes. As a result, the decision was made to recast these failed specimens using larger specimens that measure 150 mm in size. Since the remaining specimens measure 100 mm, an additional set of 150 mm cubes was produced in the Size and Configuration series in order to assess the extent to which the size effect influences bond strength.

Figure 4-17: Failed AAC batches

Figure 4-17 a: Batch #8: Bottom view

Figure 4-17 b: Batch #7: Bottom view

Figure 4-17 c: Batch #6: Bottom view

Figure 4-17 d: Batch #8: Top view

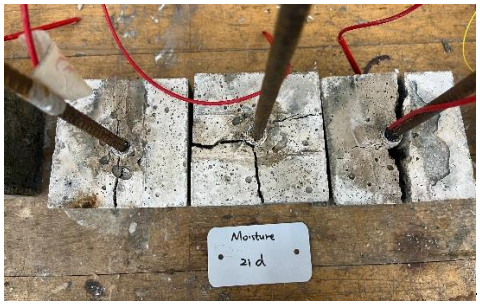

Figure 4-17 e: Batch #7: Top view

Figure 4-17 f: Batch #8: Top view

4.3.4 Size and Configuration Results

Following the failed Main Experiment AAC specimens. An additional batch referred to as “Size and Configuration” was cast. This test aimed to determine the cause of failure. By comparing two different configurations and two different specimen sizes, see Figure 4-2. The main adjustment made for this series was using PVC pipe instead of aluminium pipe for the unbonded rebar segments. This adjustment allowed for an assessment of whether the cause of failure was due to the pipe material or the configuration of the specimens. Additionally, the size effect on the bond behaviour is investigated.

Figure 4-18: Corroded aluminium pipe

Pipe type

Unlike the failed specimens, none in this series failed. The main difference between the failed and new specimens in the "Size and Configuration" series is that PVC pipe was used to cover the unbonded steel segments instead of aluminium. The material used to cover the unbonded region remained consistent throughout this series (PVC), regardless of configuration or size. Therefore, it can be concluded that the splitting failure was due to the aluminium pipe used in the failed specimens. The embedded aluminium pipe started corroding inside the AASC specimens, leading to material expansion within the concrete. This corrosion induced tensile stresses within the concrete. Similarly, the high autogenous shrinkage of AASC also contributes to considerable tensile stresses (Li et al., 2021). This, coupled effect of corrosion and high autogenous shrinkage of AASC, ultimately caused the specimens to break open, as the induced stresses exceeded the concrete’s tensile strength. Figure 4-18 shows a corroded aluminium pipe taken from one of the previous failed batches.

Figure 4-19, presents the first week of DFOS measurements, which monitor the strain in the steel. This strain reflects the chemical adhesion bond between the steel and the concrete. During the curing process, the autogenous shrinkage strain of the concrete is transmitted to the steel due to this bonding mechanism. The objective was to determine conclusively whether the corrosion of the aluminium pipe affected the integrity of the concrete. It is anticipated that microcracks resulting from the induced stresses will be reflected in the concrete's bond strength, as studies have shown that corrosion can lead to crack propagation and a subsequent reduction in bond performance (Almusallam et al., 1996).

DFOS strain measurements for the new “Size and Configuration” samples are presented in the top row of Figure 4-19 (a-d), while measurements for the failed “Main Experiment” series samples are shown in the bottom row (Figure 4-19, e-g). As previously discussed, the primary difference between these two sets is the material used to cover the unbonded segment of the pipe. A closer examination of the Size and Configuration DFOS measurements reveals that, at the 7-day mark, distinct localized peaks appear, which are absent in the initial 5-hour measurement. These peaks could indicate localized microcracks; however, similar peaks are also visible in the unbonded region as well as for the Main Experiment (Figure 4-19e-g). Consequently, it cannot be definitively concluded that these peaks represent microcracks, as they may stem from other factors. As a result, the effect of corrosion on the concrete could not be conclusively verified through DFOS measurements alone.

Figure 4-19: DFOS measurement pipe material comparison aluminium compared to PVC, first week strain measurements

Size and Configuration

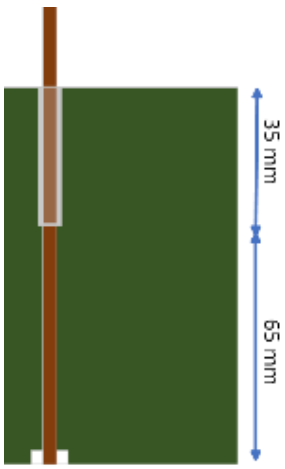

Figure 4-19a: Configuration of steel reinforced 100 mm AASC with PVC covering

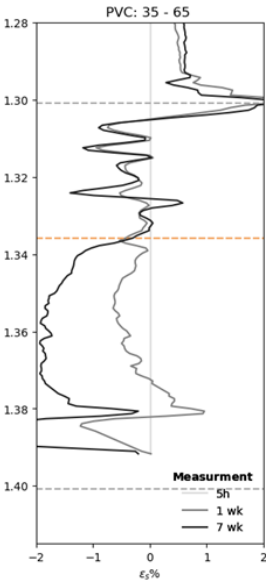

Figure 4-19b: DFOS measurement of steel reinforced 100 mm AASC with PVC covering

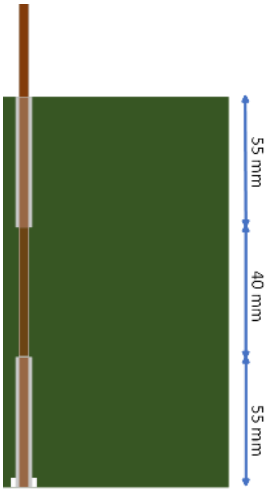

Figure 4-19c: Configuration of prestressed, reinforced 150 mm AASC with PVC covering

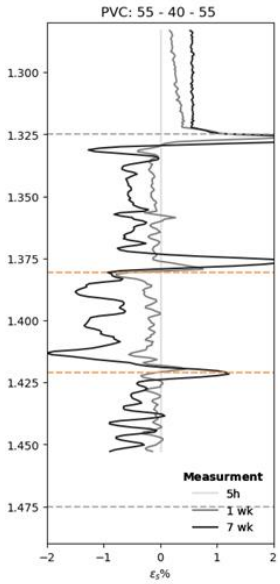

Figure 4-19d: DFOS measurement of steel, reinforced 150 mm AASC with PVC covering

Main Experiment

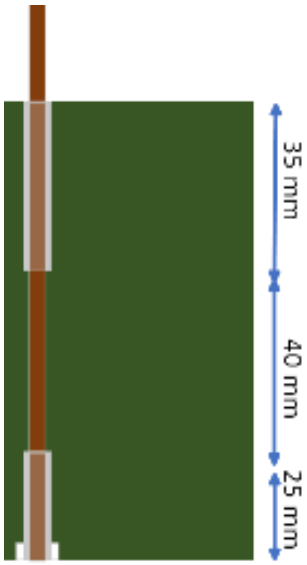

Figure 4-19e: Configuration measurement of steel reinforced 100 mm AASC with aluminium covering

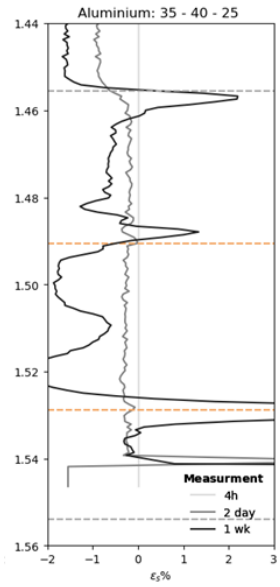

Figure 4-19f: DFOS measurement of steel reinforced 100 mm AASC with aluminium covering

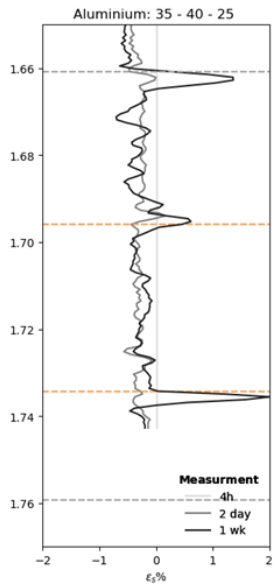

Figure 4-19g: DFOS measurement of steel reinforced 100 mm AASC with aluminium covering

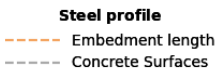

Size effect

The Main Experiment AASC steel specimens (100 mm size), in which aluminium pipe was used to cover the unbonded steel segments, failed due to corrosion of the pipe. To address this issue, new AASC steel specimens were cast in larger 150 mm cubes. Given the size difference between the initial Main Experiment specimens and the replacement, a small test was conducted to assess whether the size difference significantly impacts bond behaviour. This involved samples from the “Size and Configuration” batch, where both 100 mm and 150 mm samples shared a comparable configuration: a 40 mm bonded segment centred on the steel profile, with the remaining steel sections covered. Additionally, PVC pipe was used to cover the unbonded sections in both cases to ensure consistency in testing.

The findings are displayed Figure 4-20. The average pull-out failure bond strengths for similar configurations of different sized specimens were found to be 20.30 MPa for the 150 mm cubes and 23.75 MPa for the 100mm cubes. Despite this difference, the bond strength values fall within a similar range, suggesting that the effect of confinement between the different specimen sizes does not significantly alter the bond behaviour. When considering the standard deviations, 1.81 MPa for the 150 mm cubes and 2.83 MPa for the 100 mm cubes. The ranges largely overlap, indicating that the variations in bond strength could be attributed to natural scatter rather than irregularities in the data. This test aimed to provide an indication of whether size has a major impact on bond behaviour. Given the small sample size and the relatively minor difference in maximum bond strength, it cannot be concluded that size has a major impact on bond behaviour. This similarity supports the assumption that confinement was sufficient across both sizes, and that any observed differences are within expected statistical variability.

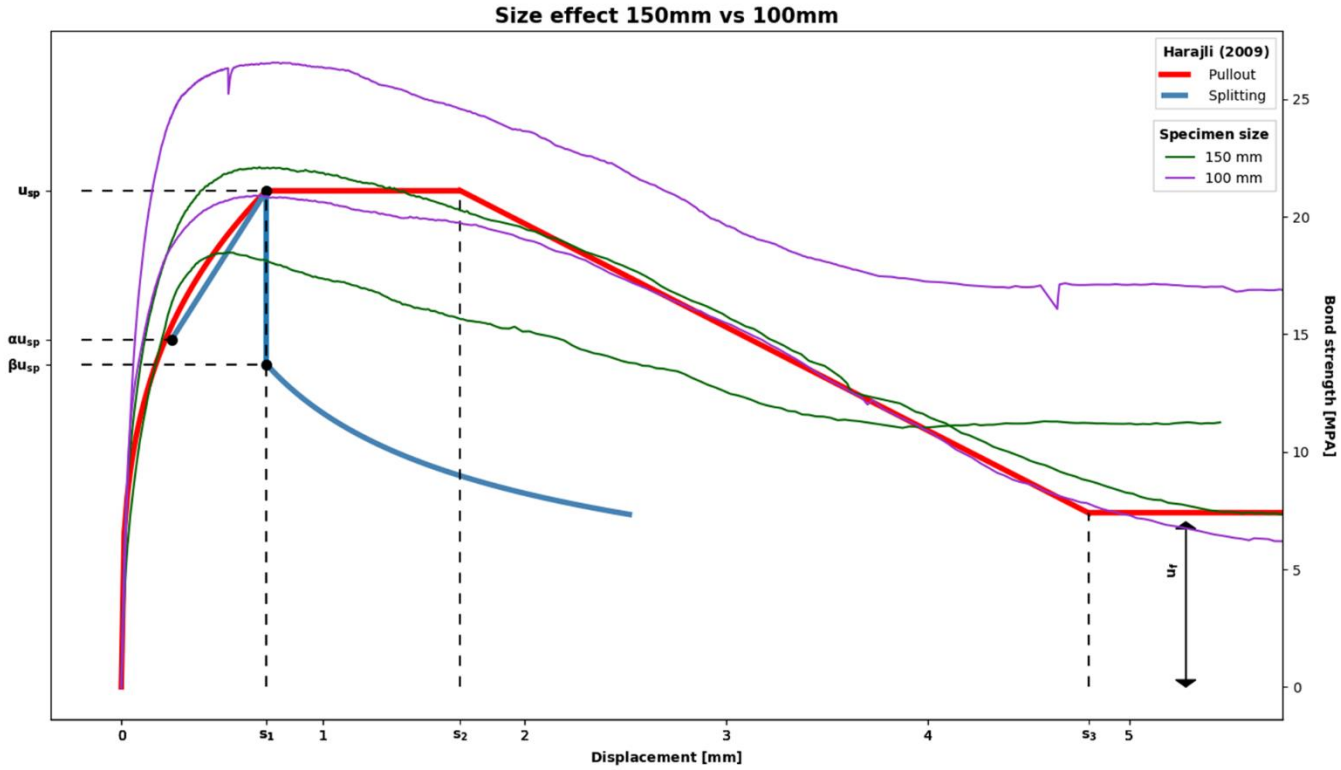

Figure 4-20: Size effect 150mm vs 100mm specimens of AASC mixture

Another small test was conducted to compare the configuration differences in same size 150 mm concrete specimens, as shown in Figure 4-21. Specifically, the test examined the influence of the top unbonded region by comparing specimens with a 55 mm top unbonded region (green) to those with a 110 mm top unbonded region (purple). Although only two samples were tested for each configuration, the results suggest that a larger top unbonded region (110 mm) may provide greater bond strength. The average maximum bond strength was 20.30 MPa for the 55 mm unbonded region compared to 25.96 MPa for the 110 mm unbonded region. This difference in bond strength can be explained by the larger concrete mass above the embedded region, which enhance the concrete's ability to withstand tensile stresses caused by the rebar, resulting to a stronger bond.

In the previous test "Size effect" the difference in the top unbonded region was smaller 55 mm compared to 35 mm, making the concrete mass effect was less pronounced. The main experiment was still performed with the 55-40-55 configuration, as it closely resembles the smaller 35-40-25 configuration of the remaining 100 mm cube size specimens. Additionally, the slightly larger top unbonded region of 55 mm compared to 35 mm did not result in clear difference in bond behaviour.

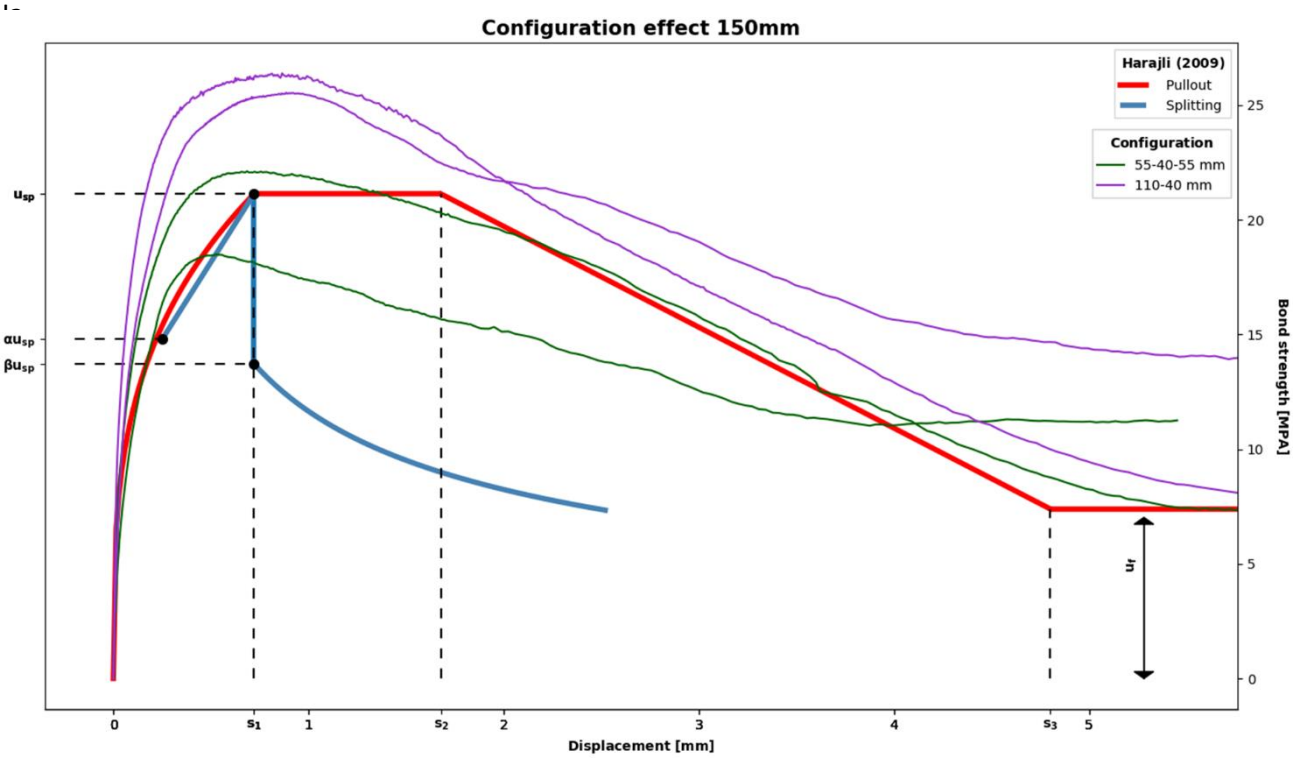

Figure 4-21: Configuration effect 55(covered)-40(embedded)-55(covered) vs 110(covered)-40(embedded)

Final pull-out specimens design

Following the failure of AASC specimens in the Main Experiment, a Size and Configuration test was conducted to determine the cause of failure. The presence of the aluminium pipe, which was employed to encase the unbonded areas in the steel reinforced specimens, resulted in the cracking of the AAC specimens during the curing process. The corrosion of the aluminium pipe, along with the significant shrinking of AAC, was the cause of the failure. The smaller size of these specimens exacerbated the shrinkage effect. This was proven by the larger sized preliminary test (150 mm), which also used aluminium pipes but showed no cracks. As a result, it was decided to recast the failed specimens in larger 150 mm cubes, using PVC pipe for the unbonded segment instead. To account for these changes, the effects of size and configuration differences were compared. Results show that both sizes provide sufficient concrete mass to withstand tensile stresses and ensure pull-out failure. The effect of the top unbonded concrete layer was also investigated, with results indicating that a larger unbonded segment results in greater bond strength. However, the difference in the top unbonded concrete layer between the two specimen sizes is small and does not significantly affect bond behaviour. Essentially, the new specimens created for the Main Experiment will have modest variations compared to the other 100 mm specimens.

Consequently, the final design for the new replacement AASC samples will use larger 150 mm cubes, configured similarly to the remaining 100 mm specimens in the Main Experiment. The embedded length remains the same at 40 mm, however, the unbonded sections have been modified to accommodate the larger size. Thus, the new configuration consists of a 55 mm pipe covered unbonded zone on both the top and bottom. Compared to the previous 35mm and 25mm pipe covered segments on the top and bottom for the 100 mm cubes. The final design for the replacement specimens is depicted in Figure 4-22b.

Figure 4-22: Configuration diagram for Main Experiment: CC 100 mm reference and AASC 150 mm replacement samples

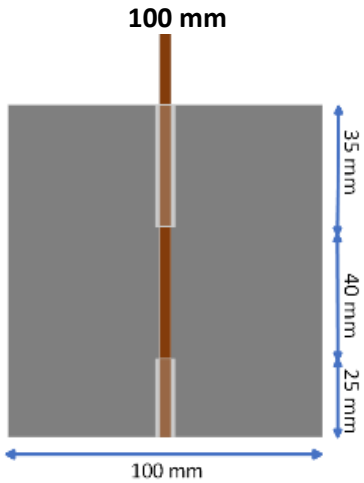

Figure 4-22a: Main Experiment Aluminium covered CC 100 mm

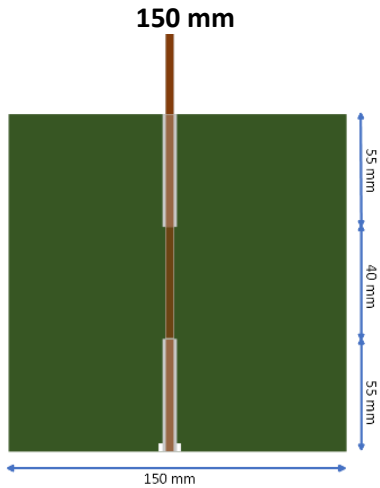

Figure 4-22b: Main Experiment PVC covered AASC 150 mm

The change in pipe from aluminium to PVC requires a slight change in the setup procedure. When using a larger 13 mm PVC pipe, wrapping the rebar's bottom covered segment in tape is no longer a viable option to hold the pipe in place. If the rebar is pulled out, this thicker part (tape wrapped) will be restrained against the concrete and might influence the results. Therefore, the bottom pipe segment rests on the bottom of the mould, and tape prevents concrete from seeping inside, as shown in Figure 4-23d. This way, the lower covered rebar segment remains plain. For the top covered segment, the pipe hole is sealed by wrapping tape around the rebar. The pipe itself is held in place by friction against the rebar, as shown in Figure 4-23a-c.

Figure 4-23: Adjusted rebar setup

Figure 4-23 a: Tape wrap for top pipe

Figure 4-23 b: Top pipe

Figure 4-23 c: Top pipe: securing in place with tape

Figure 4-23 d: Bottom pipe

Figure 4-23 e: Bottom pipe: bottom view

Figure 4-23 f: Fully completed rebar

4.4 Test Method

4.4.1 Test Setup

The pull-out tests are conducted on concrete cubes to measure the bond strength and slip behaviour. The procedure involves embedding reinforcement in concrete cubes and applying a tensile load until the reinforcement is pulled out. The key measurements taken during these tests include:

- Bond Strength: The maximum stress the bond can withstand before failure.
- Slip Behaviour: The relative displacement between the concrete and reinforcement as the load is applied.

The pull-out test setup and procedure were determined during the preliminary test series. Based on the knowledge gained from these tests, the setup and procedure were adjusted. Moreover, regarding the procedure in the upcoming section 4.4.2. The setup consists of a "cage" where the specimens are placed, which serves to restrain them during the pull-out test. The cage is fixed to an immovable lower frame by four rods on each corner. Initially, the cage only consisted of a top plate while the specimens rested on the lower frame. However, this setup did not allow for measuring of the rebar slip on the bottom of the concrete. This setup was quickly changed so that the slip of the steel could also be measured at the bottom of the specimens. To level the top plate, a felt layer is placed between the top plate and the concrete specimen.

The rebar is attached to the hydraulic jack using thick steel clamps, which are pre-tensioned by hand. The jack-clamp connection is free to rotate. Figure 4-24 presents the complete pull-out setup. Direct pull-out test is conducted with the 100 kN “Blauw Cylinder” hydraulic jack at Stevin Laboratory – TU Delft. A displacement-controlled procedure with a variable loading rate is adopted. For steel reinforced specimens the loading rate is 0.01mm/sec up till 2mm slip, at this point the maximum bond strength (u_m) has already been reached. The loading rate is then increased to 0.03mm/sec. The test is halted when the bond strength reaches a plateau u_f (constant residual stress). For prestressing strand reinforced specimens, a starting load-rate of 0.03mm/sec is adopted. Once a clear peak is reached, usually about 7-8mm slip, the load rate can be increased to 0.05mm/sec for the remaining descending curve of the pull-out test.

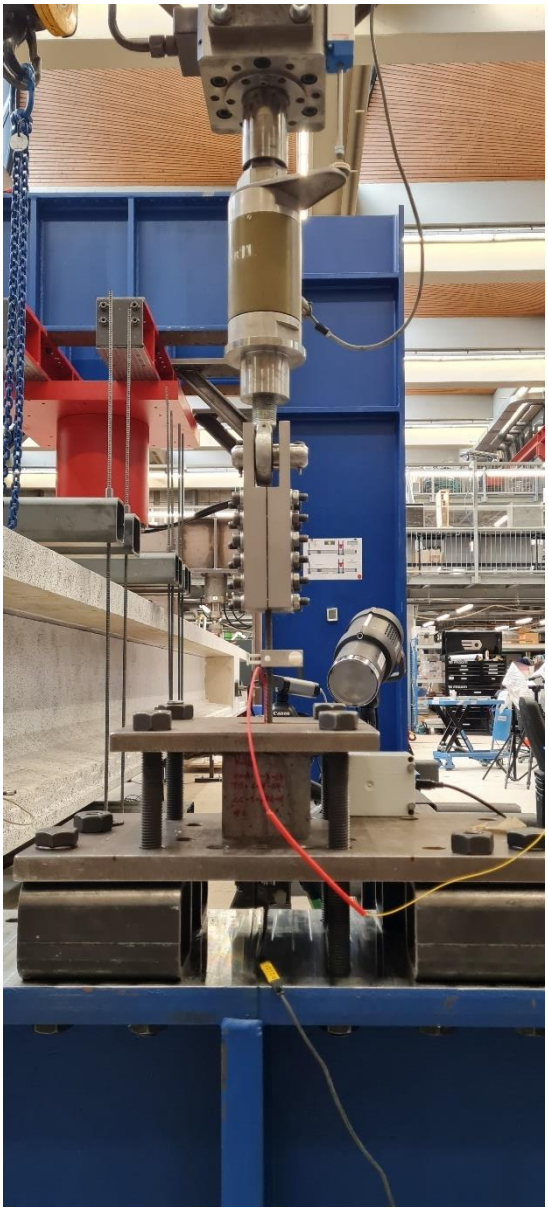

Figure 4-24: Pull-out test setup

Figure 4-25: DIC camera setup

4.4.2 Preliminary Test Procedure and Results

Procedure

A major point of discussion was the need for confinement of the concrete specimen. Compressing the concrete is believed to reduce the likelihood of splitting failure; the additional confinement would, therefore, guarantee pull-out failure. In accordance with this concept, the top plate was subjected to prestressing. The level of prestressing was varied during the experiment, ranging from substantial prestressing (resulting in significant compression of the specimens) to intermediate prestressing (applying some compression but not excessive) to hand-tightened (no compression applied).

In the end, it was concluded that an intermediate amount of prestressing of the top plate was adequate. As will become clear in the proceeding segments, the prestressing of the top plate had a major impact on the results.

Results

In this segment, the preliminary test results are presented. To comprehend these results, it is imperative to provide the necessary context on how the test procedure was followed. As it turns out the test procedure, mainly the amount of prestressing applied on the top plate had significant impact on the results.

Table 4-4 presents the compressive test results for the preliminary tests. The preliminary test was not intended to derive any conclusions on the pull-out behaviour in respect to the material properties. Therefore, only one compressive test was performed for each concrete type.

Table 4-4: Preliminary Test results

Preliminary Test			
Specimens	f_{cd} [MPA]	Days	Batch
CC150	71.40	140 (moisture)	1
AAC150	67.17	112 (moisture)	2

The following Figure 4-26 present the preliminary test results for all three configurations. For clarity, diagrams of the specimen's configuration are incorporated in the figure. The figure also compares the Harajli bond model, for both pull-out and splitting failure against the obtained results. This theoretical model predicts bond behaviour based on the compressive strength, more over in Chapter 6. Failure mode is indicated by line type: a solid line represents pull-out failure, while a dotted line represents splitting failure. Displacement during the test is recorded either from the top or bottom, depending on the configuration. For Configurations 1 and 2, displacement of the rebar is recorded from the top, while for Configuration 3, displacement is recorded from the bottom. Each test is labelled as PT#, which will be referenced in the following paragraph. The discussion will focus on the effects of confinement in each test.

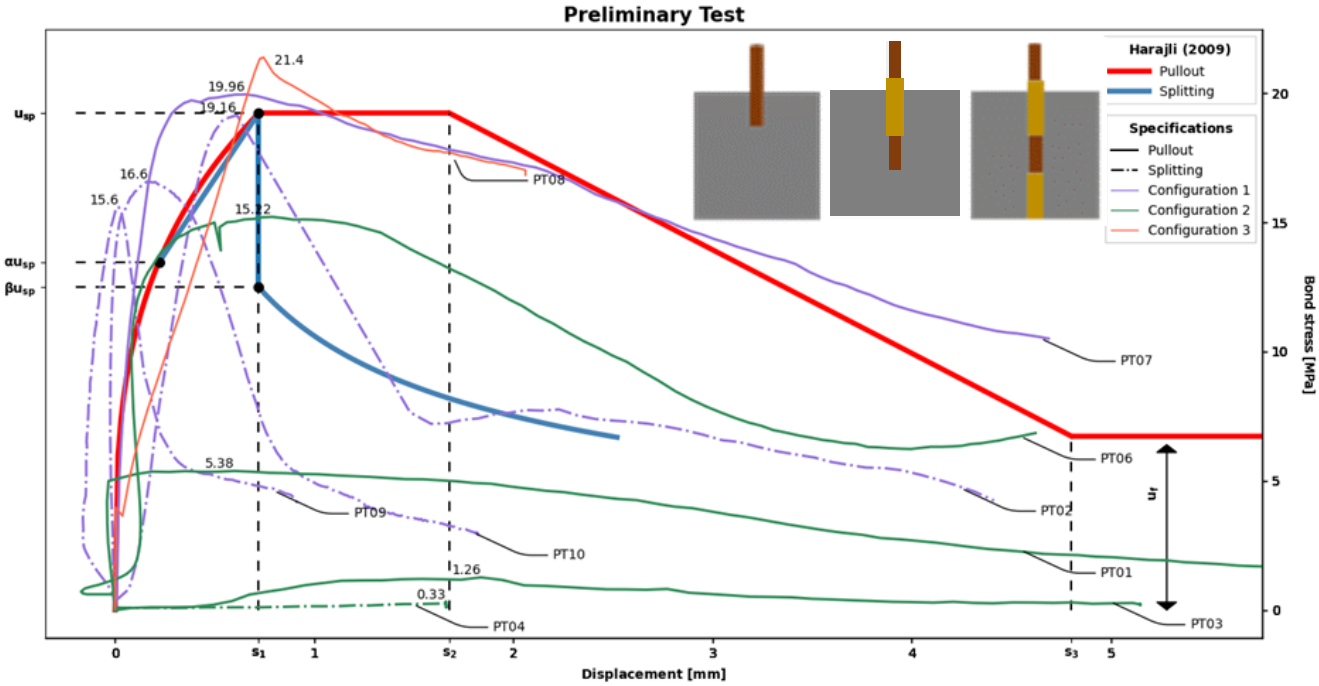

Figure 4-26: Preliminary test result configuration 1

Influence of confinement

A major point of discussion was the need for confinement of the concrete specimen. The idea was that by compressing the concrete, the chance of splitting failure would be reduced, thereby ensuring pull-out failure. Following this idea, the top plate was compressed. Three different levels of top plate compression were tested:

1. **Hand Tightened**: Specimens with no confinement applied are from Configuration 1: PT07 and PT09, and from Configuration 3: PT08. For these tests, the top plate was only hand tightened, which did not provide sufficient restriction, resulting in specimen movement. In Test PT09, the entire setup moved up, causing the LVDT to compress initially instead of elongating, see Figure 4-26. In Test PT08, the whole cage moved up (1.48 mm ↑). In Test PT07, the cage did not move, but the specimen moved up due to the compression of the felt layer during the pull-out test (1.3 mm ↑).

2. **Intermediate Prestressing**: Some confinement was applied to specimens from Configuration 2: PT05 and from Configuration 1: PT06. In these tests, the top plate was fixed tightly just to restrain the specimen, rather than being compressed excessively. All these tests yielded reasonable results. The camera setup (without DIC pattern) was used for these tests. The movement of the sample cannot be distinguished by visual inspection, so it can be ignored. The conclusion from these tests is that fixing the top plate tightly, but not excessively, was sufficient to restrain the specimens and prevent failure. For the final specimen, PT10, the top plate was compressed using a torque wrench, allowing for a quantifiable amount of prestress on each rod. When applying 80 Nm, a displacement of 0.28 mm at bottom left point of the specimen was measured by DIC. Iterating to 100 Nm, a displacement 0.22 mm was obtained. With continued increase in confinement did not reduce the displacement. It was determined to use 60-80 Nm for other tests is sufficient to prevent movement of the specimen. The confinement was calculated using Eq. 4.1 and Eq. 4-2 to achieve a compressive stress of 0.15 – 0.25 MPa prior to testing.

$$F = \frac{T}{Kd}$$ *Eq. 4-1: Torque to bolt force equation*

$$\sigma_c = \frac{F}{A}$$ *Eq. 4-2: Concrete stress*

Where T is the applied torque in Nm, K is the friction constant (typically ranging from 0.2 to 0.3), d is the bolt diameter (38 mm), and A represents the concrete surface area. It is worth noting that most confinement occurs during the pull-out test, where a pull-out force of 20 kN can result in a compressive stress of up to 2 MPa.

3. **Substantial Prestressing**: Significant confinement was applied to specimens from Configuration 2: PT03, PT04, and PT01, and from Configuration 1: PT02. Tests PT03 and PT04 involved compressing the top plate as much as possible, causing PT03 to fail by splitting before the test began, with similar results for PT04 (as shown in Figure 4-26). Overall, 3 out of the first 4 tests resulted in lower or barely any bond strength (failed tests). This can be explained by the excessive confinement, which led to the top plate bending. This bending caused concentrated stresses on the edges, resulting in tension stresses in the middle of the specimen, leading to premature splitting failure. Only test PT02 had reasonable bond strength, although this specimen also failed by splitting.

Influence of configuration

Comparing the pull-out results across all three configurations, it is challenging to determine the most optimal configuration due to procedural variations that significantly impacted the results. Most tests with configuration 2 failed, presumably due to excessive confinement, leaving configurations 1 and 3 for comparison. In configuration 1, three out of four specimens failed by splitting, whereas in configuration 3, none failed by splitting. Configuration 1 lacks a top unbonded concrete layer, while configuration 3 includes a 55 mm top unbonded region. The additional concrete mass in configuration 3 provides resistance against tensile stresses exerted by the rebar, enabling pull-out failure. Therefore, configuration 3 was chosen for further testing. Additionally, configuration 3 allows for the measurement of rebar slip at the free end, considered more accurate than top displacement as it does not include rebar strain.

4.4.3 Optimal Testing Procedure

As stated previously, the goal of the preliminary tests was to determine the optimal test setup, configuration and procedure for performing the pull-out test. The final test setup and procedure have already been presented in Ch4.4 Test Method. How and why these procedural decisions were made is made clear based on the presented results and procedural context.

A major procedural impact on the pull-out results is the amount of confinement applied to the concrete cubes. As mentioned in segment 4.4.2, the amount of confinement has much influence on the results. To little confinement will result in displacement of the specimens, while excessive might results on failure of the specimens. Additionally, the sequence of the procedure impacted these results. The rebars were clamped to the jack before confinement was applied, meaning compressing the top plate on the concrete while the rebar was fixed to the jack effectively started pulling out the rebars before the test began. Considering these impacts, the optimal procedure was determined. Optimal confinement was determined to be 60-80 Nm of torque on each bolt of the top plate. Additionally, the confinement should be applied prior to securing the rebar to the jack. The preliminary tests proved that pull-out failure could be obtained without displacement of the specimens, with this procedure.

4.4.4 Monitoring Devices and Mechanical Tests

Measurement Device

During the pull-out test, the vertical displacement of the rebar is measured by a Linear Variable Differential Transformer (LVDT). Measurements are taken at both the loaded end (top) and the opposing free end (bottom) of the concrete specimen, see Figure 4-24. For this type of test, measuring the lower rebar displacement is preferable to the top measurement. The bottom displacement provides a more accurate measurement as it does not include the elongation of rebar, which is included in the top LVDT measurement. To denote this difference, the bottom rebar displacement is referred to as slip.

The strain distribution along the reinforcement will be measured by Distributed Fiber Optical Sensors (DFOS), by means of the LUNA ODiSI 6100 system. DFOS are a novel measurement instrument increasingly adopted in civil structures and infrastructure as a monitoring solution (Barrias et al., 2019; Villalba & Casas, 2013). In the past, strain monitoring of reinforced concrete relied on strain gauges, which were applied internally or externally to concrete specimens. However, strain gauges have limitations: they provide measurements only at specific intervals and in limited quantities, offering only a partial view of strain distribution. In contrast DFOS offer a major advantage by providing a continuous strain profile along the entire length of the fibre, enabling a more comprehensive and detailed understanding of strain behaviour. In this study, DFOS is applied to measure strain, allowing for a more complete and accurate bond behaviour assessment compared to traditional methods. Each discrete measurement takes 5 strain recordings with a speed of 10 Hz with a spatial resolution of 0.65 mm at five seconds intervals.

Digital Image Correlation (DIC) will be employed on one side of the specimen using a Canon EOS 5DSR camera with a 35 mm lens. DIC will capture the strain field and any potential crack development during the test. DIC was also employed to measure drying shrinkage crack formation of the concrete. The camera setup used is as follows: aperture f/6.3, shutter speed 1/100, and ISO 100. During the pull-out test the strain measurements are taken simultaneously with the DIC pictures every 5 seconds. To guarantee precise outcomes, the DIC setup is calibrated prior to each test in order to minimise the level of noise. This calibration entails, adjusting camera focus light source angle and intensity. The noise level criteria are < 0.1% strain and < 0.02 mm displacement. The DIC setup can be seen in Figure 4-25.

Compressive and splitting tensile test

Compressive strength and splitting tensile tests are performed with the MATEST Cyber-Tronic press at the Stevin Laboratory, TU Delft. The compressive strength test is conducted in accordance with NEN-EN 12390-3, and the splitting tensile test follows NEN-EN 12390-6. Standardized concrete sizes of 100x100x100 mm or 150x150x150 mm are used. These correspond to the concrete sizes of the pull-out test specimens. The new replacement AASC steel samples are 150 mm, while the remaining reference CC samples are 100 mm. For 100 mm sized specimens, some cubes were obtained from wet-sawn 100x400 mm prisms. In the compressive strength test, a load rate of 13.5 kN/sec is applied. For the splitting tensile test, a thin wood piece is placed at the centre of the cube on both the top and bottom surfaces. The load for these specimens is applied at a rate of 1.1 kN/sec.

The compressive and splitting tensile strengths are calculated using the following equations:

$$f_c = \frac{F}{A_c}$$ *Eq. 4-3: Compressive strength*

$$f_{ct} = \frac{2*F}{\pi*L*d}$$ *Eq. 4-4: Tensile splitting strength*

5. Experimental Results

This chapter presents the results and analysis of the pull-out tests conducted on steel and prestressed reinforced test groups of Main Experiment specimens. The test groups are defined based on the curing age, condition and reinforcement type for each concrete type. Table 5-1 presents each test group along with the specimen ID.

During the pull-out test, the test is halted momentarily to readjust the LVDTs when they go out of range. In post-processing, these segments are removed, and the continuous test data segments are concatenated to provide a seamless bond behaviour diagram.

Table 5-1: Main Experiment test groups

		Curing age [days]			
	Reinforcement	28	84		168
	- sample size	Moisture	Moisture	Drying	Drying
CC	Steel – 100 mm	CC100-S-28d-M		CC100-S-3m-D	CC100-S-6m-D
	Prestressing strands – 100 mm	CC100-P-28d-M		CC100-P-3m-D	CC100-P-6m-D
AAC	Steel – 150 mm	ACC150-S-28d-M	ACC150-S-3m-M	AAC150-S-3m-D	
	Prestressing strands – 100 mm	ACC100-P-28d-M	AAC100-P-3m-M	AAC100-P-3m-D	

5.1 Mechanical Properties

Compressive strength

The main experiment's mechanical test findings are presented alongside the experimental results reported by Zhang et al. (2022) for identical 150 mm AASC and Nikhil (2019) for identical 100 mm CC under similar curing conditions. Figure 5-1 depicts the compressive strength development over time for both concrete mixtures CC and AASC. As previously stated, the experiment includes two sample sizes with cube dimensions of 100 mm and 150 mm.

For moisture-cured AASC specimens, the concrete compressive strength tends to increase over time, regardless of specimen size. Prolonged moisture cured AASC led to a 12.9% increase in compressive strength for 100 mm cubes and a 5.4% increase for 150 mm cubes compared to their 28d strength. When consider drying condition. Different behaviour over time is observed for CC compared to AASC. The reference CC specimen exhibited an initial reduction of 14% in compressive strength after being exposed to dry conditions for the first 56 days. This reduction is unusual and may be due to an unaccounted error, possibly during casting or testing. However, it is worth noting that such a significant reduction was not observed in Nikhil's tests. Subsequent drying for an additional 84 days resulted in a 12.4% improvement in compressive strength. Therefore, these results should be regarded with scepticism. The AASC specimens when exposed to drying exhibited an increase in compressive strength within the curing period of 84 days. The 100 mm AASC (green) concrete increased with 9.1% and the larger 150 mm cubes increased 18.0%.

For the 100 mm cubes, the moist-cured specimens showed a greater average strength gain than the dry-exposed specimens. Conversely, the 150 mm cube specimens exhibit a different pattern, with the dry exposed specimens demonstrating higher compressive strength. This difference in concrete strength can be attributed to the presence of eigenstresses (Awasthy et al., 2023). This phenomenon is more pronounced in larger concrete specimens, which might explain the strength gain differences between the different sized cubes.

Specimens subjected to drying will experience drying shrinkage, resulting in the development of eigen-stresses. As a result of uneven drying shrinkage over the concrete cross section. The external surface will undergo greater drying shrinkage in comparison to the internal concrete core. As a consequence, the outside surface experiences tensile stress while the concrete core experiences compressive stress. This eigenstress enhances the ability of the material to resist compression. Over time, the eigen-stress gradually diminishes as the inner concrete core undergoes drying. This is shown in Figure 5-1, which displays Zhang et al. (2022) results. After 190 days curing, the dry exposed concrete compressive strength levels off with time as the impact of eigenstress decreases. Comparing the results from present study to Zhang et al. (2022) can see that similar eigenstress effect is present for AASC exposed to drying and the results match closely, giving confidence in the validity of the results.

Furthermore, it can be observed that the smaller moisture cured 100 mm cubes have higher compressive strength than the bigger 150 mm cubes. This can be explained due to the size effect, smaller samples will exhibit larger mechanical strength than larger samples according to (Leung & Ho, 1996).

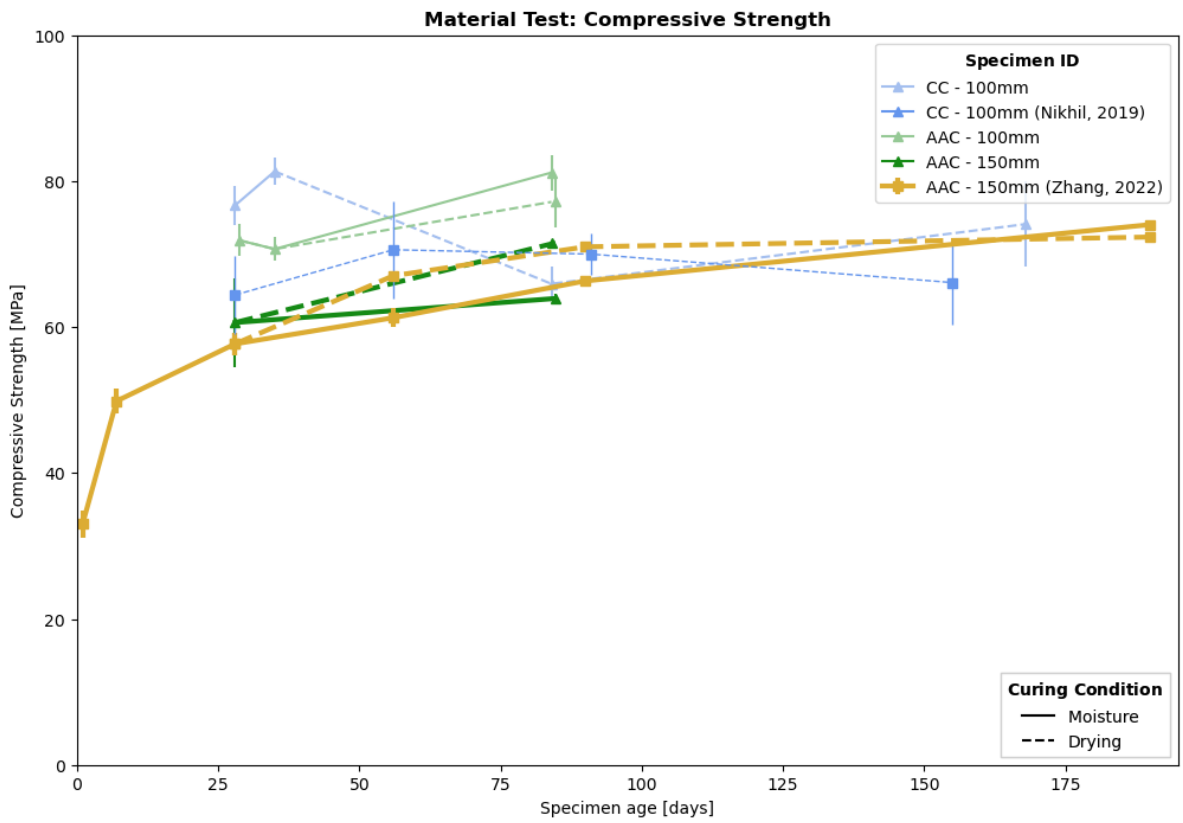

Figure 5-1: Development of compressive strength of CC and AASC over time

Tensile splitting strength

Figure 5-2 depicts the tensile splitting strength development over time for both concrete types. Throughout the first 56 days, the tensile splitting strength increases for all concrete samples. This increase is minimal in the 100 mm AASC samples but significant in the 150 mm samples, although the latter exhibit a large standard deviation. This variability remains unexplained, as no discernible differences in casting or testing procedures were noted. After 56 days, a decrease in tensile splitting strength is observed in both CC and AASC samples, as also reported by (Zhang et al., 2022). This decline may result from the diminishing influence of eigenstresses over time, as previously discussed.

In terms of curing conditions, the 150 mm moisture-cured samples display greater tensile strength than the dry-cured specimens. This outcome contrasts with the compressive strength results, where drying led to higher strength due to the eigenstress effect. These findings also diverge from (Zhang et al., 2022), where the eigenstress effect was more pronounced. However, due to overlapping standard deviations between specimens, the influence of eigenstress cannot be entirely discounted.

Furthermore, the size effect is evident, as CC specimens exhibit significantly greater tensile splitting strength compared to AASC specimens. The 100 mm AASC samples also reflect the size effect when compared to the results reported by (Zhang et al., 2022). However, the 84-day-old 150 mm specimens contradict this trend, although these results exhibit considerable variability.

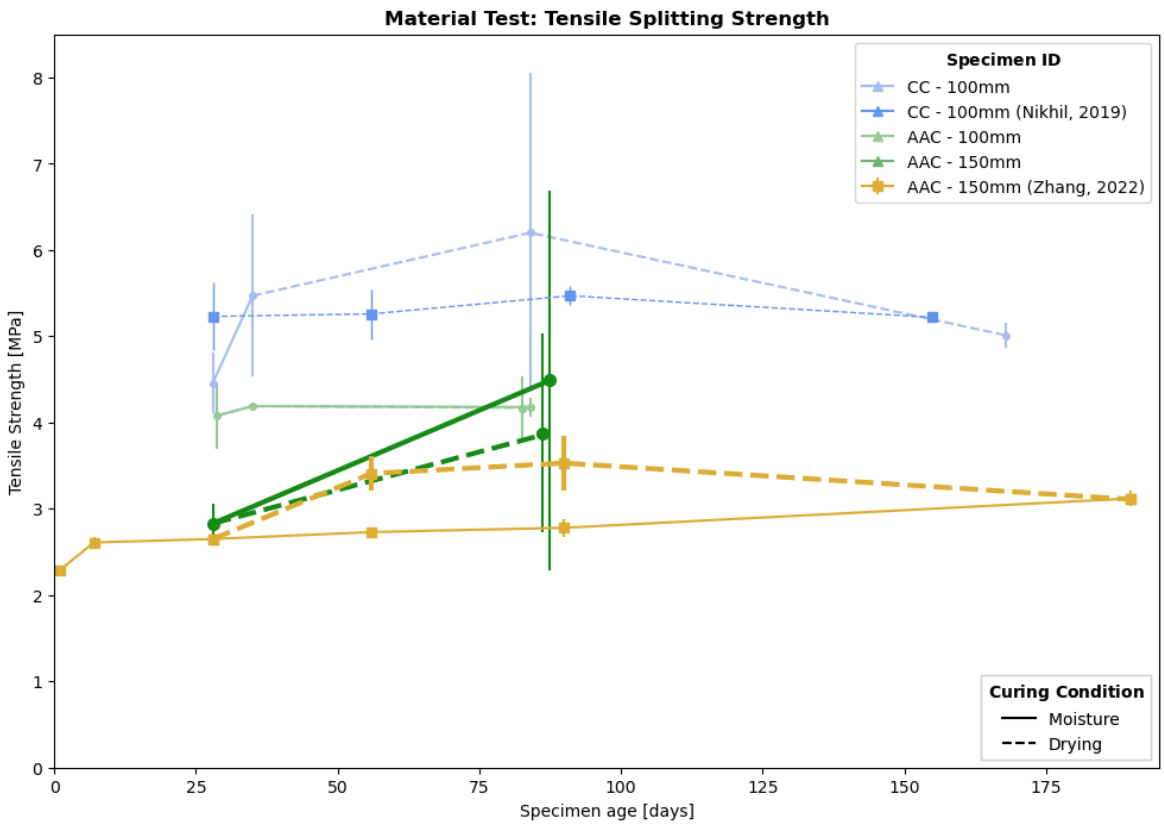

Figure 5-2: Development of tensile splitting strength of CC and AASC over time

5.2 Pull-out results

During the pull-out test, the maximum force and corresponding displacement are recorded. The bond strength is then calculated using a design bond length of 40 mm and applying the theoretical bond stress equation (Eq. 3.5). The bond strength pull-out test results for each specimen are provided in Table 5-2. Table 5-3 presents the mean and standard deviation of the bond strength for each test group. These values are a plotted in Figure 5-4 and Figure 5-18 to illustrate the bond strength development over time under different curing conditions more clearly.

Table 5-2: bond strength from pull-out test

	Curing Condition	M	M	D	D	M	M	M	D	D
	Age [days]	S – 28	S – 84	S – 84	S – 168	P – 28	P – 35	P – 84	P – 84	P – 168
Main Experiment	Specimen ID	CC100-S-28d-M		CC100-S-3m-D	CC100-S-6m-D	CC100-P-28d-M			CC100-P-3m-D	CC100-P-6m-D
	Batch	4		4	3	4	3		4	3
	CC100	26.05		19.58	26.06	7.08			12.82	12.38
		16.73		24.55	23.56	10.29			8.82	12.07
		22.44		21.00	20.9	10.05			13.35	11.92
	Specimen ID	AAC150-S-28d-M	AAC150-S-3m-M	AAC150-S-3m-D			AAC100-P-6m-M	AAC100-P-3m-M	AAC100-P-6m-M	
	Batch	10	11	11		6	8	7	7	
	AAC150	21.37	24.98	27.08			8.94	8.12	7.41	
		22.12	20.97	13.40			7.27	7.77	7.60	
		20.36	19.92	11.81			5.83	7.92	8.46	

Table 5-3: Average and standard deviation from maximum bond strength results

	Curing Condition	M	M	D	D	M	M	M	D	D
	Age [days]	S – 28	S – 84	S –84	S - 168	P – 28	P – 35	P – 84	P – 84	P - 168
Main Experiment		CC100-S-28d-M		CC100-S-3m-D	CC100-P-6m-D	CC100-P-28d-M			CC100-P-3m-D	CC100-P-6m-D
	CC100	mean std	mean std	mean std	mean std	mean std	mean std	mean std	mean std	mean std
		21.74 4.7		21.71 2.56	23.51 2.11	9.14 1.79			11.66 2.48	12.12 0.19
		AAC150-S-28d-M	AAC150-S-3m-M	AAC150-S-3m-D			AAC100-P-6m-M	AAC100-P-3m-M	AAC100-P-6m-M	
		mean std	mean std	mean std	mean std	mean std	mean std	mean std	mean std	mean std
	AAC100_P	21.28 0.88	21.96 2.18	17.43 6.85			7.35 1.56	8.56 0.7	7.89 0.67	

The bond strength, as determined by Eq. 3-5, is indicated on the y-axis. All the plots, unless otherwise indicated, display the displacement of the rebar as measured from the bottom of the specimen on the x-axis. The curing ages are represented by different colours, while the line style indicates the bond failure mechanism: a solid line for pull-out failure and a dashed line for splitting failure.

5.2.1 Steel reinforced specimens

The pull-out results for steel reinforced specimens are presented in Figure 5-3. On the left CC specimens are presented for 28 days moisture cured and subsequent 86- and 168-days age for specimens exposed to drying. The first test group CC100_28d_M (blue), the test was stopped shortly after reaching the maximum bond strength. This mistake was corrected for the ensuing test, where the test is continued till a bond strength plateau is reached. All the CC specimens, maintained their bond strength, regardless of curing condition or age. From a total of 12 pull-out test only 2 failed due splitting failure, as is indicated by the line type. On the right the AASC specimen are presented for 28 days (blue) and 86 days (green) moisture cured specimens. The 86-day old AASC specimens exposed to drying are presented in yellow. Prolonged moisture curing did not affect did bond behaviour of AASC over time. However, in contrast to the CC, the bond strength of AASC specimens exposed to drying was affected. With two out of 3 having significantly reduced strength. More over in the following segment.

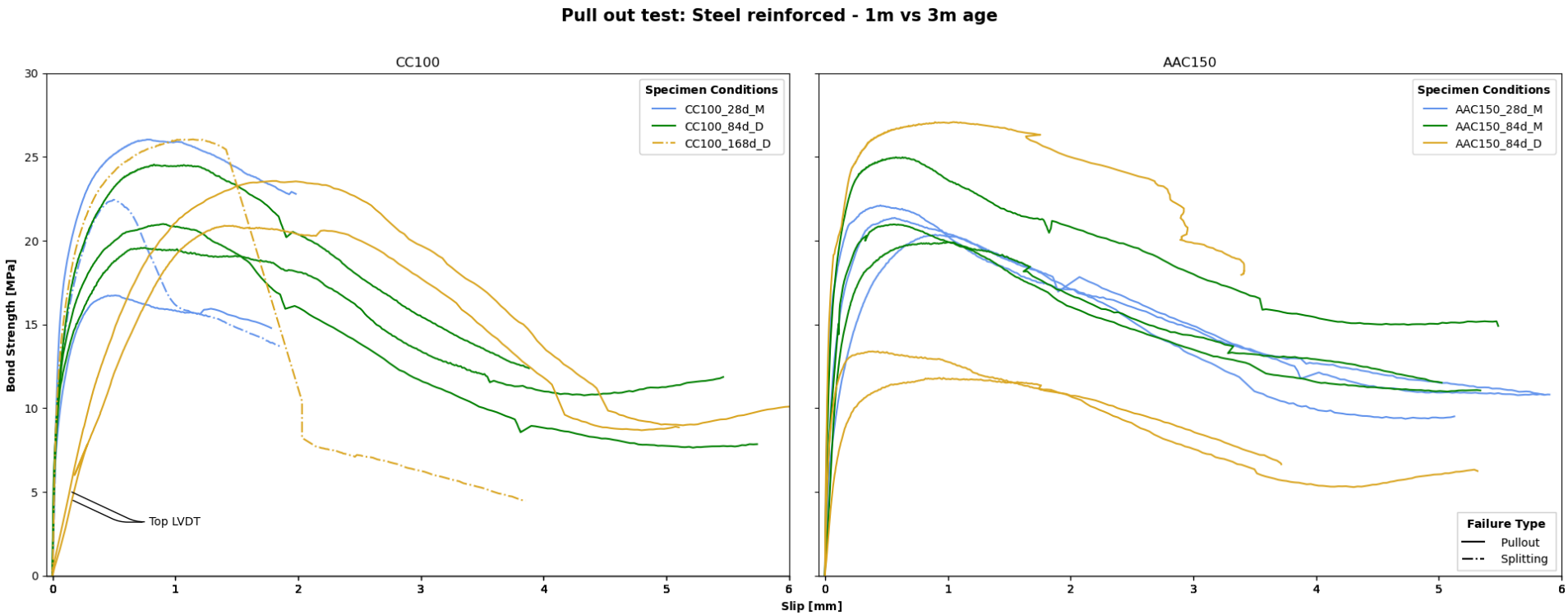

Figure 5-3: Pull-out test CC (100 mm) compared to AASC (150 mm) under different curing conditions over time

The pull-out results for steel reinforced specimens are summarized in Figure 5-4. This figure presents the average maximum pull-out bond stress for each test group, along with the standard deviation over time. AASC is depicted in green, whereas CC is represented in blue. The line type indicates the curing conditions: moist and dry. Th overall bond behaviour over time under varying curing conditions becomes clearer from this figure.

The results indicate that the bond strength of CC specimens remains unaffected under dry conditions. Moreover, it may experience a slight increase over time. This aligns with expectations, although CC does exhibit some material property degradation under drying in current study. This is regarded as an outlier, refer to Section 5.1 for further details. The stability of CC bond strength under dry conditions aligns with its consistent material behaviour.

Regarding the size difference, where CC specimens are 100 mm cubes and AASC specimens are 150 mm cubes, no clear difference in bond behaviour was observed. However, it is noteworthy that two CC specimens failed by splitting, while all AASC specimens failed by pull-out. This suggests that the larger AASC specimens may be better suited to ensure pull-out failure.

At first glance, the AASC specimens exposed to dry conditions (AAC150-84-D) exhibited a noticeable decrease in bond strength. However, a closer examination reveals a high standard deviation in the results, with two out of three specimens showing significantly lower bond strength. This suggests that drying may have some effect on bond strength, although this conclusion remains inconclusive due to a single specimen's exceptionally high bond strength.

To investigate this discrepancy, available tools and measurements were utilized. DIC results showed no discernible differences among the specimens. Additionally, the bonded sections were examined by splitting the specimen's post-test, and both the specimen with the unexpectedly high bond strength and the specimens with lower bond strengths had proper bonded length. This suggests that neither the increased bond strength in one specimen nor the reduced bond strength in others can be attributed to variations in bonded length. Of the three specimens, only one was monitored with DFOS for internal strain measurements, which indicated a significantly higher bond strength of 25.28 MPa compared to the 11.81 MPa observed in the other specimens. This suggests that the pull-out measurement should be higher. However, given the implementation challenges of DFOS in the present study (as detailed in Section 5.2.3), the lower bond strength values obtained from the pull-out test are considered more reliable. Given the consistent testing procedures across all specimens and the absence of identifiable irregularities, no definitive explanation for this discrepancy has been found. Consequently, the results for the AASC specimens under dry conditions remain inconclusive.

Since the goal of this research is to determine if AASC bond strength is affected by its reduced material properties, the decrease observed might be linked to these changes. Material tests have shown an increase in compressive strength when drying influenced by eigenstresses. Since bond strength typically correlates with material properties, the drop in bond strength cannot be attributed to compressive strength. Similarly, tensile splitting strength has shown a slight increase over the tested period, further ruling out these factors as explanations for the bond strength decrease. This suggests that the reduction in bond strength is not directly tied to compressive or tensile strength development, partially addressing the research question.

Another material property of AASC is its significant autogenous shrinkage, particularly during the first three weeks of curing (Li et al., 2018; Zhang et al., 2022). The considerable autogenous shrinkage is a notable disadvantage of AAS and AASF materials, as it may lead to micro- or macro-cracking in the concrete when employed under constrained conditions (Lura, 2003). In general concrete,

experiences some degree of constraint, either by some adjacent components or the steel reinforcement. This effect likely accounts for the decrease in stiffness (E-modulus) noted by Zhang et al. (2022) for the identical AASC utilised in the present study. Compressive strength principally relies on the (capillary) porosity of the concrete matrix, whereas splitting tensile strength is significantly more affected by microcracking. The significant autogenous shrinkage leads to the formation of microcracks surrounding the aggregates. The microcracking may also explain the reduced tensile splitting strength noted in the AASC specimens as compared to CC (Li et al., 2021). As a result, the lower tensile strength increases the probability of bond failure caused by micro-cracking in the concrete matrix. Unlike AASC, the 28-day moisture-cured CC specimens experience much less autogenous shrinkage, which means micro-cracking doesn't impact CC, and its bond strength remains unaffected. The micro-cracking in AAS, resulting from significant autogenous shrinkage, primarily occurs during the first month of curing while the specimens are kept under moisture conditions. When comparing the bond 28-day moisture cured bond strength of CC and AASC, it can be seen that these are comparable. Therefore, it can be concluded that the large autogenous shrinkage of AASC and the ensuing micro-crack formation does not impact the bond strength.

However, for AASC under dry conditions, drying shrinkage likely induces further micro-cracking within the concrete, contributing to the observed decrease in bond strength. Collins and Sanjayan (2001) reported significant micro-cracking in AAS samples exposed to dry conditions, attributing this to the material's larger porosity and coarser pore size distribution. Similar surface micro-crack development was observed in the present study (see Section 5.3).

Bond behaviour is intrinsically linked to the concrete's structural integrity. During the pull-out test, the wedging action generates tensile stresses within the concrete matrix. In samples exposed to dry conditions, where significant micro-cracking is present, the propagation of these cracks due to wedging increases the likelihood of premature failure during the pull-out test.

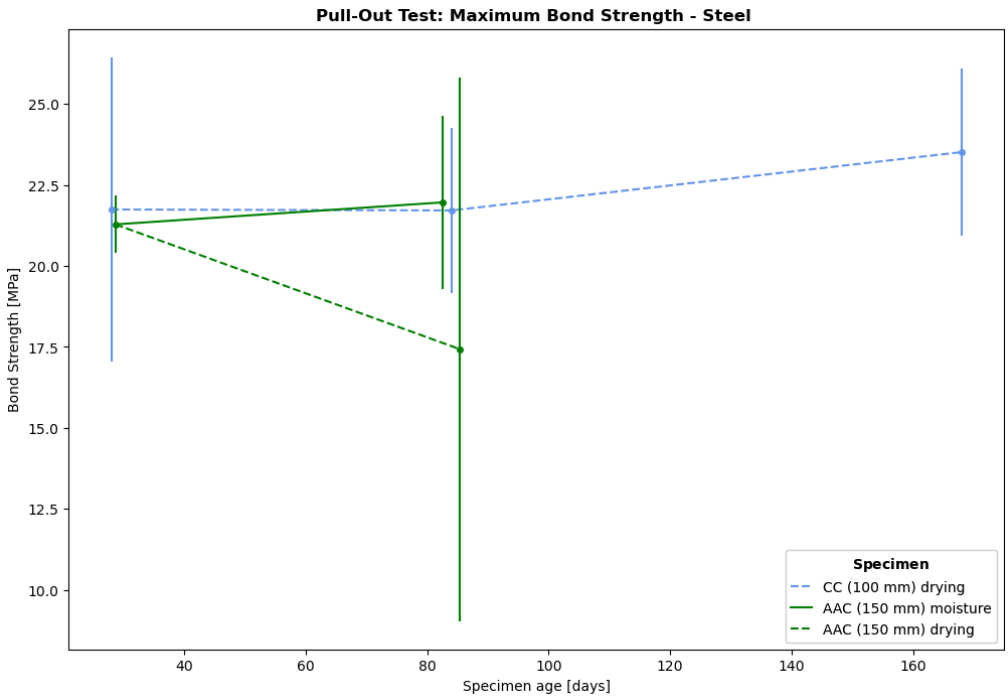

Figure 5-4: Bond strength development over time under different curing conditions: CC vs AASC

5.2.2 Steel reinforced specimens: DIC results

The crack formations obtained from DIC are presented in Figure 5-5 for CC and Figure 5-6 for AASC. The primary difference between the two concrete types is their size: CC specimens are 100 mm cubes, while AASC specimens are 150 mm.

Among the reference specimens (CC), only two tests failed due to splitting failure. These are specimens: CC100-S-28d-M#3 and CC100-S-6m-D#1, shown in Figure 5-5a and e. A closer look at Figure 5-5e reveals that the splitting failure originated from the bottom gap left by the wooden piece used to keep the rebar straight, as explained in Section 4.3.3. In theory, splitting failure occurs when tensile stresses exceed the concrete's tensile capacity. These stresses are typically induced by a wedging effect at the top of the concrete, not at the bottom. Therefore, this instance does not represent a conventional splitting failure, instead this stems from the concrete setup.

Figures 5-5f, 5-5g, and 5-6e present DIC imaging results, showing a distinct crack (highlighted in red strain colour) predominantly at the edges of the specimens. However, this is not indicative of actual crack development within the concrete. Instead, it occurs due to the application of a thick paint layer. During the confinement of the specimens, the excess paint likely breaks, resulting in the observed strain patterns.

Contrarily, not a single AAC specimen failed by splitting. This suggest that the larger concrete mass provides better resistance against the induced tensile stresses in the concrete during the pull-out test.

Figures 5-7 illustrate the development of splitting failure cracks in steel-reinforced AASC specimens. Key crack patterns are highlighted through DIC images at critical locations.

Figure 5-5: Steel reinforced CC specimens: DIC results

CC

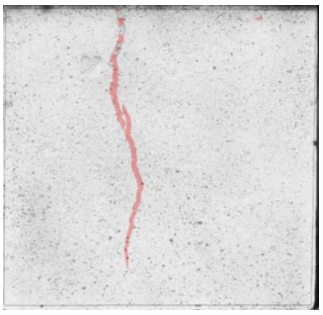

Figure 5-5a: CC-S-28d-M#3

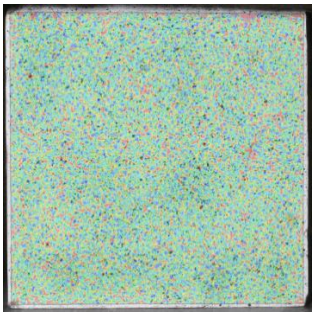

Figure 5-5b:CC-S-3m-D#1

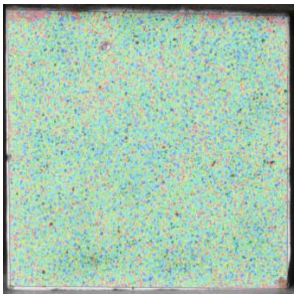

Figure 5-5c: CC-S-3m-D#2

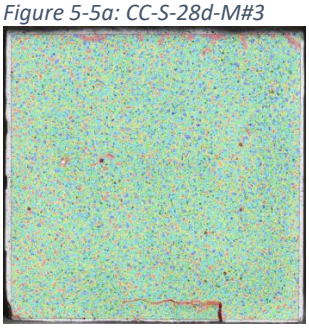

Figure 5-5d: CC-S-3m-D#3

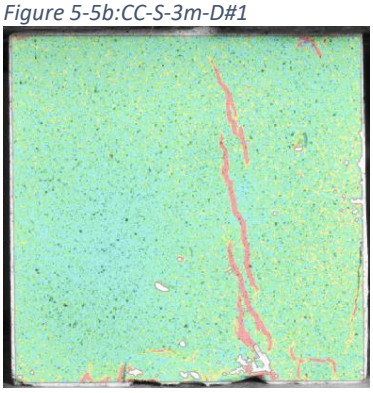

Figure 5-5e: CC-S-6m-D#1

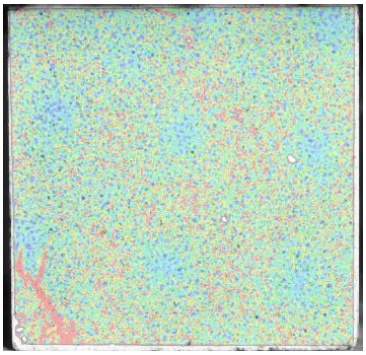

Figure 5-5f: CC-S-6m-D#2

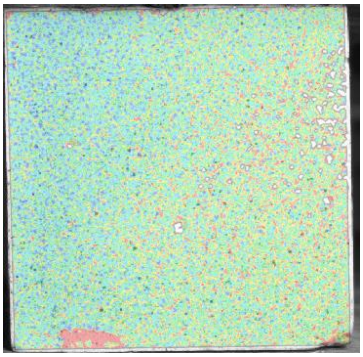

Figure 5-5g: CC-S-6m-D#3

Figure 5-6: Steel reinforced AAC specimens: DIC results

AAC

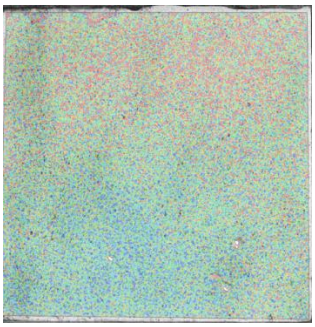

Figure 5-6a: AAC-S-28d-M#1

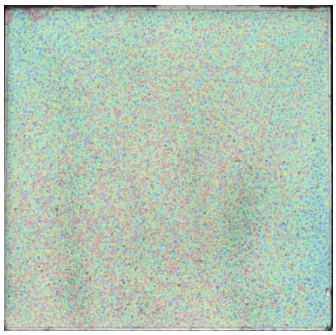

Figure 5-6b:AAC-S-28d-M#2

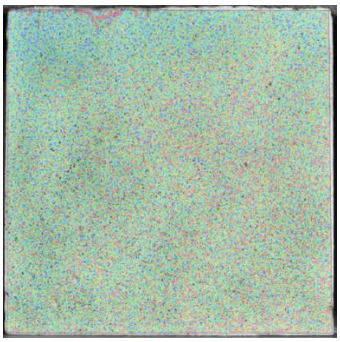

Figure 5-6c: AAC-S-28d-M#3

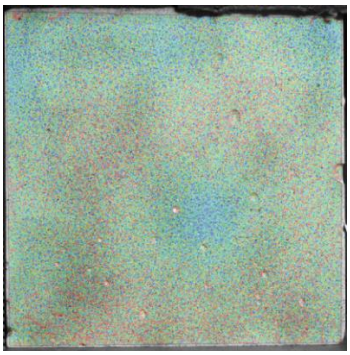

Figure 5-6d: AAC-S-3m-M#1

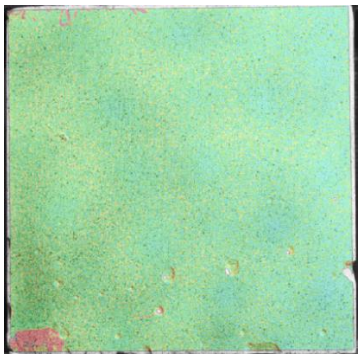

Figure 5-6e: AAC-S-3m-M#2

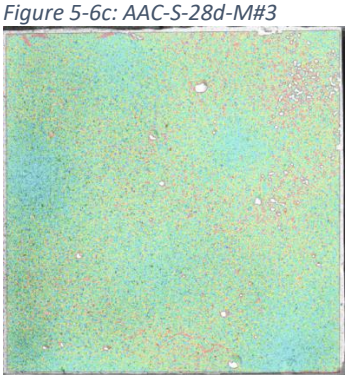

Figure 5-6f: AAC-S-3m-M#3

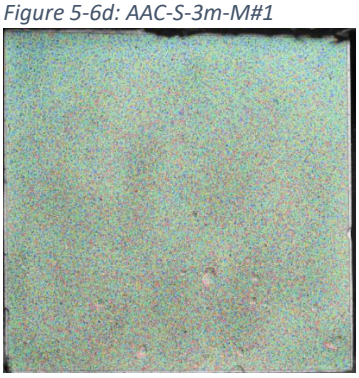

Figure 5-6g: AAC-S-3m-D#1

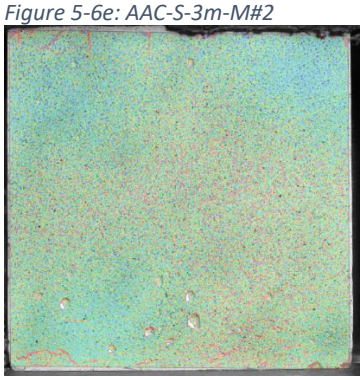

Figure 5-6h: AAC-S-3m-D#2

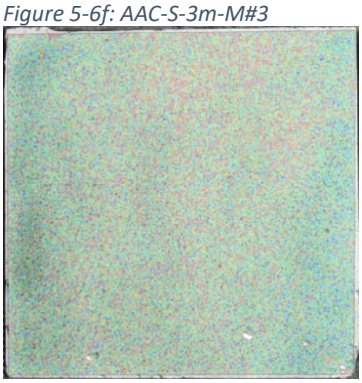

Figure 5-6i: AAC-S-3m-D#3

Figure 5-7: Steel reinforced AAC specimens with splitting failure mode: Bond behaviour and crack development

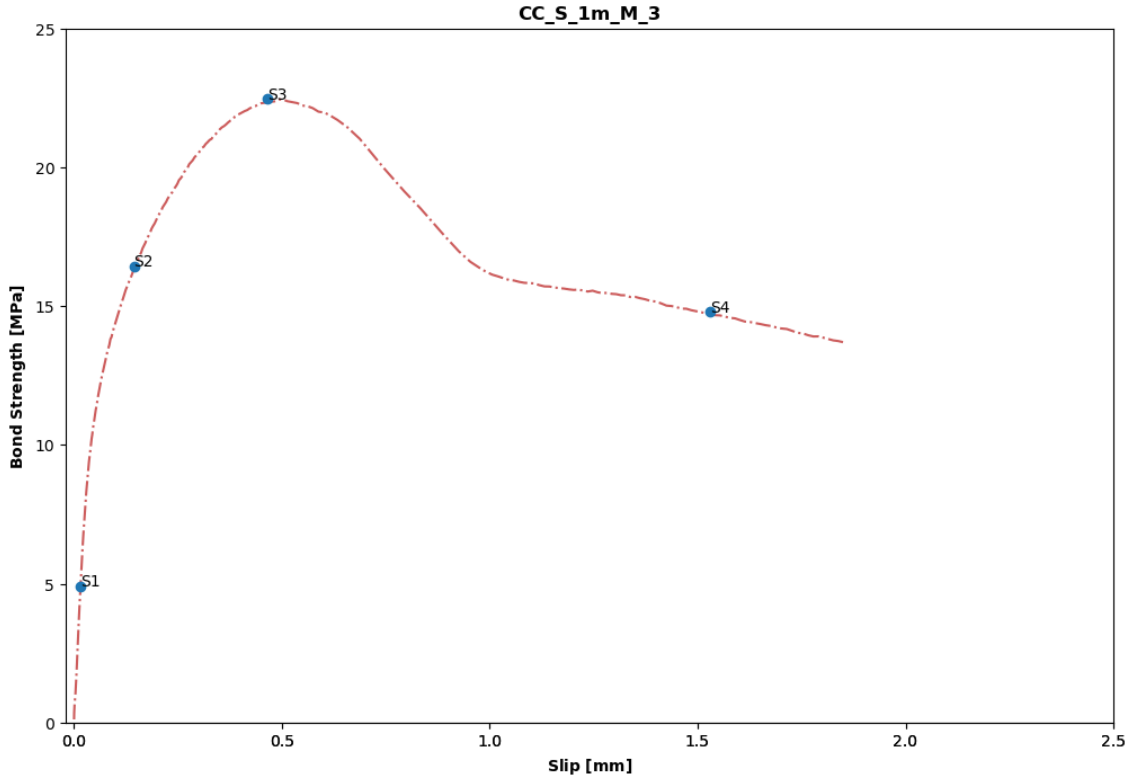

Figure 5-7a: Steel reinforced CC-28d-M#3: Bond behaviour and DIC imaging at key stages

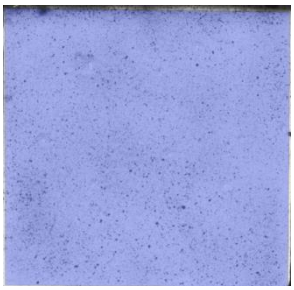

Figure 5-7b: DIC S1

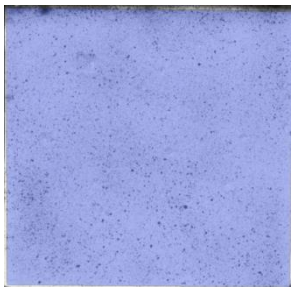

Figure 5-7c: DIC S2

Figure 5-7d: DIC S1

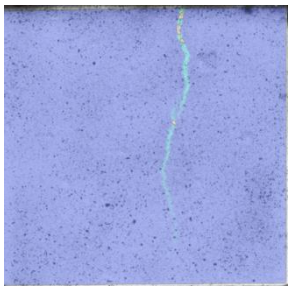

Figure 5-7e: DIC S1

Figure 5-7f: Post test splitting failure crack formation (top)

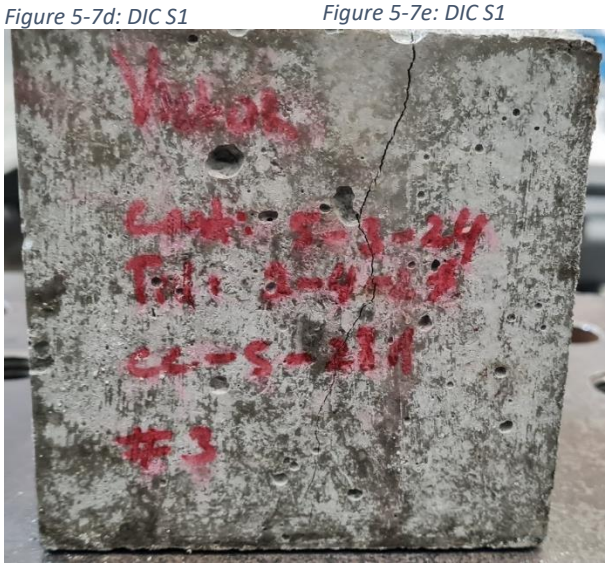

Figure 5-7g: Post test splitting failure crack formation (front)

5.2.3 Steel reinforced specimens: DFOS measurements

As previously stated, Distributed Fibre Optic Sensing (DFOS) is utilised in several steel-reinforced pull-out tests. The main aim of utilising this measurement equipment is to have a more profound understanding of the internal bond behaviour. The raw data acquired from these tests is processed to clearly present the relevant details. The data processing encompasses the following stages: data selection, data filtering, data smoothing, and calculation.

Data selection

The raw data acquired from each pull-out test with the ODiSi system generates two distinct .tsv files. The initial file, titled "[name]_full.tsv," has all strain data associated with each gauge position. The second file, "[name]_gages.tsv," specifies the designated positions of the DFOS profile, encompassing the concrete top surface, the commencement of the bonded segment, and the termination of the bottom segment. The gauge locations are displayed on the horizontal axis (x-axis), while the time of each recording is represented on the vertical axis (y-axis), accompanied with the respective strain records.

Section 4.4.4 (Monitoring Devices) specifies that five strain measurements are captured at a frequency of 10 Hz for each discrete measurement, occurring at 5-second intervals. The mean of these five measures is subsequently computed for each recording. Nevertheless, the data includes many "NaN" (Not a Number) values resulting from measurement errors. The "NaN" values are substituted with zeros to maintain uniformity in the dataset.

Data filtering

Strain is measured along the complete DFOS profile; however, only the embedded concrete segment is relevant for analysis. Consequently, the remaining data is excluded. Furthermore, local disruptions are eliminated. For example, as illustrated in Figure 5-8, significant strain peaks arise at the junction of the unbonded and bonded segment due to the rebar being encased in tape to secure the pipe in the unbonded zone (Figure 4-23). This encapsulation compresses the DFOS, resulting in elevated strain levels.

Prior to executing each pull-out test, a new reference state is established for the DFOS profile. This is performed to eliminate prior shrinkage readings and initiate a zero-strain profile. Nonetheless, the strain peaks observed at the unbonded-to-bond segment contact may lead to superposition errors when establishing a new reference state (Galkovski et al., 2021), see Figure 5-8.

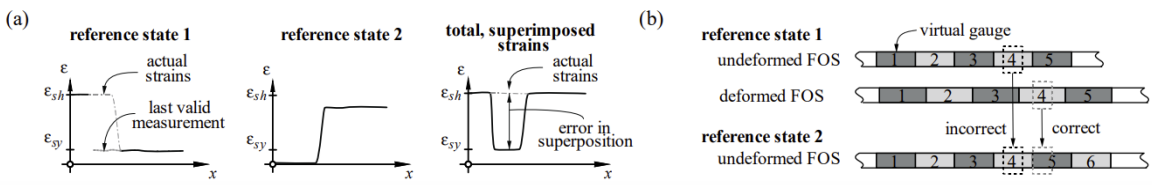

Figure 5-8: Superposition error (Galkovski et al., 2021)

To address this issue, any negative strain values (below zero) at the interface points are eliminated. This method is warranted, as the rebar experiences tension, indicating that the strain should be positive. Likewise, significant positive strain spikes at the interfaces are also eliminated.

Prior research conducted (Croppi and et. al, 2024), excluded strains over 4000 µm/m, equating to a steel stress of 4000 × Es = 800 MPa. This value surpasses the maximum yield strength of the steel.

Consider the following example corresponding to specimen AAC150-S-3m-M#3, see Figure 5-9. The presented measurement follows the data selection process, presenting only the bonded segment. The bond segment is denoted by the dotted black lines, while the dotted grey lines represent the unbonded sections. Clear peaks can be identified, as result of the aforementioned superposition error. To extend to which these peaks influence the measurement will become clear in following paragraphs.

The pull-out tests results indicate that the maximum pull-out strength is approximately 20 kN, signifying that the steel is not yielding. The following formula determines the anticipated maximum steel strain:

$$\frac{F}{EA} = \frac{20\ kN}{200000 * 50{,}26} \approx 2000\ \mu\mathrm{m/m}$$

Eq. 5-1: Strain estimate at maximum pull-out strength

As illustrated in Figure 5-9, the expected steel strain in the unbonded portion closely aligns with the estimated 2000 µm/m, hence instilling confidence in the results of the unbonded segment. It is worth noting that the DFOS measurement decreases back to 0 strain at the top side, instead of remaining at 2000 µm/m as indicated by the thick red line. This occurs because the DFOS fibre is not bonded outside the concrete specimen, and therefore, the strain recorded is 0.

Nonetheless, considerable superposition errors are detected at the bond-unbonded junctions. The recorded strain of around 3600 µm/m indicates a steel stress of over 700 MPa, suggesting steel failure, which is inaccurate as this did not occur during the pull-out test. Consequently, a more stringent filter of around 3500 µm/m may be implemented, contingent upon the data. The actual strain should resemble the red line in the graph, which represents a theoretical approximation of the bond behaviour. The bond strength begins to develop at the start of the bottom bond section, with a linear increase expected until the maximum bond strength is reached. After this bond section, a constant steel stress will follow. The maximum steel strain was calculated in Eq. 5-1 based on the maximum pull-out strength.

The disturbances resulting from superposition errors are explained and indicated by the blue circles in Figure 5-9b. Since the strain in these regions does not accurately reflect the actual strain, as demonstrated, they should be filtered out. When considering the maximum expected strain (the thick red line), it can be observed that all measurement data points exceed this limit. Given that the bond segment is only 40 mm in length, this suggests that the disturbances are significant enough to influence the outcomes for the entire bonded area, including the presumed undisturbed region (green rectangle). Therefore, applying a stronger filter in line with the expected maximum steel strain, as calculated in Eq. 5-1, would result in the loss of too many data points, rendering the results unrepresentative and unusable.

Data Smoothing

After the results have been filtered, a cubic spline is employed to interpolate the remaining data points following to the exclusion of outliers, see Figure 5-9. A Bessel filter is applied to smooth the strain curve, in accordance with the methodology utilised by Janiak et al. (2023). A Bessel filter is a low-pass filter that attenuates frequencies exceeding a given cut-off frequency. A 5th-degree Bessel filter with a cutoff frequency of 0.1 Hz is applied to the strain data.

Figure 5-9: Data filtering example specimen AAC150-S-3m-M-#3

Specimen configuration

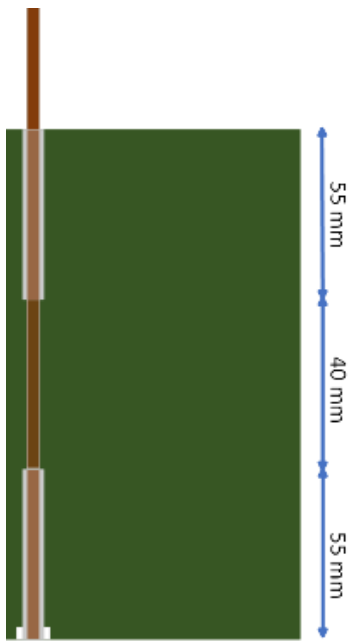

Figure 5-10a: Configuration specimen

AAC150-S-3m-M#3

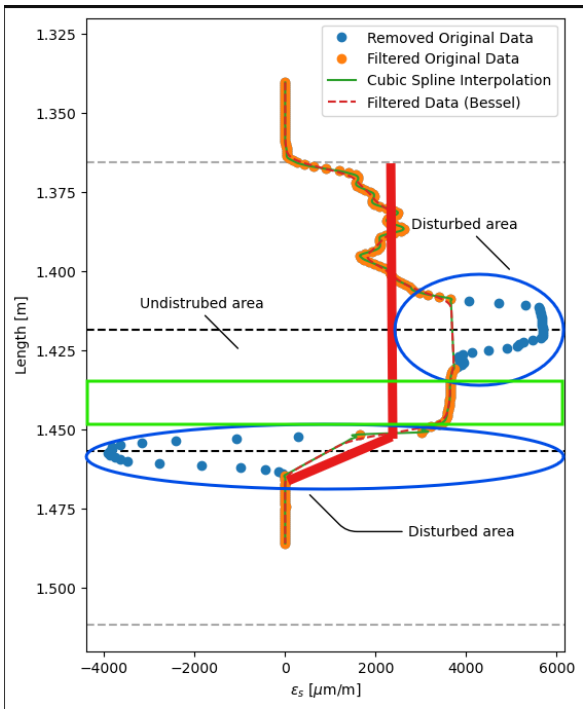

Figure 5-10b: DFOS measurement results processing

Calculations

Upon establishing the strain profile of the rebar, many mechanical parameters can be computed, including steel deformation, steel stress, and bond stress.

- The **steel stress** in steel is calculated by multiplying the strain ($\varepsilon(x)$) by Young's modulus E. Given that none of the pull-out experiments with DFOS data demonstrated rebar yielding, a linear-elastic material behaviour is assumed for the calculation of steel stress (Eq. 5-2).

$$\sigma = \varepsilon(x)\, E$$

Eq. 5-2: Steel stress

- **Bond stress** is computed using Equation *Eq. 5-3*, which is obtained from the equilibrium condition between the steel force and the bond force (refer to Section 3.3):

$$\tau(x) = \frac{d_b \Delta f_s}{4L} \left[{}^{N}/_{mm^2} \right]$$

Eq. 5-3: Bond stress

where: d_b is the rebar diameter, Δf_s is the steel stress difference between consecutive gauge locations and L is the total bond length.

In addition to the bond stress, the average bond stress is calculated. This is determined by integrating the bond stress over the bonded length and then dividing by that length. The designated bonded area was delineated before casting (dotted grey lines). Upon closer examination of the strain curves, it is evident that the new bond region is presumed to extend slightly longer, indicated by the blue dotted lines, from which the strain begins to increase from zero.

Following figures are the DFOS measurements. A schematic of the concrete specimen is illustrated. In the event of a splitting failure, the crack pattern is superimposed over the diagram. The steel profile, together with the associated bonded and unbonded regions, is illustrated with dotted lines across the mechanical quantities. Six load steps are selected for display according to a fraction of the highest steel stress attained. The initial six loads represent the increasing load fraction until the maximum pull-out strength is attained, indicated in red. The computed average bond stress is noted. The experimental bond stress derived from the maximum pull-out strength is also noted for comparison. Additionally, steel yield strain is indicated with a teal dotted line across the steel stress plot. The analysis of the following DFOS results, will consider key aspects discussed regarding the DFOS data processing explanation. These aspects include; data filtering, expected steel strain and comparison experimental bond stress and calculated internal bond stress.

Figure 5-10 presents the strain measurements for 28-day moisture-cured specimens. The results required minimal data filtering, as no significant disturbances were observed at the bonded section boundaries. The measured steel strain and stress are slightly higher than the expected experimental strain, suggesting that the steel may have just begun to yield, which was not indicated by the experimental results. Nonetheless, the DFOS results are reasonable and closely align with the expected values.

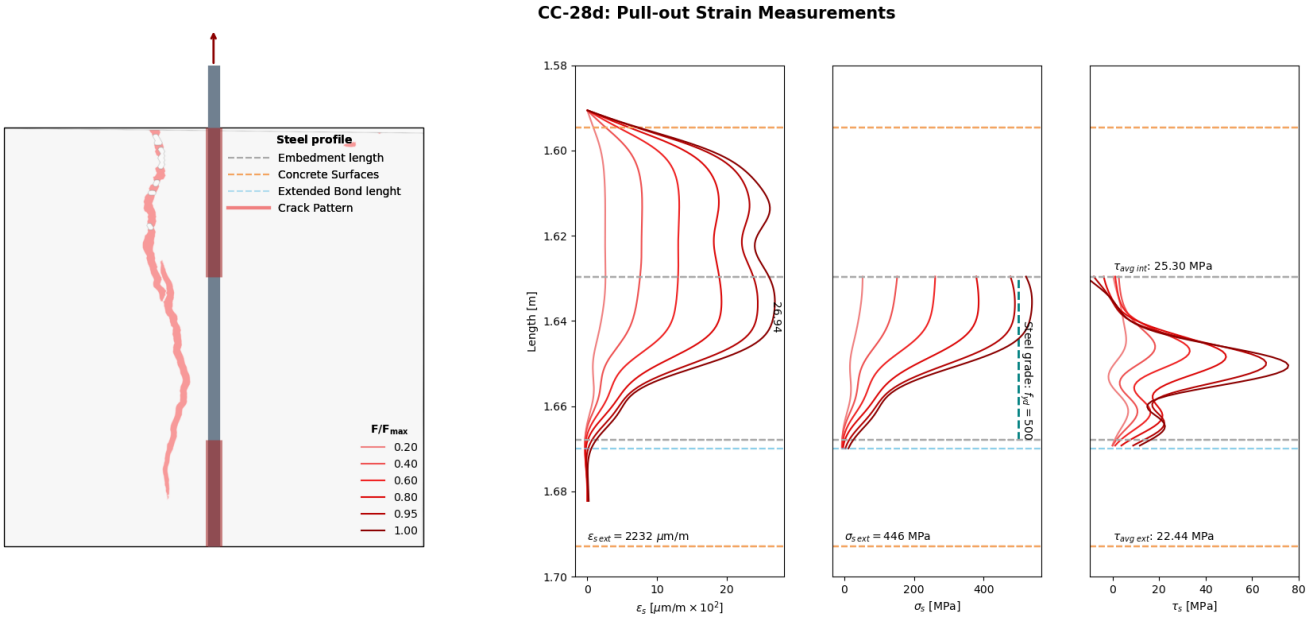

Figure 5-10: DFOS CC_28d_M – splitting failure

Figure 5-11 presents the strain measurements for 84-day dry-exposed specimens. These results required extensive data filtering due to significant disturbances observed at the bonded section boundaries. The measured steel strain and stress are considerably higher than the expected experimental strain, suggesting that the steel is yielding, an outcome not supported by the experimental results. Although the average internal bond strength is close to the experimental value, these results are not considered reliable.

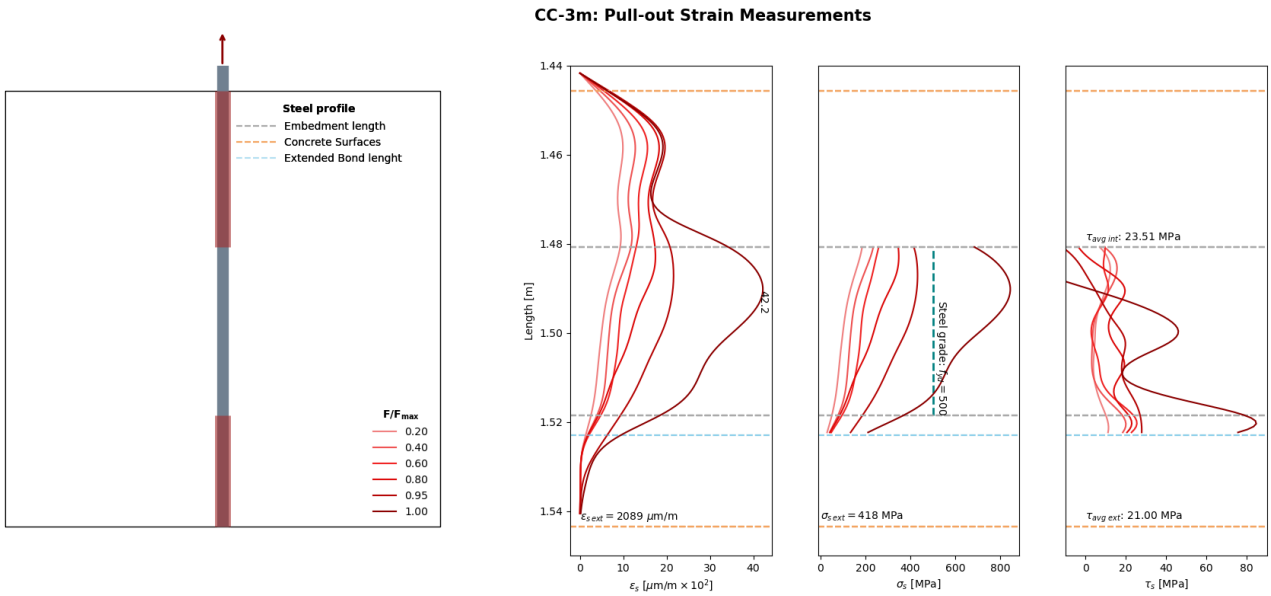

Figure 5-11: DFOS _CC_3m_D – pull-out failure

Figure 5-12 presents the strain measurements for 28-day moisture-cured specimens. The results required minimal data filtering, as no significant disturbances were observed at the bonded section boundaries. The measured steel strain and stress are lower than the expected experimental strain. These results are questionable, as it is unexpected that steel strain would continue to increase in the unbonded region or reach a maximum there, given the absence of bonding. This might be due to improper application of the DFOS. Ultimately, the calculated bond stress value deviates significantly below the expected value.

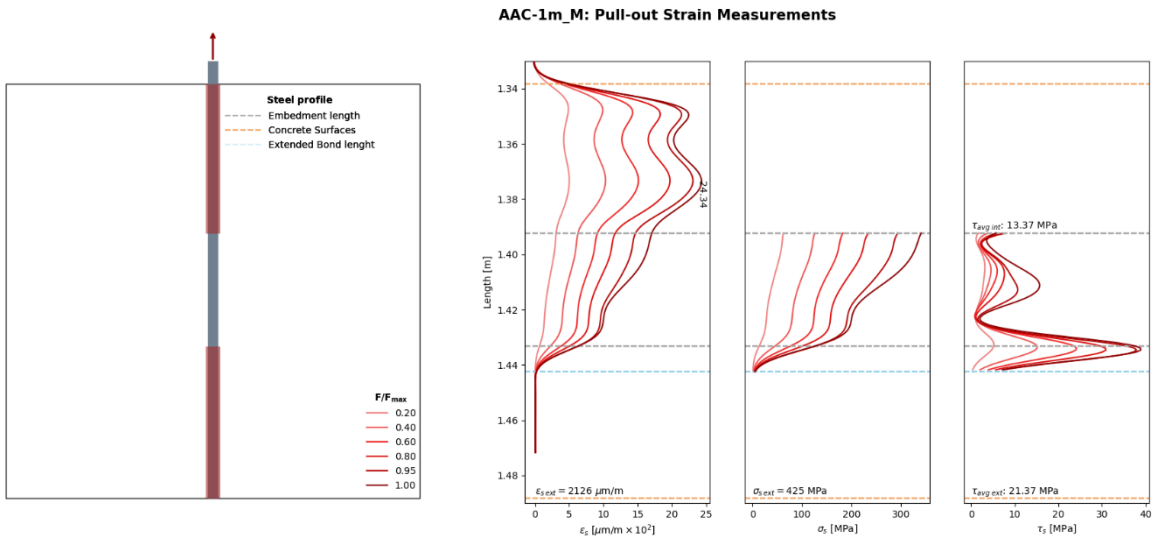

Figure 5-12: DFOS AAC_28d_M – pull-out failure

Figure 5-13 presents the strain measurements for 84-day dry-exposed AASC specimens. These results required extensive data filtering due to significant disturbances observed at the bonded section boundaries. The measured steel strain and stress are considerably higher than the expected experimental strain, suggesting that the steel is yielding, an outcome not supported by the experimental results. The bond strength determined from this measurement significantly exceeds the external bond stress.

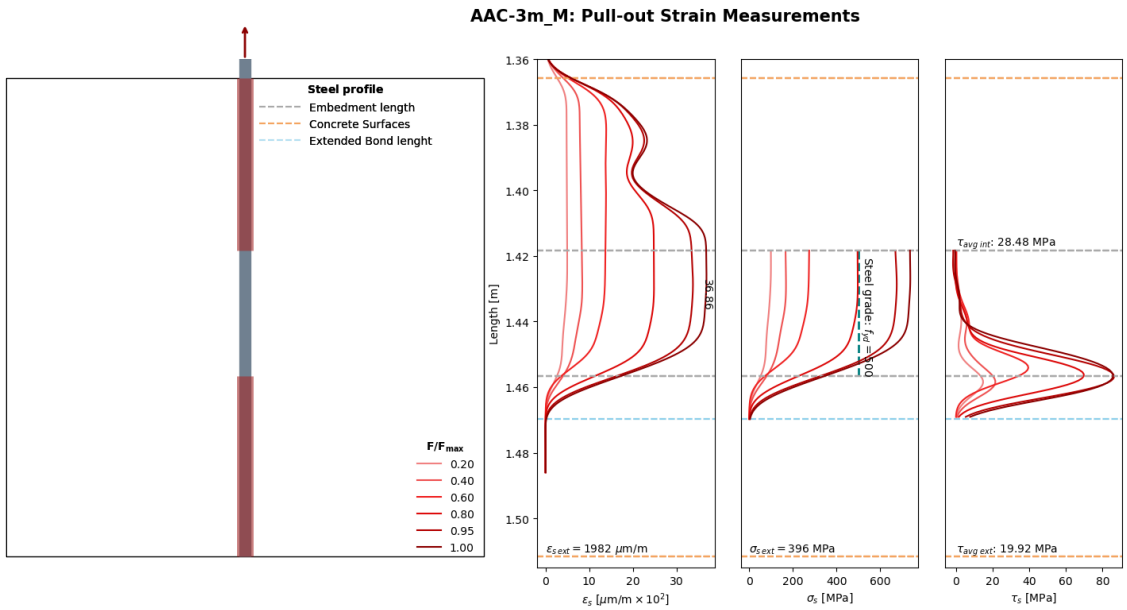

Figure 5-13: DFOS AAC_3m_M – pull-out failure

Figure 5-14 presents the strain measurements for 84-day moisture cured AASC specimens. These results minimal data filtering at the bonded section boundaries. The measured steel strain and stress are considerably higher than the expected experimental strain, suggesting that the steel may have just begun to yield, an outcome not supported by the experimental results. The bond strength determined from this measurement significantly exceeds the external bond stress.

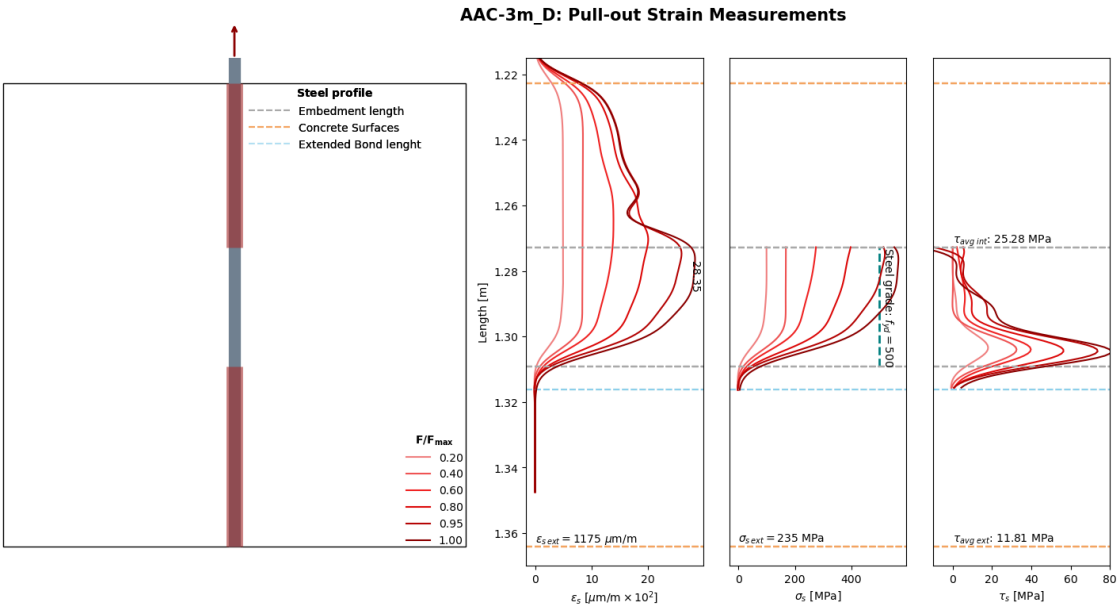

Figure 5-14: DFOS AAC_3m_D – pull-out failure

The most important findings from the DFOS are summarized in Table 5-4. These results indicate that DFOS measurement data requiring extensive filtering does not yield reliable results and is likely to overestimate bond strength. Conversely, a single measurement that did not require data filtering produced reasonable results. This supports the earlier conclusion that disturbances due to superposition errors at the boundaries impact the remaining bond segment, especially given the small bond length.

Table 5-4: Summary of findings: DFOS measurement results

	CC-28d-M	**CC-84d_D**	**AAC-28d-M**	**AAC-84d-M**	**AAC-84d-D**
Data filtering applied	No	Extensive	Minimal	Extensive	Minimal
Expected DFOS Strain/ Steel stress	close	Overestimate	Underestimate (dubious)	Overestimate	Overestimate
Expected Bond stress	close	Overestimate	Underestimate	Overestimate	Overestimate

With a better understanding of the data and the disturbances observed, modifying the DFOS setup to minimize these issues should be considered. For instance, not wrapping the tape tightly around the DFOS or in case this is still necessary, this could be performed at some distance from the bonded-bond boundary, therefore minimizing the disturbances in the bonded segment.

5.2.4 Prestress reinforced specimens

Processing data

During the pull-out test of prestressed specimens, some specimens exhibit a noisy zigzagging bond behaviour. This is explained by the prestressed reinforcement spiral shape. When the prestressed rebar is embedded in the concrete, this spiral geometry is imprinted on the surrounding concrete matrix, see Figure 5-15. During the pull-out test for this reinforcement to be pulled out smoothly the rebar should be able to rotate freely, when this does not happen the zigzagging bond behaviour occurs. At certain point the spiral grooves are broken and the prestress rebar suddenly slips. This is the zigzagging noise can be observed in Figure 5-16.

Figure 5-15: Spiral geometry of prestress reinforcement

Figure 5-15 a: Cross-section prestressed reinforced AASC

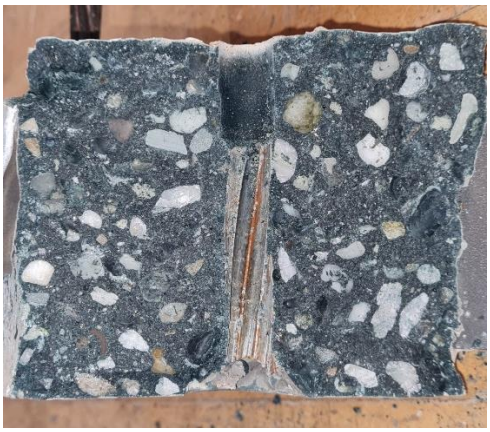

Figure 5-15 b: Spiral geometry imprinted in concrete matrix

To smoothen these curves the Savitzky-Golay filter is used. This method uses the convolution process, where successive data points are fitted with a 5th degree polynomial by the linear least squares method. The window size for the successive data points was chosen iteratively. A window size of 50 measurement points is taken from prestress data files of 600-1200 data points. This equates to 0.5 – 1 mm slip. An example of the Savitzky-Golay filter applied to the noisy zigzagging data is presented in Figure 5-16.

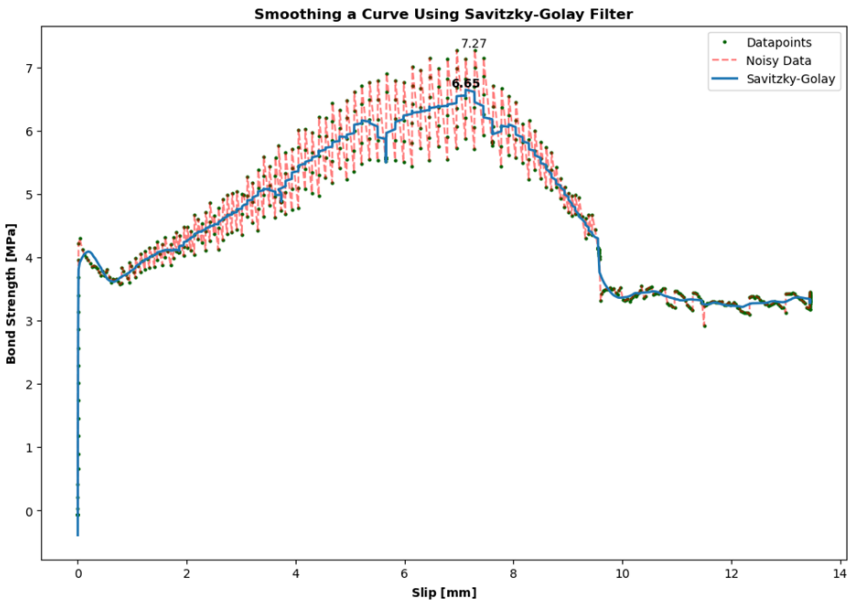

Figure 5-16: Smoothening of noisy data

The prestressed reinforced concrete specimens are displayed in Figure 5-17. All these specimens failed by splitting failure. Depending on the noisy amount some curves have been smoothed with the Savitzky-Golay filter.

Figure 5-17: Prestressed reinforced concrete results

The pull-out results for prestressing strand reinforced specimens are summarized in Figure 5-18. This figure presents the average maximum pull-out bond stress for each test group, along with the standard deviation over time. AASC is depicted in green, whereas CC is represented in blue. The line type indicates the curing conditions: moist and dry. Th overall bond behaviour over time under varying curing conditions becomes clearer from this figure.

Concerning the outcomes for prestressing strands, it is clear that CC exhibits superior bond strength than AASC. Bond strength is associated with both compressive strength and tensile splitting strength. The enhanced bond strength in prestressed strands reinforced CC is attributable to the superior tensile splitting strength exhibited by these specimens. Nonetheless, this disparity in bond strength was absent in the steel-reinforced specimens, where the bond strength of both concrete types was similar, despite CC exhibiting superior tensile splitting strength. This can be explained by the difference in failure modes. Prestressed reinforced specimens all failed by splitting failure, indicating that the material properties, particularly tensile strength, play a key role. Therefore, the greater tensile strength of the CC concrete is reflected in the performance of the prestressed reinforced specimens, but not in the steel-reinforced specimens, where the failure mode is different.

The apparent reduced bond strength in prestressed, AASC-reinforced concrete compared to CC can be attributed to the geometry of the reinforcement and the different bond transfer mechanisms involved. In ribbed rebars, the primary mechanism for bond transfer mechanism is bearing resistance, while friction contributes minimally. Conversely, for prestressed strands, the smoother surface renders friction the predominant mechanism for bond transfer. This is substantiated through evaluation of bond strengths: Steel-reinforced specimens, despite their smaller rebar diameter and embedding length, exhibited significantly greater bond strength than those reinforced with prestressing strands. Therefore, the lower concrete tensile splitting strength in AASC likely explains the reduced bond strength in prestressed specimens. The higher tensile strength in CC ensures the concrete matrix remains intact, allowing for stronger bond performance.

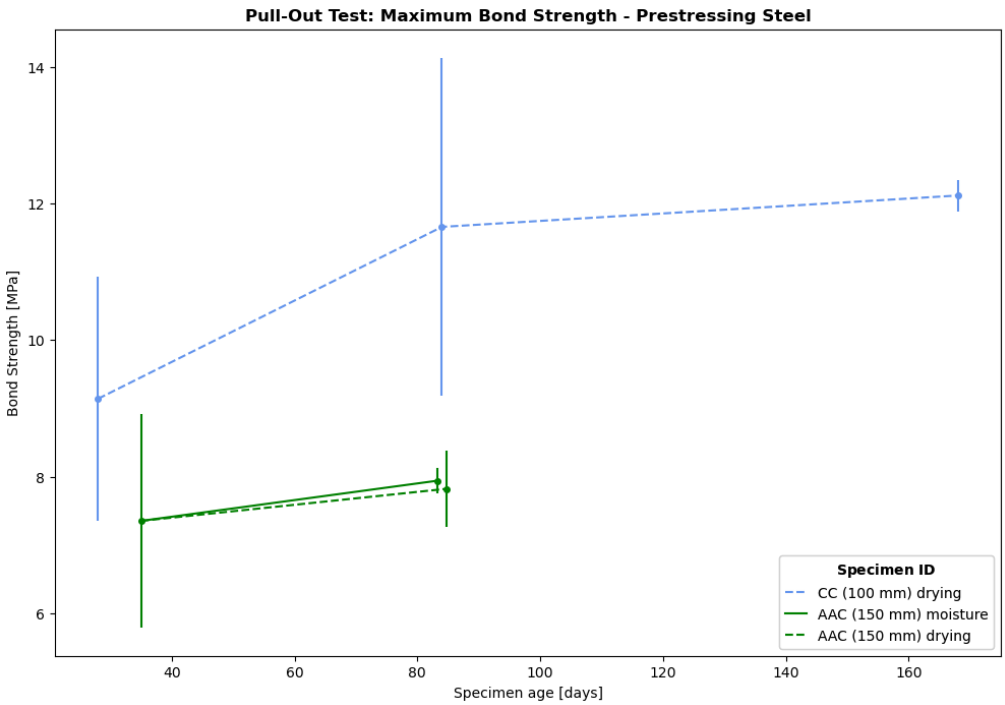

Figure 5-18: Bond strength development over time under different curing conditions: CC vs AASC

5.2.5 Prestress reinforced specimens: DIC results

The crack formations captured with DIC are shown in Figure 5-19 for both CC and AASC. Unlike the steel-reinforced specimens, the prestressed reinforced specimens for both concrete types are of the same size. In all cases, both concrete types experienced splitting failure, which can be attributed to the dominant bond transfer mechanism. Here, bond transfer relies primarily on friction resistance, generating radial tensile stresses that, once they exceed the concrete's tensile strength, lead to splitting failure. The absence of mechanical interlock and the larger strand diameter further exacerbate this issue, making prestressed reinforced concrete more susceptible to splitting failure than steel-reinforced concrete.

Figure 5-20 illustrates the development of splitting failure cracks in prestressed-reinforced AASC specimens. Key crack patterns are highlighted through DIC images at critical locations.

Figure 5-19: Prestressed reinforced specimens crack pattern: splitting failure

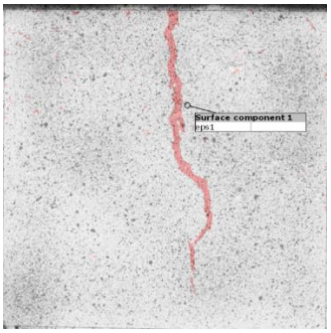

Figure 5-19 a: CC-28d-M-1

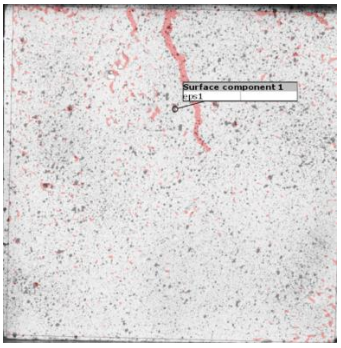

Figure 5-19 b: CC-28d-M-2

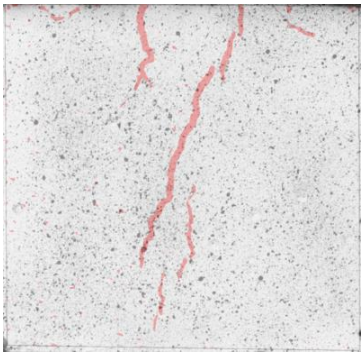

Figure 5-19 c: CC-28d-M-3

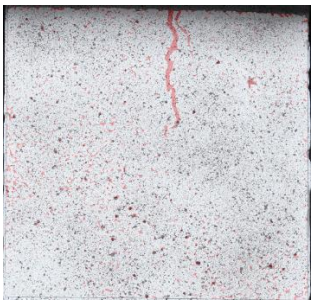

Figure 5-19 d: CC-3m-D-3

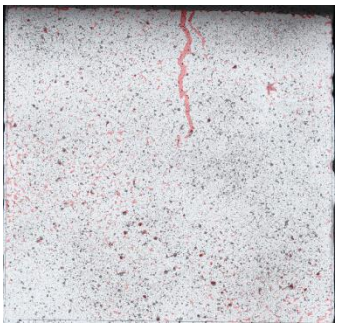

Figure 5-19 e: CC-6m-D-3

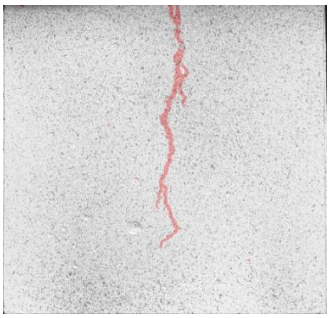

Figure 5-19 f: AAC-3m-M-1

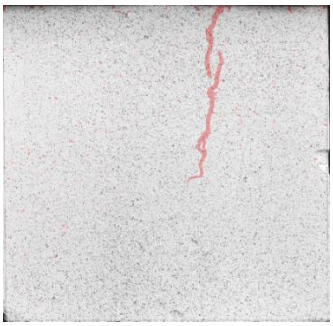

Figure 5-19 g: AAC-3m-M-2

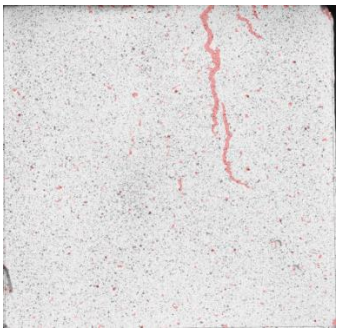

Figure 5-19 h: AAC-3m-D-3

Figure 5-20: Prestressed reinforced AAC specimens with splitting failure mode: Bond behaviour and crack development

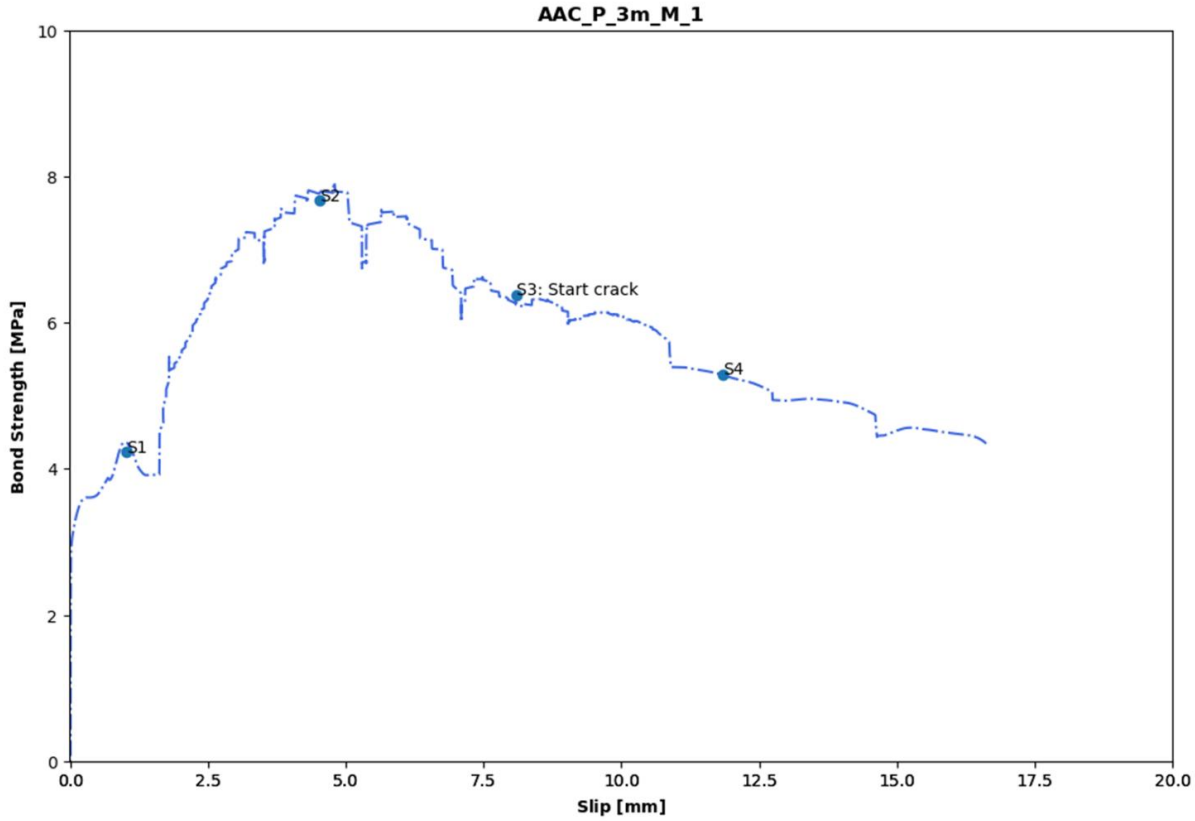

Figure 5-20a: Steel reinforced AAC-3m-M#1: Bond behaviour and DIC imaging at key stages

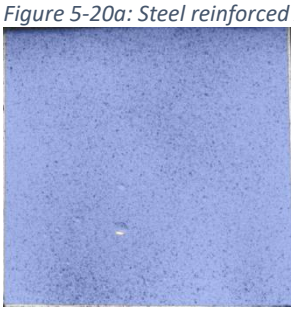

Figure 5-20b: DIC S1

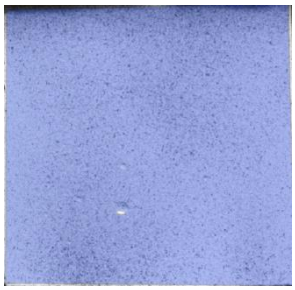

Figure 5-20c: DIC S2

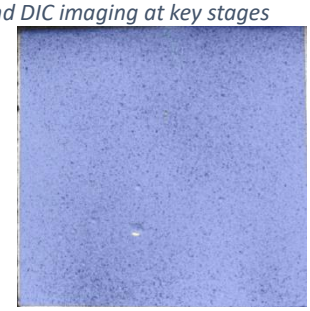

Figure 5-20d: DIC S3

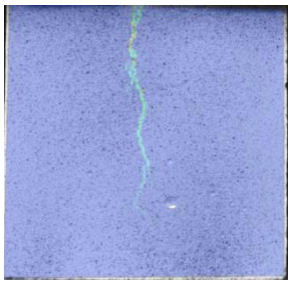

Figure 5-20e: DIC S4

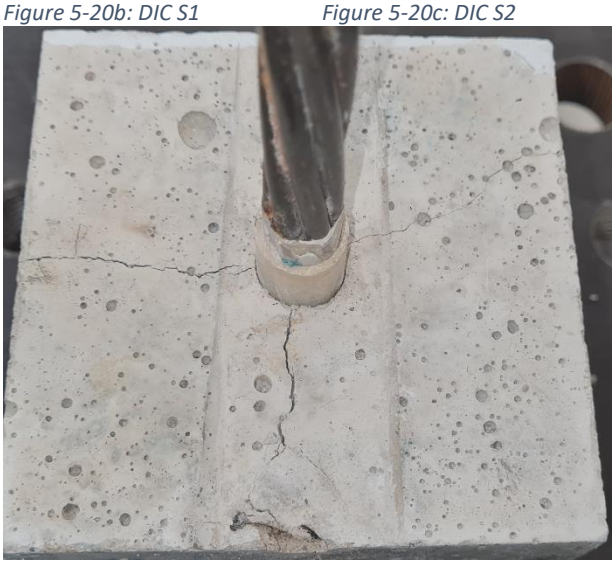

Figure 5-20f: Post test splitting failure crack formation (top)

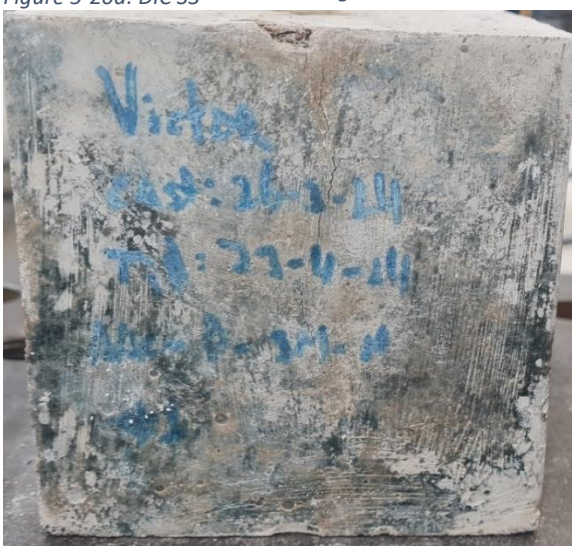

Figure 5-20g: Post test splitting failure crack formation (front)

5.3 Drying shrinkage

Following an initial 28 days of conventional moisture curing, certain AASC specimens were subjected to drying. To visualise the impact of drying on AASC specimens, DIC observations were performed over the initial 7 days after exposure to drying. Figure 7-19b presents these results. Significant cracks are visible. The extent of drying shrinkage fractures is not visible in concrete composite (CC), see Figure 5-19a. This corroborates the significant drying shrinkage cracks documented in earlier research (Li et al., 2021). Similar micro-crack pattern was observed by (Collins & Sanjayan, 2001), for AASC exposed to dry conditions. The significant micro-cracking was attributed larger porosity and coarser pore size distribution.

Figure 5-21: DIC drying shrinkage results: CC vs AAC

CC

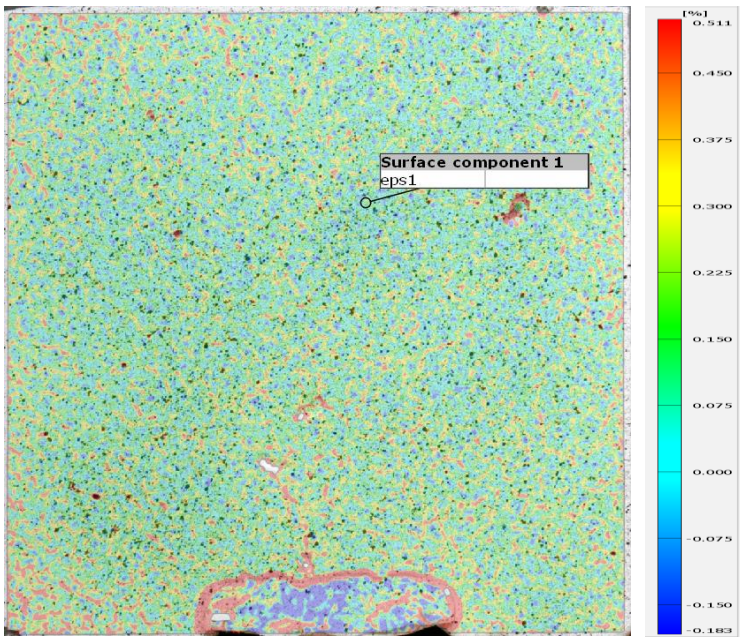

Figure 5-21a: DIC drying shrinkage results CC: 28 days

AASC

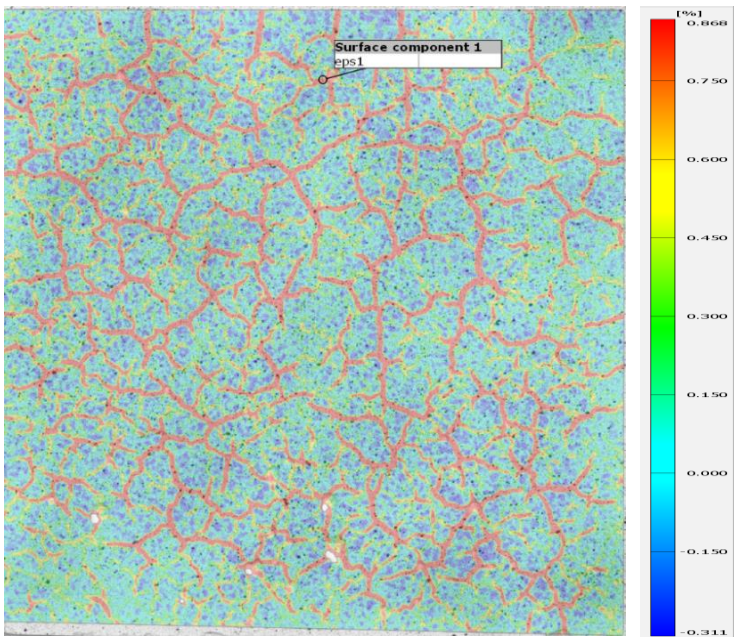

Figure 5-21b: DIC drying shrinkage results AAC: 7-days

Figure 5-22: Drying shrinkage microcrack development: first week

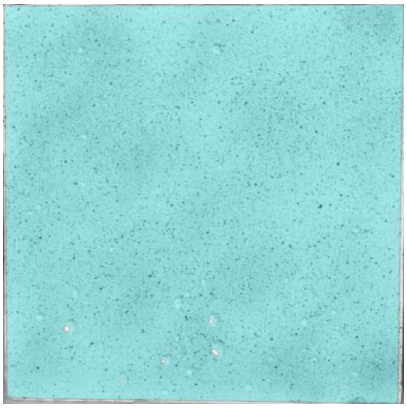

Figure 5-22 a: First exposure

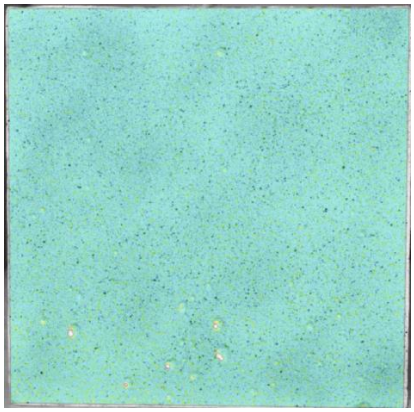

Figure 5-22 b: 1 Day

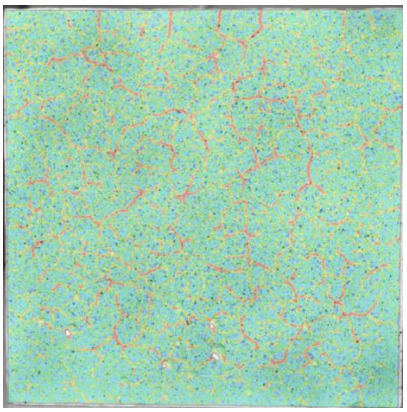

Figure 5-22 c: 2 Days

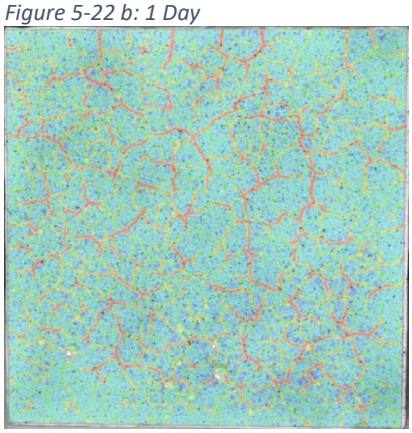

Figure 5-22 d: 3 Days

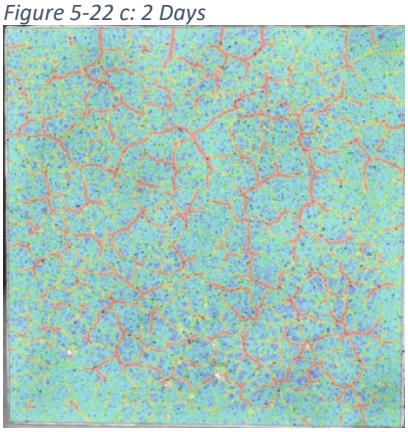

Figure 5-22 e: 4 Days

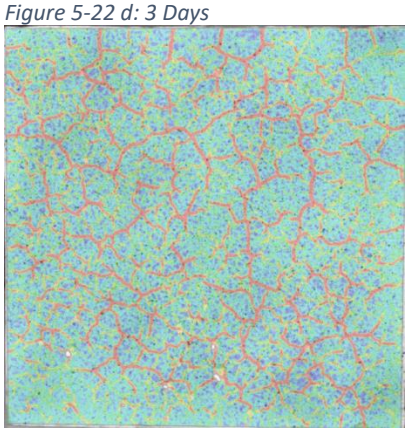

Figure 5-22 f: 5 Days

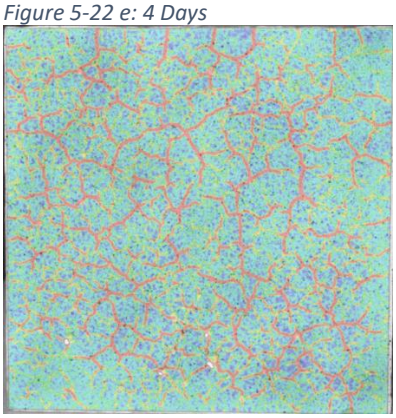

Figure 5-22 g: 6 Days

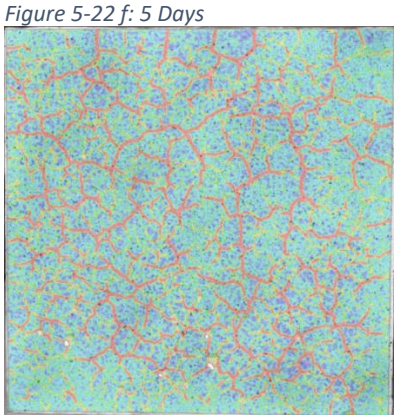

Figure 5-22 h: 7 Days

6. Comparison of Analytical and Experimental results

Many studies have already compared the bond qualities of AASC to conventional concrete models (Sofi et al., 2007; Topark-Ngarm et al., 2015). However, these models entailed shorter term studies. Therefore, the alarming decrease in material properties of AASC and its effect on the bond behaviour has not been analysed yet. The aim of this chapter is to determine if or in what capacity established models can be implemented to determine the bond strength for AAC concrete after said specimens have been exposed to drying for some time. Therefore, this chapter will discuss the 3rd research question: *"What is the applicability of existing models for the bond behaviour of conventional concrete on that of AAS considering the time dependency?"*

As discussed in Chapter 3, bond behaviour is dependent on various parameters including: concrete cover, reinforcement diameter or type, embedment length and concrete strength to name a few. Many of these variables are not incorporated in the theoretical model (Eq. 3-5). Hence, it is difficult to predict bond strength. Therefore, many researchers relied on semi-empirical models to estimate the bond strength. A few of these semi-empirical models will be discussed along with the code standards for bond strength: AS 3600, ACI 318 and EC2.

6.1 Bond strength prediction models

OJB Model 1977

Orangun et al. (1977) asserted that a crucial aspect in determining the bond behaviour is dependent on the angle (β). This angle determines the radial component of the bond force (u_r) that is exerted onto its surroundings, Figure 6-1. The cover lengths C_s and C_b, which stand for horizontal and vertical cover lengths, are in large part determined by this angle. Hence, β can vary greatly ranging from 45-80° depending on assumptions made. Therefore, an empirical approached seemed more promising. Orangun conducted a nonlinear regression analysis on empirical results of lap spliced beam tests to determine the bond strength (u_b).

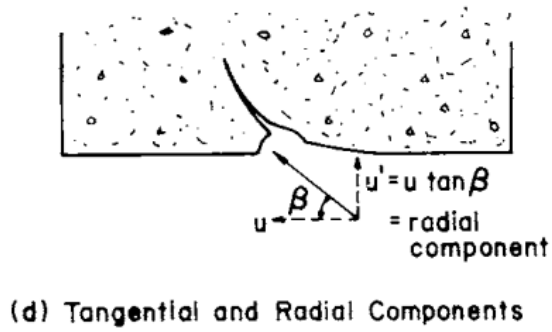

Figure 6-1: Radial component bond stress (Orangun et al., 1977)

Orangun semi-empirical model reflects the effects of concrete cover ($C = \min(C_s, C_b)$), rebar diameter (d_b), length (l_s) and concrete strength (f_c').

$$\frac{u^*}{\sqrt{f_c'}} = 0.083045\left[1.2 + \frac{3C}{d_b} + \frac{50d_b}{l_s}\right]$$

Eq. 6-1: Bond model by Orangun et al. (1977)

This model is based on empirical tests with concrete cover to rebar ratio $C/d_b < 2.5$, were splitting failure was the dominant failure mode. In regards to this study the $C/d_b < 5.75$ and $C/d_b < 3.38$ for steel rebar Ø8 mm and prestressing steel Ø12.9 mm respectively. As for larger C/d_b ratios the failure mode may be pullout failure instead of splitting failure. Therefore, Orangun recommends to use $C/d_b = 2.5$ in these cases.

Darwin 1992

Building upon the previous bond prediction model developed by Orangun, Darwin et al. (1992) aimed to limit unintentional bias in the test data. Darwin denoted the following biases in data set used by Orangun. Larger rebars had greater lateral spacing C_s compared to smaller rebars. Therefore, resulting in a larger C_s/C_b ratio. This has positive influence on the bond strength. Darwin also noted a disparity in the size of coarse aggregates in the concrete specimens. When compared to larger aggregate sizes, smaller coarse aggregates are likely to produce lower fracture energy. Furthermore, higher strength steel rebars were used for larger rebars compared to the smaller rebars. These biases were not filtered out of the data set used by Orangun, before he performed his regression analysis. In addition to filtering out the data set, Darwin used a different approach. Using the bond force as the strength measurement, as opposed to bond stress. Reasoning, that the bond stress varies over the bonded length, whilst the bond strength is a structural response rather than a material property. Therefore, bond strength provides a more accurate measure.

$$\frac{A_b f_s}{\sqrt{f_c'}} = 10 l_d (C + 0.5 d_b)$$

Eq. 6-2: Bond model by Darwin et al. (1992)

Esfahani and Rangan 1998

Esfahani and Rangan (1998) develop analytical equations for low and high strength concrete for short length specimens based on Tepfers (1973) cracked thick cylinder theory. Tepfers theory assumes that surrounding the cracked concrete enveloping the rebar, an uncracked concrete ring is acting as confinement resisting the outward stresses. Esfahani and Rangan (1998) modified this theory to account for plastic deformation of the tensile concrete in the cracked and uncracked rings of the concrete cylinder.

$$u_c = 4.9\frac{C/d_b + 0.5}{C/d_b + 3.6} f_{ct}\,;\;\; f_{cd} < 50\ MPa$$

Eq. 6-3: Bond model by Esfahani and Rangan (1998) (low strength concrete)

$$u_c = 8.6\frac{C/d_b + 0.5}{C/d_b + 5.5} f_{ct}\,;\;\; f_{cd} = 50 - 75\ MPa$$

Eq. 6-4: Bond model by Esfahani and Rangan (1998)

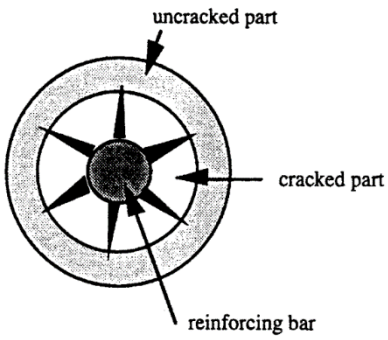

Figure 6-2:(Esfahani & Rangan, 1998)

Hadi

With the use of high strength concrete becoming more common. Whereas, the previous bond models for mainly developed for concrete strength less than 50 MPa. Hadi (2008) proposed a new empirical model similar to Orangun model aimed specifically for high strength concrete.

$$\frac{u^*}{\sqrt{f_c'}} = 0.083045\left[22.8 - 0.208\frac{C}{d_b} - 38.212\frac{d_b}{l_s}\right]$$

Eq. 6-5: Bond model by Hadi (2008)

6.2 Bond behaviour prediction model

Harajli et al. (1995) set out to develop an analytical model for the bond stress-slip response based on experimental research. The model considers the different failure modes for bond behaviour; pull-out failure and splitting failure (confined and unconfined). Each of these bond stress-slip models is characterized by four stages. These are explained in the following segment, and is depicted in Figure 6-3.

Pull-out

Reinforced concrete specimens failing in pull-out mode. (Harajli et al.) defines the following relations. The initial ascending branch of the pull-out curve is defined by Eq. 6-6. Where u_m represents the maximum bond stress, corresponding to the concrete compressive strength. And s denotes the slip of the rebar.

$$u = u_m(s/s_1)^{0.3}$$ *Eq. 6-6: Pull-out mode (ascending branch)*

$$u_m = 2.57\sqrt{f_c'}$$ *Eq. 6-7: Pull-out mode (plateau)*

The amount of slip (S_{max}) where the maximum bond strength u_m occurs does not correlate to concrete strength fc' nor confinement. It depends mainly on the clear distance (c_0) between the lugs of the reinforcing bars (Harajli et al. (1995), Eligehausen). This distance between the lugs is dependent on the rebar diameter $c_0 = 0.5 - 0.7d_b$. If This information is not provided may use the distances provided in *Eq. 6-8* to *Eq. 6-10*.

$$s_1 = 0.15c_0 \; or \; 1.5\,mm$$ *Eq. 6-8: Pull-out mode (slip at max strength)*

$$s_2 = 0.35c_0 \; or \; 3.5\,mm$$ *Eq. 6-9: Pull-out mode (slip at end max strength)*

$$s_3 = c_0 \; or \; 10\,mm$$ *Eq. 6-10: Pull-out mode (slip at friction strength)*

After reaching the maximum bond strength u_m, a linear decrease till reaching the final resistance u_f.

$$u_f = 0.35u_m$$ *Eq. 6-11: Pull-out mode (frictional resistance)*

Splitting

The first stage before splitting failure, for both unconfined or confined concrete follows the pull-out mode envelope up to αu_{sp} (where $\alpha = 0.7$). At the onset of microcracking, induced by the concrete wedging as explained in Chapter 3. The stiffness reduces and the bond resistance increases linearly up to u_{sp} in the following segment. The bond stress is u_{sp}, *Eq. 6-12*. K_c is a confinement parameter. In present research no confinement is used, therefore $K_c = 0$.

$$u_{sp} = \gamma\sqrt{f_c'}\left(\frac{c+K_c}{d_b}\right)^{2/3} \leq u_m$$

Eq. 6-12: Splitting mode (ascending branch)

The slip corresponding to the maximum splitting bond strength u_{sp}, see *Eq. 6-13*. At this moment the bond resistance will decrease rapidly.

$$S_{sp} = s_1 e^{3.3\ln(u_{sp}/u_m)} + s_0 \ln\left(\frac{u_m}{u_{sp}}\right)$$

Eq. 6-13: Splitting mode (slip at u_{sp})

Where $s_0 = 0.15$ for unconfined concrete $s_0 = 0.4$ for steel confined concrete, $s_0 = 0.2$ FRP confined concrete.

The finale segment of the splitting failure mode depends is contingent upon whether the concrete is confined. If the concrete is confined, a more progressive decrease in bond resistance will occur.

Unconfined concrete the descending segment expression:

$$u = \frac{\beta u_{sp}}{\sqrt{s/s_{sp}}}$$

Eq. 6-14: Splitting mode unconfined concrete (descending branch)

Confined concrete;

$$u_p = u_{sp}(0.5 + K_{cs});\ \beta u_{sp} \leq u_p \leq u_{sp}$$

Eq. 6-15: Splitting mode confined concrete (descending branch)

Table 6-1: Harajli bond model equations

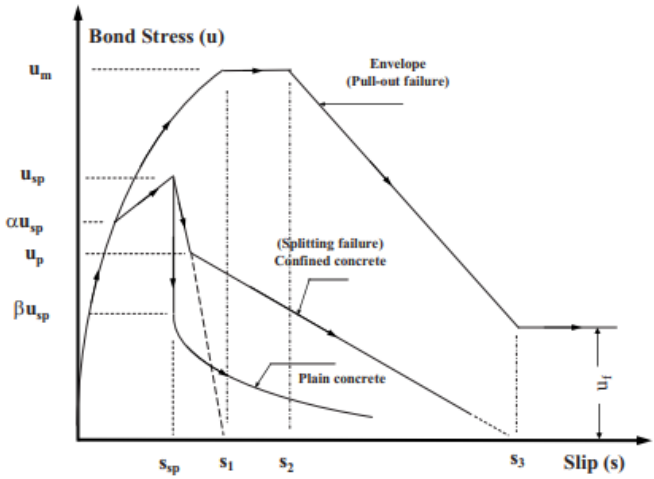

Figure 6-3: Bond behaviour model Harajli et al. (1995)

Parameters Harajli model	
$\alpha = 0.7 \;\; \beta = 0.65 \;\; \gamma = 0.78$	
Slip at each stage	
Monotonic Pullout Envelope	$s_1 = 0.15c_0 \; or \; 1.5$ $s_2 = 0.35c_0 \; or \; 3.5$ $s_3 = c_0 \; or \; 10$
Splitting failure normal concrete	$S_{sp} = s_1 e^{3.3\ln(u_{sp}/u_m)} + s_0 \ln\left(\frac{u_m}{u_{sp}}\right)$
Bond strength	
Monotonic Pullout Envelope	$u = 2.57\sqrt{f_c'}(s/s_1)^{0.3}$ $u_f = 0.35u_m$
Splitting failure	$u_{sp} = \gamma\sqrt{f_c'}\left(\frac{c+K_c}{d_b}\right)^{2/3} \leq u_m$
Unconfined	$u = \frac{\beta u_{sp}}{\sqrt{s/s_{sp}}}$
Confined	$u_p = u_{sp}(0.5 + K_{cs}); \; \beta u_{sp} \leq u_p \leq u_{sp}$

6.3 Bond prediction Codes

ACI 318

The ACI 318 equation is derived from the OJB model. The code expresses the minimum development length needed.

$$\frac{l_d}{d_b} = 0.9\frac{f_y}{\sqrt{f_c'}\left(\frac{c+K_{tr}}{d_b}\right)}$$

Eq. 6-16: Development length ACI 318

Where K_{tr} accounts for transverse reinforcement. In present case, pull-out test is performed without transverse reinforcement. Therefore, this parameter is 0.

$$K_{tr} = \frac{A_{tr}f_{yt}}{10.34\,sn}$$

Eq. 6-17: Transverse reinforcement parameter ACI 318

The ACI 318 development length equation can be rewritten to the average bond stress U_{ACI}.

- Using the theoretical average bond stress u_b (Eq. 3-5)
- ACI assumes that the rebar stress f_s will achieve 125% of the yield stress $f_s = 1.25f_y$

$$U_{ACI} = 0.8\left(0.347\sqrt{f_c'}\frac{l_d}{d_b}\right)$$

Eq. 6-18: Bond stress derived from ACI 318 minimum development length

AS 3600 (2001)

The AS 3600 defines the minimum embedded length (Eq. 6-19).

$$l_d = \frac{k_1 k_2 f_y A_b}{(2c + d_b)\sqrt{f_c'}} > 25 k_1 d_b$$

Eq. 6-19: Minimum development length AS 3600 (2001)

Where:

- $k_1 = 1.25$ for a horizontal bar with more than 300 mm of concrete cast below, otherwise 1.0
- $k_2 = 1.7$ for bars in slabs and walls if the clear distance between adjacent parallel rebars developing stress is not less than 150 mm.

Similarly, this equation is rewritten using the theoretical average bond stress equation.

$$U_{AS} = \frac{(2c + d_b)\sqrt{f_c'}}{\pi k_1 k_2 d_b} \leq \frac{f_s}{100 k_1}$$

Eq. 6-20: Bond stress derived from AS 2001 minimum development length

EC2

Contrary to previous code standards the EC2 specifies a minimum bond strength. This bond strength is based on the tensile strength of the concrete.

$$f_{bd} = 2.25 \eta_1 \eta_2 f_{ctd}$$

Eq. 6-21: Minimum bond stress EC2

Where:

- f_{ctd} is the concrete tensile strength design value.
- η_1 is a parameter which takes in to account the bond quality
  - $\eta_1 = 1$ good bond quality
  - $\eta_1 = 0.7$ otherwise
- η_2 regarding the rebar diameter
  - $\eta_2 = 1.0\ for\ \emptyset < 32mm$
  - $\eta_2 = \frac{132-\emptyset}{100}\ for\ \emptyset > 32mm$

6.4 Comparison model to test results

Analytical Models

The bond strength was evaluated against various CC semi-empirical models. Figure 6-4 displays the maximum bond strength values for all pull-out tests conducted in the current investigation on steel-reinforced specimens. The parameter age is represented by the marker's form, while the curing condition is indicated by the hue of the marker. The concrete type is expressed by the marker size. The subsequent bond models take into account essential variables: compressive strength, concrete cover, and bond length. This study utilised two sizes of concrete cubes. Consequently, the concrete cover will vary between 46 mm and 71 mm. The OJB model was based on empirical tests with a concrete cover to rebar ratio $c_c/d_b < 2.5$. Consequently, Orangun advises employing $c_c/d_b = 2.5$ when this ratio exceeds 2.5. Since both concrete sizes have a c_c/d_b greater than 2.5, this ratio is considered to be 2.5 in both instances. As a result, the varying concrete sizes do not influence the projected outcomes and are applicable to both sizes.

The results are relatively conservatives. Only test findings consistent with these models relate to AASC subjected to drying. These specimens exhibited significantly reduced bond strength relative to the standard cured specimens. In order to comprehend these results, it is essential to examine how these models were developed. All these models were developed based on regression analysis of lap-spliced beam tests. This distinction is significant when comparing current pull-out test results. Lap spliced beam test resemble real bond scenarios more closely. Where the surrounding concrete matrix is in tension, this is opposed to pull-out tests where the surrounding concrete matrix is in compression. Consequently, the maximum bond strength achieved in these experiments is generally inferior to that of the pull-out test. This distinction is evident in the ensuing models produced. The OJB paper indicated that the primary failure mode in its dataset, upon which its model is founded, is splitting failure. The predominance of this failure mode is partly attributable to the experimental setup, wherein the surrounding concrete is subjected to tension. This contrasts with the principal failure mechanism of the current experiment, which is pull-out failure.

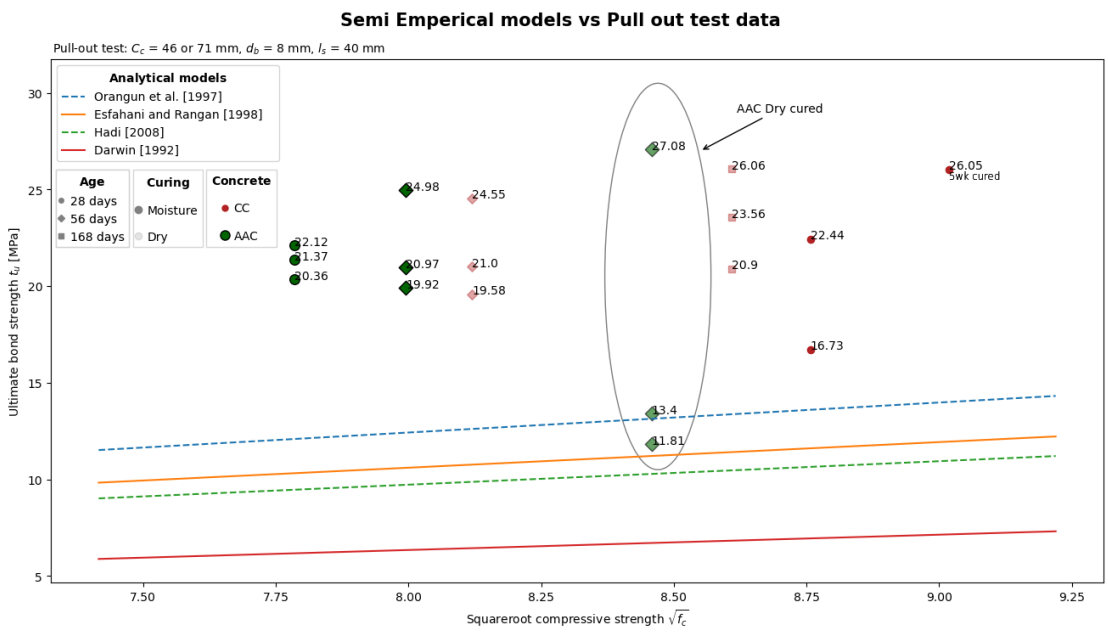

Figure 6-4: Semi-empirical models vs experimental results

Comparison results to literature

Figure 6-5 presents the maximum bond strength obtained in this study for CC and AASC concrete (indicated by green and red dots, respectively). These results are compared with bond strength findings from other research, primarily from 28-day pull-out or beam-end tests, while the present study involved longer-term bond testing. The comparison encompasses various types of AAC, considering factors such as composition, reinforcement diameter, concrete cover, and curing conditions. The aim is to provide a broader context for interpreting the present results within the scope of AAC bond strength. Beam-end tests generally produce lower ultimate bond strengths compared to pull-out tests. The beam-end results of Sofi (2007) which align more closely to the analytical models. Reflect the nature of the analytical models, as these models were derived from spliced beam test. Whereas current study and remaining literature pull-out test results tend to exceed the predicted bond strength from these models.

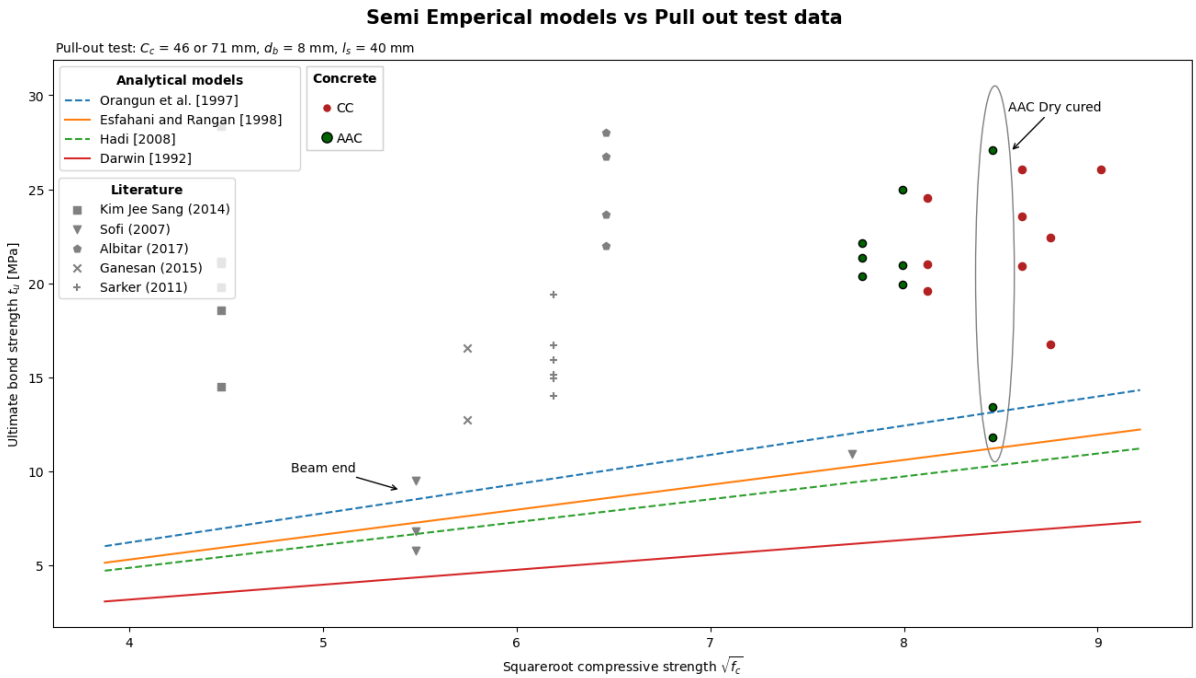

Figure 6-5: Pull out test results compared to literature results

Code standards

The maximum bond strength results were evaluated against various code standards: ACI 318, AS 01, and EC2. The bond strength values from the experimental test are divided by the minimum needed bond strength as per the various standards U_{test}/U_{code}. This ratio is depicted graphically; values exceeding the red line ratio of 1 are deemed safe, while values falling below the red line are classified as unsafe.

The most conservative standard is EC2, succeeded by ACI 318 and AS 01. An examination of the results reveals that the two AAS specimens subjected to drying, which exhibited a lesser than anticipated bond strength, do not conform to ACI 318 or AS 01 standards. Moreover, a CC standard cured pull-out test fails to comply with AS 01. This result is deemed an outlier as it was obtained under excellent moisture curing conditions.

Furthermore, it is important to acknowledge the similarities between OJB and ACI 318 outcomes are evident, as ACI is based on the OJB model.

It follows that the results indicate that the AAS specimens subjected to drying may lead to an unsafe design according to ACI 318 and AS 01 code requirements.

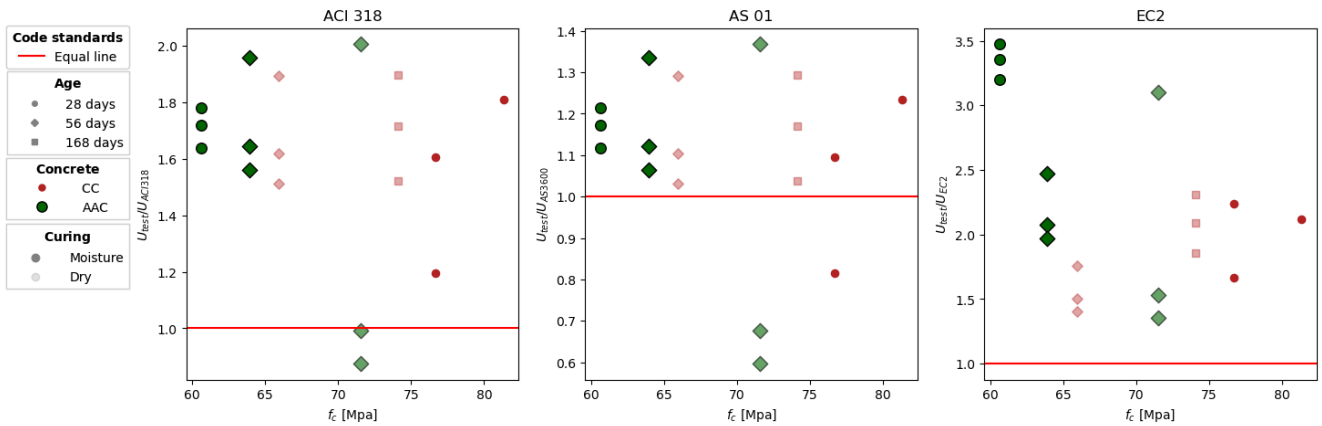

Figure 6-6: Experimental pull-out test results compared to various code standards: ACI 318, AS 01 and EC2

Harajli bond behaviour model

The bond behaviour model proposed by Harajli is superimposed on the findings of the pull-out test conducted. The Harajli model requires input parameters including compressive strength, concrete cover, and rebar diameter. The compressive strength of concrete fluctuates with time; hence, an average compressive strength of 73 MPa is estimated CC and 65 MPa for AAS. All CC examples are 100 mm cubes; hence, the concrete cover c_c measures 46 mm. All AAS specimens measure 150 mm in size, with a c_c of 71 mm. These characteristics, along with the rebar diameter, serve as inputs for the Harajli model. The subsequent graphic illustrates the Harajli model for pull-out failure (thick red line) and splitting failure (thick blue line).

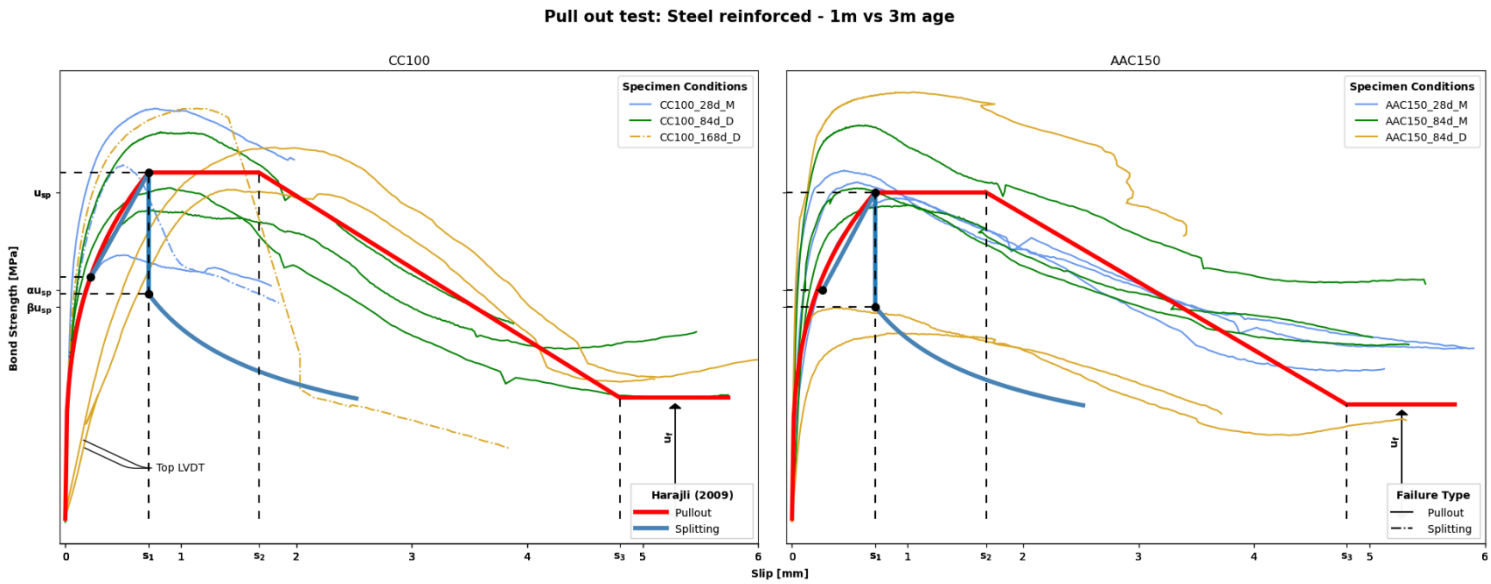

Figure 6-7: Harajli bond behaviour model CC and AAS

The CC specimens pull-out test behaviour does correspond quite well with the Harajli model regardless of the curing condition or age. Same can't be said for the AAS specimens. The initial 28d standard cured and continued moisture cured do resemble the model. However, the AAS specimens exposed to dry conditions have significant lower bond strength and don't match the model.

7. Conclusion

The main objective of this study was to evaluate the time-dependent bond behaviour of slag-activated concrete (AAS) under various curing conditions. Specifically, it aims to determine the extent to which drying, following 28 days of moisture curing, affects the bond behaviour of AAS and whether this impact is consistent with the changes in the material properties observed in previous studies.

The research in the present study comprised a series of pull-out tests on steel and prestressed strands reinforced self-compacting AAS cubes (AASC). The AASC mixture was developed by TU Delft. This mixture, as well as several other studies on AAS, reported a decrease in material properties over time when subjected to drying. This phenomenon is not observed in conventional concrete. Consequently, it raises concerns regarding the applicability of AAS in structural elements. The bond behaviour is crucial for structural integrity. Initial preliminary test aimed to establish a proper test procedure, before proceeding with the main experiment on the bond behaviour. Finally, the applicability of existing analytical bond models for conventional concrete are used to compare and evaluate the results.

Q1: What is the optimal method for conducting a pull-out test?
Preliminary test series were conducted to determine the optimal testing procedure, test setup and best configuration to perform the pull-out test. The main consideration regarding the test procedure is the displacement speed and the application of confinement. A variable displacement-controlled load rate was preferred. Prior to each pull-out test the concrete cubes are confined, by prestressing the top plate. With the aim of enabling pull-out failure mode. The confinement mitigates the radial tensile stresses generated by the wedging action of the rebar. Consequently, facilitating pull-out failure mode. Excessive confinement may produce the contrary effect, leading to a splitting failure mode. To ensure effective confinement, the setup procedure requires careful evaluation. An error occurred by securing the rebar to the jack prior to applying confinement. This sequence inadvertently resulted in the rebar being pulled out before the test could commence, leading to a failed experiment. Moreover, it is essential to ensure that the top plate remains straight during the prestressing of the top plate. Top plate bending as a consequence of the prestressing will induce tensile stresses, contrary to the desired effect, leading to a splitting failure mechanism. It was ultimately determined that a prestress of approximately 60-80 Nm is adequate to ensure the integrity of the specimens.

This study investigated the influence of the rebar profile configuration on the failure mode. The main distinction is the presence of a top unbonded concrete layer preceding the bonded segment. However, the configurations were not evaluated using a consistent methodology, preventing the establishment of definitive conclusions regarding the optimal configuration. Configuration 3, comprising an upper and lower unbonded embedded reinforcement section with a bonded portion centrally located, was selected based on the following criteria; The ability to measure the rebar slip from the free end. The top unbonded section will provide the necessary concrete mass to resist tensile stresses caused by wedging. Preliminary test with appropriate confinement levels proved that pull-out failure could be attained in specimens including a top unbonded region. Suggesting that the unbonded concrete mass does enable pull-out failure mode.

Q2: How does the bond behaviour for conventional and prestressing strand reinforced concrete develop over time under different curing conditions?

All specimens underwent conventional moisture curing for 28 days. Subsequently, some were exposed to drying for up to 168 days, while others were maintained in moist conditions. The pull-out test was conducted on specimens at 28 days (moisture cured), 84 days (moisture and dry cured), and 168 days (dry cured CC). In addition to the pull-out test, compressive and tensile splitting tests were conducted on each test group.

The material test results indicated that prolonged moisture curing in AAS increased compressive strength. AAS specimens exposed to dry conditions also demonstrated improved compressive strength. Larger AAS specimens showed greater strength gains due to eigenstress effects, aligning closely with findings reported by Zhang et al. (2022). However, CC showed a decrease in compressive strength over time under dry conditions, which could not be explained in the current study.

For tensile splitting strength, an increase was observed in all samples over 84 days, though the 150 mm AAS specimens exhibited significant variability, diverging partially from Zhang et al. (2022). After 84 days, tensile strength decreased in both dry-cured CC and AAS, likely due to reduced eigenstress effects, with CC specimens consistently exhibiting higher tensile strength than AAS.

The results show that the bond strength of CC specimens remains stable under dry conditions, potentially even increasing slightly over time. This outcome aligns with general expected CC material behaviour. Overall, the stability of CC bond strength under dry conditions is consistent with its predictable material performance.

At first glance, a noticeable decrease in bond strength was observed in the steel reinforced AAS specimens exposed to drying. However, a closer look reveals a large standard deviation in the results, with two out of three specimens showing significantly lower bond strength, suggesting some effect of drying. Closer inspection of DIC, DFOS or execution did not reveal any discernible differences. Therefore, the effect of drying on the bond behaviour remains inconclusive, as single specimen exhibited exceptionally high bond strength.

This research aims to determine if AAS bond strength is affected by reduced material properties. Material property test have shown compressive strength increase as well as slight tensile splitting strength increase over the testing period. This indicates that the decrease in bond strength of steel reinforced specimens is not directly associated with the development of compressive or tensile strength, partially answering the research issue.

A notable material property of AAS is the considerable autogenous shrinkage when compared to CC. This has been shown to induce micro-cracks in the concrete. Most of the autogenous shrinkage occurs in the first three weeks of curing, when the concrete is under optimal moisture curing conditions. Considering, that no clear bond strength differences is observed in the first 28-days between CC and AAS it can be concluded that the large autogenous shrinkage does not affect the bond behaviour in steel reinforced concrete.

However, under dry conditions the ensuing drying shrinkage can induce further micro-crack development in the concrete (Collins & Sanjayan, 2001), potentially explaining the observed decrease in bond strength for steel specimens in dry conditions. Visual evidence supports this, as significant drying shrinkage cracks were detected using DIC. Thus, microcracks from drying shrinkage likely influenced the bond strength results. However, this remains inconclusive, as not all dry-cured specimens exhibited a decrease in bond strength attributable to drying shrinkage microcracks.

In prestressed reinforced specimens, the results indicate that CC demonstrates superior bond strength compared to AAS, primarily due to the higher tensile splitting strength of the concrete surrounding the prestressed strands in CC. However, this difference in bond strength was not observed in steel-reinforced specimens, which showed similar bond strengths despite CC's greater tensile splitting strength. This discrepancy can be attributed to differences in failure modes. Prestressed reinforced specimens failed by splitting failure, where the concrete's tensile strength was the dominant factor. In contrast, steel-reinforced specimens failed by pull-out, a failure mode in which the concrete's tensile strength does not play a significant role and is therefore not reflected in the bond strength results. The reduced bond strength in prestressed AAS can be attributed to the geometry of the reinforcement and differing bond transfer mechanisms, as prestressed strands rely more on friction due to their smoother surfaces, while ribbed rebars primarily utilize bearing resistance. Consequently, the lower tensile splitting strength in AAS likely contributes to the decreased bond strength in the prestressed specimens, whereas CC's higher tensile strength helps maintain the integrity of the concrete matrix, enhancing bond performance.

Additionally, no drying effects were observed in prestressed reinforced concrete, as the development of micro-cracks did not negatively impact bond strength, unlike in steel-reinforced specimens. This difference can be attributed to the distinct bond transfer mechanisms. In steel-reinforced concrete, the wedging action of the rebar is more likely to propagate micro-cracks, which may explain the observed effects of drying. In contrast, the geometry of prestressed reinforced concrete seems to mitigate this issue.

Internal strain measurements were conducted using Distributed Fiber Optic Sensing (DFOS) sensors to gain deeper insights into the internal bond behaviour. In some instances, the internal strain readings aligned well with the theoretical strain derived from the external strength obtained in pull-out tests, especially in the top unbonded layer just before the bonded segment. This suggests that DFOS is capable of accurately capturing the internal distribution of bond stress. However, significant inconsistencies were noted, particularly with high peak strain values at the boundaries of the bonded segment, which adversely impacted the strain measurements in that area. These discrepancies likely resulted from disturbances related to the installation of pipe covers on the rebar in the unbonded sections. While DFOS shows promise for assessing bond behaviour, these boundary effects highlight the need for further refinement of the setup to improve measurement accuracy and consistency.

Q3: What is the applicability of existing bond models for conventional concrete on to AAS considering the time dependency?

The necessity to estimate the bond strength is crucial for the safety and structural integrity of concrete structures. To this end the pull-out results were compared to various semi-empirical models and code standards. The semi-empirical model proved to be fairly conservative against bond strength results attained in current study. Even the lesser bond strength attained from dry exposed AAS specimens. While the tests in this study were conducted up to 86 days, it is important to consider that concrete structures are expected to last for at least 50 years. Based on existing literature, drying shrinkage typically stabilizes within the first 3 months of age, and therefore, it is unlikely that the bond strength will significantly worsen over a longer time frame. Microcrack development due to drying shrinkage would have already stabilized, so it is not expected that bond strength will continue to deteriorate significantly. Further testing at later ages is recommended to confirm this stabilization and to provide more conclusive insights regarding the durability of bond strength over the lifespan of the structure. It should be noted that the lower bond strength predicted by these models is in part due to the nature of these modes. These semi-empirical models were derived from lap spliced

beams. Where the surrounding concrete matrix is in tension. Therefore, the attained bond strength is generally lower compare to bond strength attained from pull-out test. The code standards were mostly conservative. With EC2 being the most conservative, with all the bond strength results compliant. For the remaining code standards AS 01 and ACI 318, the reduced bond strength observed from AAS specimens exposed to drying fell below the minimum required bond strength. The bond behaviour model was also considered, to this end the pull-out test results were compared to the Harajli bond model. The CC concrete results were all in line with the Harajli model. The same could be said for the moisture-cured AAS specimens, with the exception of those subjected to drying. One of the key challenges impeding the structural application of AAC is the limited understanding of its structural behaviour, particularly how changes in material properties influence its performance. This study aimed to determine whether the observed decrease in material properties, especially due to drying, impacts the bond behaviour of AAC. Since bond behaviour is critical for the structural integrity of reinforced concrete, the findings from this research suggest that drying effects, specifically drying shrinkage, impact the bond behaviour of AAC. The microcracks as results weaken the bond strength. Therefore, it can be concluded that the observed decrease in bond strength due to drying effects of AAC may result in unsafe design.

Recommendations and future work

In future work, a further investigation into the effects of drying on bond behaviour in AAS is necessary. Although bond strength has been shown to correlate with compressive and tensile strength, the results from AAS specimens exposed to drying contradict this trend. No significant loss in compressive or tensile strength was observed in these specimens, yet they experienced a notable reduction in bond strength. This suggests that drying, particularly the shrinkage effects, plays a more complex role in bond behaviour than previously understood. A comprehensive study focused on the impact of drying shrinkage on bond strength is essential to clarify this relationship.

A key aspect of this is the role of shrinkages, which has been shown to cause the formation of microcracks during curing. These microcracks likely influence bond performance, making it crucial to investigate their development in greater detail. Future research should focus on understanding the extent to which both autogenous and drying shrinkage contribute to microcrack formation, and how different levels of drying affect the severity of these cracks. Moreover, it is important to explore how the presence and progression of microcracks influence bond behaviour, particularly in terms of weakening the bond between the reinforcement and the concrete matrix.

Moreover, reproducibility remains an issue. While some drying effects on bond strength were observed, not all AAS specimens exposed to drying exhibited this reduction. In fact, one specimen showed unexpectedly high bond strength. This inconsistency indicates that the effect of drying on AAC and its mechanical properties is not yet fully understood, and further research is needed to conclusively determine whether these changes affect bond strength uniformly.

Finally, the limited timeframe of the current study—84 days—leaves questions about the long-term effects of drying unaddressed. It remains unclear whether the reduction in bond strength would continue, stabilize, or worsen over a longer period. Future studies should investigate the long-term development of bond strength under drying. This would help to determine if the reduction in bond strength exacerbates over time or plateaus, providing more comprehensive data on the durability and performance of AAS in dry environments.

Future studies should focus on understanding how the development and propagation of microcracks due to drying evolves over time and how this affects bond strength in the long run. Clarifying the relationship between drying-induced microcracking and bond behaviour is crucial for predicting the

material's long-term performance and durability in structural applications. By investigating whether microcracking increases with extended drying periods or stabilizes, we can better assess the safety and reliability of AAC in real-world applications.

References

Abdulrahman, H., Muhamad, R., Shukri, A. A., Al-Fakih, A., Alqaifi, G., Mutafi, A., Al-Duais, H., & Al-Sabaeei, A. (2023). Tension Stiffening and Cracking Behavior of Axially Loaded Alkali-Activated Concrete. *Materials*, *16*, 4120. https://doi.org/10.3390/ma16114120

Abdulrahman, H., Muhamad, R., Visintin, P., & Azim Shukri, A. (2022). Mechanical properties and bond stress-slip behaviour of fly ash geopolymer concrete [Article]. *Construction and Building Materials*, *327*, Article 126909. https://doi.org/10.1016/j.conbuildmat.2022.126909

Albidah, A., Altheeb, A., Alrshoudi, F., Abadel, A., Abbas, H., & Al-Salloum, Y. (2020). Bond performance of GFRP and steel rebars embedded in metakaolin based geopolymer concrete [Article]. *Structures*, *27*, 1582-1593. https://doi.org/10.1016/j.istruc.2020.07.048

Albitar, M., Mohamed Ali, M. S., & Visintin, P. (2018). Evaluation of tension-stiffening, crack spacing and crack width of geopolymer concretes. *Construction and Building Materials*, *160*, 408-414. https://doi.org/https://doi.org/10.1016/j.conbuildmat.2017.11.085

Albitar, M., Visintin, P., Mohamed Ali, M. S., Lavigne, O., & Gamboa, E. (2017). Bond slip models for uncorroded and corroded steel reinforcement in class-F fly ash geopolymer concrete [Article]. *Journal of Materials in Civil Engineering*, *29*(1), Article 04016186. https://doi.org/10.1061/(ASCE)MT.1943-5533.0001713

Allen, J. H., Felder, A. L., McDermott, J. F., Azizinamini, A., Frosch, R. J., Mitchell, D., Balazs, G. L., Hamad, B. S., Pantazopoulou, S. J., & Browning, J. (2003). Bond and Development of Straight Reinforcing Bars in Tension. *ACI 408R-03*.

Allwood, J. M., Cullen, J. M., & Milford, R. L. (2010). Options for Achieving a 50% Cut in Industrial Carbon Emissions by 2050. *Environmental Science & Technology*, *44*(6), 1888-1894. https://doi.org/10.1021/es902909k

Almusallam, A. A., Al-Gahtani, A. S., Aziz, A. R., & Rasheeduzzafar. (1996). Effect of reinforcement corrosion on bond strength. *Construction and Building Materials*, *10*(2), 123-129. https://doi.org/https://doi.org/10.1016/0950-0618(95)00077-1

Anwar Hossain, K. M. (2008). Bond characteristics of plain and deformed bars in lightweight pumice concrete. *Construction and Building Materials*, *22*(7), 1491-1499. https://doi.org/https://doi.org/10.1016/j.conbuildmat.2007.03.025

Awasthy, N., Schlangen, E., Hordijk, D., Šavija, B., & Luković, M. (2023). The role of eigen-stresses on apparent strength and stiffness of normal, high strength, and ultra-high performance fibre reinforced concrete. *Developments in the Built Environment*, *16*, 100277. https://doi.org/https://doi.org/10.1016/j.dibe.2023.100277

Barrias, A., Casas, J. R., & Villalba, S. (2019). SHM of Reinforced Concrete Elements by Rayleigh Backscattering DOFS. *Frontiers in Built Environment*, *5*. https://doi.org/10.3389/fbuil.2019.00030

Bernal, S. A., Provis, J. L., Fernández-Jiménez, A., Krivenko, P. V., Kavalerova, E., Palacios, M., & Shi, C. (2014). Binder chemistry–high-calcium alkali-activated materials. *Alkali Activated Materials: State-of-the-Art Report, RILEM TC 224-AAM*, 59-91.

Bijleveld, M., & Beeftink, M. (2020). *Klimaatimpact van betongebruik in de Nederlandse bouw. Vergelijking 1990, 2010 en 2017*.

Bijleveld, M. M., Bergsma, G. C., & van Lieshout, M. (2013). *Mileu-impact van betongebruik in de Nederlandse bouw*.

Bischoff, P. H. (2001). Effects of shrinkage on tension stiffening and cracking in reinforced concrete. *Canadian Journal of Civil Engineering*, *28*(3), 363-374.

Boopalan, C., & Rajamane, N. P. (2017). An Investigation of Bond Strength of Reinforcing Bars in Fly Ash and GGBS Based Geopolymer Concrete. MATEC Web of Conferences,

Boopalan, C., Rajamane, N. P., & Jeyalakshmi, R. (2018, 2018). Studies on adhesive bond strength of steel reinforcing bars with fly ash based-ambient cured geopolymer concrete.

Bye, G. C., Livesey, P., & Struble, L. J. (2011). *Portland cement* (Third edition. ed.). Institution of Civil Engineers Publishing.

Castel, A. (2017). Bond Between Steel Reinforcement and Geopolymer Concrete. In *Handbook of Low Carbon Concrete* (pp. 375-387). https://doi.org/10.1016/B978-0-12-804524-4.00014-2

Castel, A., & Foster, S. J. (2015). Bond strength between blended slag and Class F fly ash geopolymer concrete with steel reinforcement. *Cement and Concrete Research*, *72*, 48-53. https://doi.org/https://doi.org/10.1016/j.cemconres.2015.02.016

Castel, A., Foster, S. J., Ng, T., Sanjayan, J. G., & Gilbert, R. I. (2016). Creep and drying shrinkage of a blended slag and low calcium fly ash geopolymer Concrete [Article]. *Materials and Structures/Materiaux et Constructions*, *49*(5), 1619-1628. https://doi.org/10.1617/s11527-015-0599-1

Collins, F., & Sanjayan, J. (2001). Microcracking and strength development of alkali activated slag concrete. *Cement and Concrete Composites*, *23*(4-5), 345.

Collins, F., & Sanjayan, J. G. (2000). Effect of pore size distribution on drying shrinking of alkali-activated slag concrete. *Cement and Concrete Research*, *30*(9), 1401-1406. https://doi.org/https://doi.org/10.1016/S0008-8846(00)00327-6

Croppi, J. I., Ahrens, M. A., Genesio, G., Piccinin, R., Casucci, D., & Mark, P. (2024). Bond stresses in post‐installed reinforcing bars derived via fiber optic sensors. *Structural Concrete*.

Cui, Y., Qu, S., Bao, J., & Zhang, P. (2022). Bond Performance of Steel Bar and Fly Ash-Based Geopolymer Concrete in Beam End Tests [Article]. *Polymers*, *14*(10), Article 2012. https://doi.org/10.3390/polym14102012

Cui, Y., Zhang, P., & Bao, J. (2020). Bond Stress between Steel-Reinforced Bars and Fly Ash-Based Geopolymer Concrete [Article]. *Advances in Materials Science and Engineering*, *2020*, Article 9812526. https://doi.org/10.1155/2020/9812526

Darwin, D., McCabe, S. L., Idun, E. K., & Schoenekase, S. P. (1992). Development length criteria: bars not confined by transverse reinforcement.

Davidovits, J. (1991). Geopolymers : Inorganic polymeric new materials. *Journal of thermal analysis*, *37*(8), 1633-1656. https://doi.org/10.1007/BF01912193

Davidovits, J. (2018). Why alkali-activated materials (AAM) are not geopolymers. *Publication Technical Paper*, *25*.

Dawood, N., & Marzouk, H. (2011). Experimental evaluation of the tension stiffening behavior of HSC thick panels. *Engineering Structures*, *33*(5), 1687-1697. https://doi.org/https://doi.org/10.1016/j.engstruct.2011.02.006

Esfahani, M. R., & Rangan, B. V. (1998). Local Bond Strength of Reinforcing Bars in Normal Strength and High-Strength Concrete (HSC). *ACI Structural Journal*, *95*(2). https://doi.org/10.14359/530

Farhan, N. A., Sheikh, M. N., & Hadi, M. N. S. (2018). Experimental Investigation on the Effect of Corrosion on the Bond Between Reinforcing Steel Bars and Fibre Reinforced Geopolymer Concrete [Article]. *Structures*, *14*, 251-261. https://doi.org/10.1016/j.istruc.2018.03.013

Ferguson, P. M. (1966). Bond Stress - State of the Art. *ACI Journal Proceedings*, *63*(11). https://doi.org/10.14359/7665

Fernandez-Jimenez, A., García-Lodeiro, I., & Palomo, A. (2007). Durability of alkali-activated fly ash cementitious materials. *Journal of Materials Science*, *42*(9), 3055-3065. https://doi.org/10.1007/s10853-006-0584-8

Fernández-Jiménez, A., Palomo, A., & Alonso, M. (2005). Alkali activation of fly ashes: mechanisms of reaction. Congress of Non-Traditional Cement and Concrete II,

Gagg, C. R. (2014). Cement and concrete as an engineering material: An historic appraisal and case study analysis. *Engineering Failure Analysis*, *40*, 114-140. https://doi.org/https://doi.org/10.1016/j.engfailanal.2014.02.004

Galkovski, T., Lemcherreq, Y., Mata-Falcón, J., & Kaufmann, W. (2021). Fundamental Studies on the Use of Distributed Fibre Optical Sensing on Concrete and Reinforcing Bars. *Sensors*, *21*(22), 7643. https://doi.org/10.3390/s21227643

Ganesan, N., Indira, P. V., & Santhakumar, A. (2014). Influence of steel fibres on tension stiffening and cracking of reinforced geopolymer concrete. *Magazine of Concrete Research*, *66*(6), 268-276. https://doi.org/10.1680/macr.13.00273

Ganesan, N., Indira, P. V., & Santhakumar, A. (2015). Bond behaviour of reinforcing bars embedded in steel fibre reinforced geopolymer concrete [Article]. *Magazine of Concrete Research*, *67*(1), 9-16. https://doi.org/10.1680/macr.14.00125

García-Lodeiro, I., Fernández-Jiménez, A., & Palomo, A. (2013). Variation in hybrid cements over time. Alkaline activation of fly ash–portland cement blends. *Cement and Concrete Research*, *52*, 112-122. https://doi.org/https://doi.org/10.1016/j.cemconres.2013.03.022

García-Lodeiro, I., Maltseva, O., Palomo, Á., & Fernández-Jiménez, A. (2012). Cimenturi hibride alcaline. Partea I: Fundamente*/hybrid alkaline cements. Part I: Fundamentals. *Revista Romana de Materiale*, *42*(4), 330.

Garcia-Lodeiro, I., Palomo, A., & Fernández-Jiménez, A. (2015a). Crucial insights on the mix design of alkali-activated cement-based binders. In *Handbook of alkali-activated cements, mortars and concretes* (pp. 49-73). Elsevier.

Garcia-Lodeiro, I., Palomo, A., & Fernández-Jiménez, A. (2015b). An overview of the chemistry of alkali-activated cement-based binders. *Handbook of alkali-activated cements, mortars and concretes*, 19-47.

Garcia-Lodeiro, I., Palomo, A., Fernández-Jiménez, A., & Macphee, D. E. (2011). Compatibility studies between N-A-S-H and C-A-S-H gels. Study in the ternary diagram Na2O–CaO–Al2O3–SiO2–H2O. *Cement and Concrete Research*, *41*(9), 923-931. https://doi.org/https://doi.org/10.1016/j.cemconres.2011.05.006

Glukhovsky, V. D. (1994). Ancient, modern and future concretes. Proceedings of the First International Conference on Alkaline Cements and Concretes,

Habert, G., d'Espinose de Lacaillerie, J. B., & Roussel, N. (2011). An environmental evaluation of geopolymer based concrete production: reviewing current research trends. *Journal of Cleaner Production*, *19*(11), 1229-1238. https://doi.org/https://doi.org/10.1016/j.jclepro.2011.03.012

Hadi, M. N. S. (2008). Bond of High Strength Concrete with High Strength Reinforcing Steel~!2008-07-24~!2008-10-28~!2008-11-26~! *The Open Civil Engineering Journal*, *2*(1), 143-147. https://doi.org/10.2174/1874149500802010143

Harajli, M. H., Hout, M., & Jalkh, W. (1995). Local Bond Stress-Slip Behavior of Reinforcing Bars Embedded in Plain and Fiber Concrete. *ACI Materials Journal*, *92*(4). https://doi.org/10.14359/999

Hardjito, D., Wallah, S. E., Sumajouw, D. M. J., & Rangan, B. V. (2004). On the development of fly ash-based geopolymer concrete. *ACI Materials Journal*, *101*(6), 467-472.

Humad, A. M., Provis, J. L., Habermehl-Cwirzen, K., Rajczakowska, M., & Cwirzen, A. (2021). Creep and Long-Term Properties of Alkali-Activated Swedish-Slag Concrete [Article]. *Journal of Materials in Civil Engineering*, *33*(2), Article 04020475. https://doi.org/10.1061/(ASCE)MT.1943-5533.0003381

Hyatt, T. (1877). *An Account of Some Experiments with Portland-cement-concrete Combined with Iron: As a Building Material, with Reference to Economy of Metal in Construction, and for Security Against Fire in the Making of Roofs, Floors, and Walking Surfaces*. private circulation, at the Chiswick Press.

IEA. (2018). *Technology Roadmap - Low-Carbon Transition in the Cement Industry* World Business Council for Sustainable Development (WBCSD, Paris. https://www.iea.org/reports/technology-roadmap-low-carbon-transition-in-the-cement-industry

Kajaste, R., & Hurme, M. (2016). Cement industry greenhouse gas emissions – management options and abatement cost. *Journal of Cleaner Production*, *112*, 4041-4052. https://doi.org/https://doi.org/10.1016/j.jclepro.2015.07.055

Kathirvel, P., Thangavelu, M., Gopalan, R., & Kaliyaperumal, S. R. M. (2017). Bond characteristics of reinforcing steel embedded in geopolymer concrete. IOP Conference Series: Earth and Environmental Science,

Khalfallah, S., & Guerdouh, D. (2014). Tension stiffening approach in concrete of tensioned members. *International Journal of Advanced Structural Engineering*, *6*(1), 1-6. https://doi.org/10.1007/s40091-014-0051-8

Kim, J. S., & Park, J. H. (2014). An experimental evaluation of development length of reinforcements embedded ingeopolymer concrete. Applied Mechanics and Materials,

Kovalchuk, G., Fernández-Jiménez, A., & Palomo, A. (2007). Alkali-activated fly ash: Effect of thermal curing conditions on mechanical and microstructural development – Part II. *Fuel*, *86*(3), 315-322. https://doi.org/https://doi.org/10.1016/j.fuel.2006.07.010

Kuhl, H. (1908). *Slag Cement and Process of Making the Same* (US Patent No. 900,939).

Kumar, B. S. C., Ramesh, K., & Poluraju, P. (2017). An experimental investigation on flexural behavior of GGBS and metakaolin based geopolymer concrete. *ARPN journal of engineering and applied sciences*, *12*(7), 2052-2062.

Lee, G.-Y., & Kim, W. (2009). Cracking and tension stiffening behavior of high-strength concrete tension members subjected to axial load. *Advances in Structural Engineering*, *12*(2), 127-137.

Leung, W., & Ho, K. (1996). *Report on Strength Comparison of 100 Mm and 150 Mm Cubes*. Geotechnical Engineering Office, Civil Engineering Department.

Li, S., Sha, F., Liu, R., Li, W., Li, Z., & Wang, G. (2017). Properties of Cement-Based Grouts with High Amounts of Ground Granulated Blast-Furnace Slag and Fly Ash. *Journal of Materials in Civil Engineering*, *29*(11), 04017219. https://doi.org/10.1061/(asce)mt.1943-5533.0002083

Li, Z., Delsaute, B., Lu, T., Kostiuchenko, A., Staquet, S., & Ye, G. (2021). A comparative study on the mechanical properties, autogenous shrinkage and cracking proneness of alkali-activated concrete and ordinary Portland cement concrete. *Construction and Building Materials*, *292*, 123418. https://doi.org/https://doi.org/10.1016/j.conbuildmat.2021.123418

Li, Z., Lu, T., Liang, X., Dong, H., & Ye, G. (2020). Mechanisms of autogenous shrinkage of alkali-activated slag and fly ash pastes [Article]. *Cement and Concrete Research*, *135*, Article 106107. https://doi.org/10.1016/j.cemconres.2020.106107

Li, Z., Nedeljkovic, M., Zuo, Y., & Ye, G. (2018). Autogenous shrinkage of alkali-activated slagfly ash pastes. 5th International Slag Valorisation Symposium,

Li, Z., Zhang, S., Liang, X., & Ye, G. (2020). Cracking potential of alkali-activated slag and fly ash concrete subjected to restrained autogenous shrinkage. *Cement and Concrete Composites*, *114*, 103767. https://doi.org/https://doi.org/10.1016/j.cemconcomp.2020.103767

Luan, C., Wang, Q., Yang, F., Zhang, K., Utashev, N., Dai, J., & Shi, X. (2021). Practical prediction models of tensile strength and reinforcement-concrete bond strength of low-calcium fly ash geopolymer concrete. *Polymers*, *13*(6), 875.

Lura, P. (2003). Autogenous deformation and internal curing of concrete.

Lutz, L. A., & Gergely, P. (1967). Mechanics of Bond and Slip of Deformed Bars in Concrete. *ACI Journal Proceedings*, *64*(11). https://doi.org/10.14359/7600

Ma, C.-K., Awang, A. Z., & Omar, W. (2018). Structural and material performance of geopolymer concrete: A review. *Construction and Building Materials*, *186*, 90-102. https://doi.org/https://doi.org/10.1016/j.conbuildmat.2018.07.111

Ma, Z., Yue, Q., & Chen, Z. (2023). A Beam Test Study on the Bond Performance between Epoxy-Coated Reinforcement and Geopolymer Concrete [Article]. *Buildings*, *13*(2), Article 430. https://doi.org/10.3390/buildings13020430

MacGregor, J. G., Wight, J. K., Teng, S., & Irawan, P. (1997). *Reinforced concrete: Mechanics and design* (Vol. 3). Prentice Hall Upper Saddle River, NJ.

Maranan, G., Manalo, A., Karunasena, K., & Benmokrane, B. (2015). Bond stress-slip behavior: Case of GFRP bars in geopolymer concrete [Article]. *Journal of Materials in Civil Engineering*, *27*(1), Article 04014116. https://doi.org/10.1061/(ASCE)MT.1943-5533.0001046

Matthes, W., Vollpracht, A., Villagrán, Y., Kamali-Bernard, S., Hooton, D., Gruyaert, E., Soutsos, M., & De Belie, N. (2018). Ground granulated blast-furnace slag. *Properties of Fresh and Hardened Concrete Containing Supplementary Cementitious Materials: State-of-the-Art Report of the RILEM Technical Committee 238-SCM, Working Group 4*, 1-53.

McLellan, B. C., Williams, R. P., Lay, J., van Riessen, A., & Corder, G. D. (2011). Costs and carbon emissions for geopolymer pastes in comparison to ordinary portland cement. *Journal of Cleaner Production*, *19*(9), 1080-1090. https://doi.org/https://doi.org/10.1016/j.jclepro.2011.02.010

Melo Neto, A. A., Cincotto, M. A., & Repette, W. (2008). Drying and autogenous shrinkage of pastes and mortars with activated slag cement. *Cement and Concrete Research*, *38*(4), 565-574. https://doi.org/https://doi.org/10.1016/j.cemconres.2007.11.002

Menzel, C. A. (1939). Some Factors Influencing Results Of Pull-Out Bond Tests. *ACI Journal Proceedings*, *35*(6). https://doi.org/10.14359/8507

Mo, K. H., Yeap, K. W., Alengaram, U. J., Jumaat, M. Z., & Bashar, I. I. (2018). Bond strength evaluation of palm oil fuel ash-based geopolymer normal weight and lightweight concretes with steel reinforcement [Article]. *Journal of Adhesion Science and Technology*, *32*(1), 19-35. https://doi.org/10.1080/01694243.2017.1336195

Nath, P., & Sarker, P. K. (2014). Effect of GGBFS on setting, workability and early strength properties of fly ash geopolymer concrete cured in ambient condition. *Construction and Building Materials*, *66*, 163-171. https://doi.org/10.1016/j.conbuildmat.2014.05.080

Nath, P., & Sarker, P. K. (2017). Flexural strength and elastic modulus of ambient-cured blended low-calcium fly ash geopolymer concrete. *Construction and Building Materials*, *130*, 22-31. https://doi.org/https://doi.org/10.1016/j.conbuildmat.2016.11.034

Nguyen, K. T., Ahn, N., Le, T. A., & Lee, K. (2016). Theoretical and experimental study on mechanical properties and flexural strength of fly ash-geopolymer concrete. *Construction and Building Materials*, *106*, 65-77. https://doi.org/https://doi.org/10.1016/j.conbuildmat.2015.12.033

Nmai, C., Bury, M., & Daczko, J. (2018). Shrinkage of Concrete: Minimizing/Eliminating The Potential For Cracking. *Tilt-Up Concrete Association, January*, *27*, 2018.

Orangun, C. O., Jirsa, J. O., & Breen, J. E. (1977). A Reevaulation of Test Data on Development Length and Splices. *ACI Journal Proceedings*, *74*(3). https://doi.org/10.14359/10993

Paswan, R., Rahman, M. R., Singh, S. K., & Singh, B. (2020). Bond Behavior of Reinforcing Steel Bar and Geopolymer Concrete [Article]. *Journal of Materials in Civil Engineering*, *32*(7), Article 04020167. https://doi.org/10.1061/(ASCE)MT.1943-5533.0003237

Peng, K. D., Zeng, J. J., Huang, B. T., Huang, J. Q., Zhuge, Y., & Dai, J. G. (2022). Bond performance of FRP bars in plain and fiber-reinforced geopolymer under pull-out loading [Article]. *Journal of Building Engineering*, *57*, Article 104893. https://doi.org/10.1016/j.jobe.2022.104893

Pineda, J. E. P. (2022). *Structural performance of geopolymer concrete: shear and flexural capacity of a composite section prestressed bridge deck* TU Delft].

Ponomar, V., Luukkonen, T., & Yliniemi, J. (2023). Revisiting alkali-activated and sodium silicate-based materials in the early works of Glukhovsky. *Construction and Building Materials*, *398*, 132474. https://doi.org/https://doi.org/10.1016/j.conbuildmat.2023.132474

Prinsse, S., Hordijk, D. A., Ye, G., Lagendijk, P., & Luković, M. (2020). Time-dependent material properties and reinforced beams behavior of two alkali-activated types of concrete [Article]. *Structural Concrete*, *21*(2), 642-658. https://doi.org/10.1002/suco.201900235

Provis, J. L., & Van Deventer, J. S. (2013). *Alkali activated materials: state-of-the-art report, RILEM TC 224-AAM* (Vol. 13). Springer Science & Business Media.

Purdon, A. O. (1935). *Improvement in Processes of manufacturing Cement, Mortars and Concretes* (GB Patent No.

Rangan, B. V. (2009). 11 - Engineering properties of geopolymer concrete. In J. L. Provis & J. S. J. van Deventer (Eds.), *Geopolymers* (pp. 211-226). Woodhead Publishing. https://doi.org/https://doi.org/10.1533/9781845696382.2.211

Romanazzi, V., Leone, M., Aiello, M. A., & Pecce, M. R. (2022). Bond behavior of geopolymer concrete with steel and GFRP bars [Article]. *Composite Structures*, *300*, Article 116150. https://doi.org/10.1016/j.compstruct.2022.116150

Ryu, G. S., Lee, Y. B., Koh, K. T., & Chung, Y. S. (2013). The mechanical properties of fly ash-based geopolymer concrete with alkaline activators. *Construction and Building Materials*, *47*, 409-418. https://doi.org/https://doi.org/10.1016/j.conbuildmat.2013.05.069

S. Zhang, G. Y. (2021). *Testing Report on Phase I: Part 1: Development of self-compacting geopolymer*.

Sagoe-Crentsil, K., Brown, T., & Taylor, A. (2013). Drying shrinkage and creep performance of geopolymer concrete [Article]. *Journal of Sustainable Cement-Based Materials*, *2*(1), 35-42. https://doi.org/10.1080/21650373.2013.764963

Saranya, P., Nagarajan, P., & Shashikala, A. P. (2021). Experimental Investigation on Bond Strength Properties of Geopolymer Concrete. In (pp. 731-740). Springer Singapore. https://doi.org/10.1007/978-981-15-5644-9_57

Sarker, P. K. (2011). Bond strength of reinforcing steel embedded in fly ash-based geopolymer concrete [Article]. *Materials and Structures/Materiaux et Constructions*, *44*(5), 1021-1030. https://doi.org/10.1617/s11527-010-9683-8

Shah, A., & Shah, C. (2017). Comparison of load-displacement relationship and crac k development mechanism in reinforced geopolymer concrete beams with that o f regular reinforced concrete beams. International Conference on Advances i n Construction Materials and Systems, Chennai,

Shi, C., Jiménez, A. F., & Palomo, A. (2011). New cements for the 21st century: The pursuit of an alternative to Portland cement. *Cement and Concrete Research*, *41*(7), 750-763. https://doi.org/https://doi.org/10.1016/j.cemconres.2011.03.016

Sofi, M., Van Deventer, J. S. J., Mendis, P. A., & Lukey, G. C. (2007). Bond performance of reinforcing bars in inorganic polymer concrete (IPC) [Article]. *Journal of Materials Science*, *42*(9), 3107-3116. https://doi.org/10.1007/s10853-006-0534-5

Subramanian, N., & Solaiyan, E. (2021). Study on bond strength of geopolymer and control concrete between fiber-reinforced polymer and steel bars [Article]. *Structural Concrete*, *22*(1), 146-153. https://doi.org/10.1002/suco.201900506

Sulaiman, M. F., Ma, C.-K., Apandi, N. M., Chin, S., Awang, A. Z., Mansur, S. A., & Omar, W. (2017). A Review on Bond and Anchorage of Confined High-strength Concrete. *Structures*, *11*, 97-109. https://doi.org/https://doi.org/10.1016/j.istruc.2017.04.004

Superfine Technisch datasheet - CO2-arme, hoogwaardige GGBS voor veeleisende betontoepassingen.
Tepfers, R. (1973). A theory of bond applied to overlapped tensile reinforcement splices for deformed bars. *Division of concrete structures*.
Tepfers, R. (1979). Cracking of concrete cover along anchored deformed reinforcing bars. *Magazine of Concrete Research*, *31*(106), 3-12. https://doi.org/10.1680/macr.1979.31.106.3
Topark-Ngarm, P., Chindaprasirt, P., & Sata, V. (2015). Setting time, strength, and bond of high-calcium fly ash geopolymer concrete [Article]. *Journal of Materials in Civil Engineering*, *27*(7), Article 04014198. https://doi.org/10.1061/(ASCE)MT.1943-5533.0001157
Tran, T. T., Pham, T. M., & Hao, H. (2019). Experimental and analytical investigation on flexural behaviour of ambient cured geopolymer concrete beams reinforced with steel fibers. *Engineering Structures*, *200*, 109707. https://doi.org/https://doi.org/10.1016/j.engstruct.2019.109707
Un, C. H., Sanjayan, J. G., San Nicolas, R., & Van Deventer, J. S. J. (2015). Predictions of long-term deflection of geopolymer concrete beams [Article]. *Construction and Building Materials*, *94*, 10-19. https://doi.org/10.1016/j.conbuildmat.2015.06.030
Vandewalle, L. (1992). Theoretical prediction of the ultimate bond strength between a reinforcement bar and concrete. *Bond in Concrete: from Research to Practice, Riga*.
Villalba, S., & Casas, J. R. (2013). Application of optical fiber distributed sensing to health monitoring of concrete structures. *Mechanical Systems and Signal Processing*, *39*(1), 441-451. https://doi.org/https://doi.org/10.1016/j.ymssp.2012.01.027
Wang, S.-D., Scrivener, K. L., & Pratt, P. (1994). Factors affecting the strength of alkali-activated slag. *Cement and Concrete Research*, *24*(6), 1033-1043.
Wardhono, A., & et al. (2017). Comparison of long term performance between alkali activated slag and fly ash geopolymer concretes. *Construction and Building Materials*, *143*, 272.
Whiting, J. (1895). *Manufacture of Cement* (US Patent No. 544706).
Xin, L., Jin-yu, X., Weimin, L., & Erlei, B. (2014). Effect of alkali-activator types on the dynamic compressive deformation behavior of geopolymer concrete. *Materials Letters*, *124*, 310-312. https://doi.org/https://doi.org/10.1016/j.matlet.2014.03.102
Ye, H., & Radlińska, A. (2016). Shrinkage mechanisms of alkali-activated slag. *Cement and Concrete Research*, *88*, 126-135. https://doi.org/https://doi.org/10.1016/j.cemconres.2016.07.001
Yip, C. K., Lukey, G. C., & van Deventer, J. S. J. (2005). The coexistence of geopolymeric gel and calcium silicate hydrate at the early stage of alkaline activation. *Cement and Concrete Research*, *35*(9), 1688-1697. https://doi.org/https://doi.org/10.1016/j.cemconres.2004.10.042
Yost, J. R., Radlińska, A., Ernst, S., Salera, M., & Martignetti, N. J. (2013). Structural behavior of alkali activated fly ash concrete. Part 2: structural testing and experimental findings. *Materials and Structures*, *46*(3), 449-462. https://doi.org/10.1617/s11527-012-9985-0
Zhang, H. Y., Kodur, V., Wu, B., Yan, J., & Yuan, Z. S. (2018). Effect of temperature on bond characteristics of geopolymer concrete. *Construction and Building Materials*, *163*, 277-285. https://doi.org/https://doi.org/10.1016/j.conbuildmat.2017.12.043
Zhang, S., Ye, G., Lukovic, M., Hendrik, H., & Scharringa, A. (2022). Geopolymeerbeton voor infrastructurele toepassingen (1): Ontwikkeling van zelfverdichtende mengsels. *Cement: vakblad voor de betonwereld*, *2022*(7), 42-50.